Investigating the variability of O_2 dayglow and temperatures in the mesosphere and lower thermosphere using satellite data

Zur Erlangung des akademischen Grades eines

DOKTORS DER NATURWISSENSCHAFTEN

von der Fakultät für Physik des
Karlsruher Instituts für Technologie

genehmigte

DISSERTATION

von

Amirmahdi Zarboo
aus Yazd, Islamische Republik Iran

Referent: Prof. Dr. Johannes Orphal

Korreferent: Dr. Michael Höpfner
Betreuer der Doktorarbeit: Dr. Miriam Sinnhuber

Tag der mündlichen Prüfung: 10.05.2019

Abstract

Understanding the current climate change, and predicting its future development, is of great concern. At the same time, large uncertainties in climate models persist due to our incomplete understanding of natural processes in the Earth's atmosphere. The mesosphere (50 to 100 km) belongs to the less well studied regions of the atmosphere. However, state-of-the art chemistry-climate models used, e.g., for coordinated modelling studies for the next IPCC report, have their upper boundary in the region of the mesopause (80–95 km). Many processes therein were discovered only recently and are still not well understood neither reproduced in chemistry-climate models. Recently, a true inter-hemisphere coupling has been found which connects the winter stratosphere at around 20 km altitude in one hemisphere to the summer mesopause around 80 km in the other hemisphere. Wind, temperature, and waves drive this interaction. Other recent results suggest that disturbances can propagate from the mesosphere down to the troposphere where they influence surface pressure and temperature, i.e., the weather patterns. Various processes contribute to the mesosphere dynamics and its energy budget. Studying them in more detail is essential to better understand the middle atmosphere dynamics and to better represent the dynamical coupling from the mesosphere to the surface in chemistry-climate models.

In this work, I developed retrieval algorithms for two mesospheric components important for the energy budget of the MLT region, the O_2 dayglow and temperatures, using data from SCIAMACHY on-board the Envisat satellite. The method includes development of the retrieval algorithm for deriving O_2 emission intensities, and O_2 volume emission rates. Temperature was then derived from the emission intensities of $O_2(^1\Sigma)$. The error analysis and validation of the retrievals against other data products from other satellite instruments were also carried out, and show data of good quality in 80 to 120 km for $O_2(^1\Sigma)$, in 60 to 100 km for $O_2(^1\Delta)$, and 90 to 120 km for temperature. The whole data-set of SCIAMACHY observations in the MLT region from mid-2008 to March 2012 was analyzed, and time-series as well as climatologies were produced and investigated for all properties. Solar radiation and dynamical forcing are the most important drivers which provide and control the O_2 dayglow in the MLT region. The temperature variations in the mesosphere-lower thermosphere are mostly driven by the dynamics in the upper mesosphere, and by the solar forcing in the lower thermosphere.

Contents

Acknowledgements

1 Introduction

Focus of this thesis is the investigation the O_2 dayglow and temperatures in the region of the mesosphere and lower thermosphere region (50–150 km). The MLT is a transition region between space and the atmosphere. It is reached, on the one hand, by the upper branch of the meridional overturning circulation connecting the stratosphere and mesosphere, on the other hand affected by "space weather". Space weather impacts are transferred from the thermosphere to the atmosphere below through the MLT region, and waves from the surface to the thermosphere and ionosphere. In this Chapter, an overview over some fundamental concepts important for the topic of the thesis is given. In Section 1.1, an overview of vertical structure of the atmosphere is given; in Section 1.2 a brief of the circulation of the middle atmosphere is presented. In Section 1.3 a short review of the key features of the oxygen chemistry in the MLT region is presented. In Section 1.4 an introductory explanation of the responses of the middle atmosphere to the global climate change is stated. Finally in Section 1.5, the airglow from which the data are extracted and analyzed, and the processes driving it in the middle atmosphere, is briefly discussed.

1.1 The Earth's atmosphere

In this section, a short introduction on the vertical structure of the Earth's atmosphere is given. My focus is on the mesosphere and lower thermosphere region (MLT, ∼50–∼150 km), which is a transition region, between space and the atmosphere. It is reached, on the one hand, by the upper branch of the meridional overturning circulation connecting the stratosphere and mesosphere, on the other hand affected by "space weather". Space weather impacts are transferred from the thermosphere to the atmosphere below through the MLT region, and waves from the surface.

Figure 1.1 shows the typical behavior of the temperature throughout the atmosphere. The Earth's atmosphere is divided into several layers on the basis of temperature variability. In the lowermost layer which is called Troposphere containing more than 75% of the atmospheric mass and almost all of its humidity, temperature decreases with increasing altitude. The temperature's behavior changes its sign in a narrow region which separates the Troposphere from its higher layer and is called Tropopause. Above the tropopause, in the layer called Stratosphere temperature increases with increasing altitude due to the

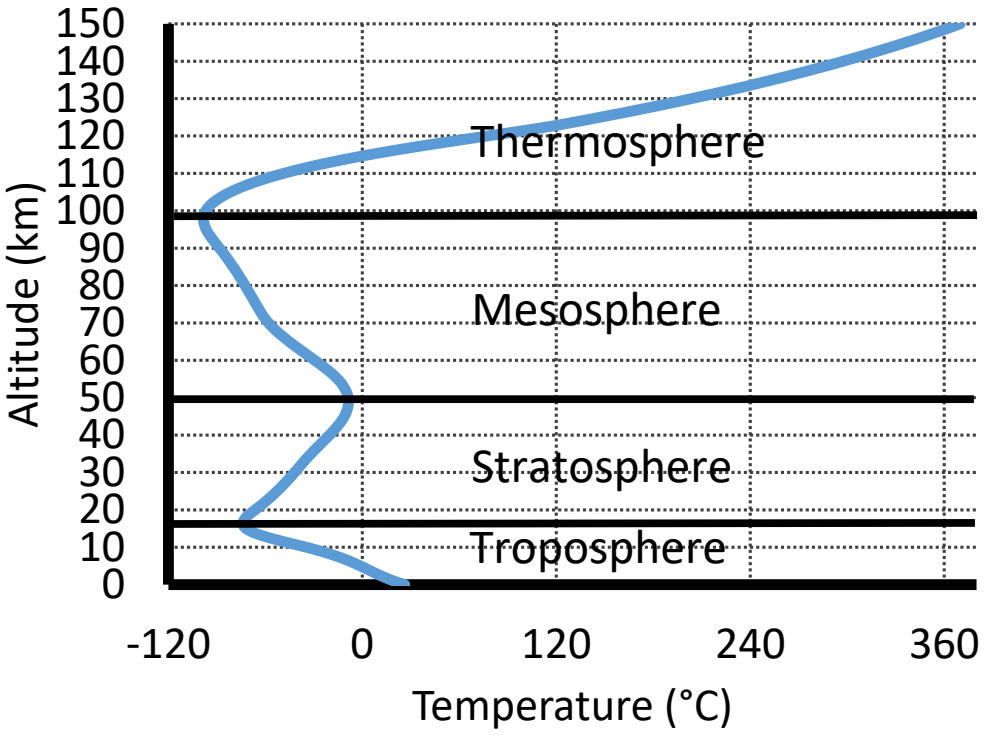

Figure 1.1: Typical temperature changes throughout the atmospheric layers from surface to thermosphere (∼150 km) (based on nrlmsise-00 data, on 03/07/2011, 11 am, zonally averaged, Picone et al. (2002)).

absorption of shortwave solar radiation by ozone. The behavior of temperature changes in the narrow layer above the stratosphere which is called stratopause and is located around about 50 km altitude on average. The mesosphere is a layer above the Stratopause in which temperature decreases with altitude as a result of the smaller solar heating by ozone at higher altitudes (Holton and Hakim, 2012). The thermosphere is the only layer above the mesosphere that extends out to heights of ∼500–1000 km which comprises a tiny fraction of the atmosphere's mass.

1.1.1 The Troposphere

The lowest layer of the atmosphere is known as troposphere (literally the "changing atmosphere"). The troposphere contains more than 75% of the atmospheric mass, 99% of the total mass of water vapor, aerosols, most clouds and all precipitation.

In the troposphere the average temperature decreases with height at a rate of near 6.5 $\mathrm{K\,km^{-1}}$, because of the effect of decreasing longwave radiative forcing with increasing altitude from the Earth's surface, and the effect of convection. The temperature of the atmosphere stops decreasing at the tropopause due to absorption of the Sun's ultraviolet (UV) radiation. This absorption, as suggested by Gold (1909), is by the increasing concentrations of ozone (O_3) above the troposphere. Strong vertical motions near the equator raise the base of the ozone layer, forcing ozone to spread horizontally to higher altitudes. Near the poles, downward motions push the ozone to lower heights, giving the variation in tropopause height between the equator and poles. The height of the tropopause varies between 9 and 16 km, being higher over the equator.

1.1.2 The Stratosphere

The stratosphere (literally the "Stratified Sphere") is a region of the atmosphere which is resistant to vertical motions because it has high static stability. Therefore there is little dynamic exchange of air between the stratosphere and the troposphere below. This stability is because of its negative lapse rate (i.e., temperature increases with height). This temperature increase with increasing height in the stratosphere is due to the strong absorption of solar radiation. Figure 1.2 shows the most important contributions to the radiative heating and cooling of the atmosphere. The stratosphere is nearly in radiative equilibrium, with radiative heating by ozone and balanced by radiative cooling by CO_2, ozone and H_2O, as it is clearly seen in the figure.
The dynamical behavior of the stratosphere is dominated by strong large scale flow system like Brewer-Dobson circulation (BDC), tropical and polar-night jet streams, and the quasi-biennial oscillation (QBO). The BDC is the global mass circulation of stratospheric air initiated by tropospheric air entering the stratosphere in the tropical tropopause (Butchart, 2014) which is described in Section 1.2. The QBO is an oscillation in the zonal winds above the equator, which change direction on average every 13 months, corresponding to a period of approximately 26 months, alternating between westward and eastward winds. Jet streams are cores of strong winds at ∼8–11 km from the Earth's surface, blowing from west to east. They develop on the border between cold and warm air masses, over the middle latitudes as "polar front jetstream" and over the subtropics as "subtropical jet". Since there is no surface friction at high altitude, extraordinarily high altitude winds occur with speeds of 200 to 500 km/hr. A dramatic phenomenon of the polar stratosphere is the *Stratospheric Sudden Warming* (Pedatella et al., 2018), which is a rapid increase in polar stratospheric temperatures accompanied by a weakening or even reversal of the stratospheric zonal mean winds. This warming occurs because warm air from mid-latitudes is brought to higher latitudes during a distortion or break up of the polar vortex from strong planetary wave activity. Major stratospheric warmings usually appear only in the northern hemisphere,

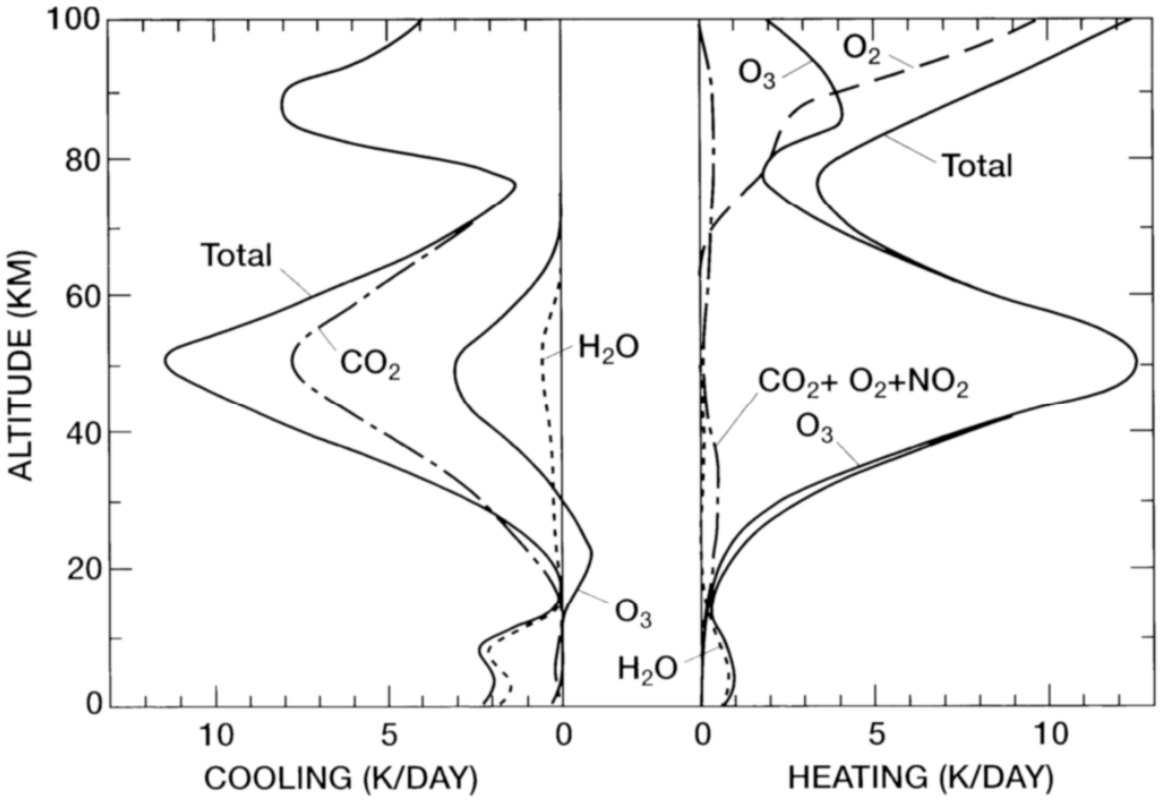

Figure 1.2: The dominant heating and cooling rates of different chemical species found in the atmosphere at various heights, measured in $\mathrm{K\,day^{-1}}$ (After Brasseur and Solomon (2006))

although one was observed in the southern hemisphere in 2002 (Smith-Johnsen et al., 2018).
The top of the stratosphere is called the *stratopause*, at heights near 55 km where a temperature maximum occurs. This is due to the peak in radiative heating clearly seen in Figure 1.2.

1.1.3 The Mesosphere

The *mesosphere* (literally "middle sphere") lies above the stratosphere and is a layer where the temperature decreases with increasing height. As can be seen from Figure 1.2 the amount of radiative heating decreases to a minimum in the Mesosphere. This is because of the depleting concentrations (measured as a fraction of the atmosphere) of atmospheric ozone in this region. Other chemical species in the mesosphere are not abundant enough to sustain the level of heating. There is also a reduction in radiative cooling of carbon dioxide (CO_2). This is not however, enough to keep the same level of heating as in the stratosphere and mesospheric temperatures are allowed to decrease.
The mesosphere is arguably the least explored part of the atmosphere. This is because it is too high to reach with aircraft or balloons for *in situ* measurements. Similarly, it is too dense for satellite orbits, so *in situ* measurements from space are also difficult to carry out. It is possible to make some *in situ* measurements with sounding rockets, and falling spheres; but these only give a snapshot through the atmosphere and can not be used from many locations. Because of these limitations, most studies of the mesosphere use either ground-based or space-based remote sensing. There are a number of different remote-sensing techniques which are now in use to measure the mesosphere. These include satellite instruments, lidar, meteor-wind radar, medium frequency radar, incoherent-scatter radar, mesosphere-stratosphere-troposphere radar, airglow cameras and spectrometers. All of these techniques have their individual strengths and limitations.
Temperature decreases with height throughout the mesosphere. The coldest temperatures in Earth's atmosphere, about -90°C, are found near the top of this layer, such that the summer mesopause at high latitudes is the coldest point in the atmosphere. The reason for this very cold temperatures is that breaking gravity waves imply an upward/equatorwards drag. The ensuing upward motion leads to adiabatic expansion, which cools the atmosphere. At the winter stratopause, the reverse happens. Downward motion leads to adiabatic compression and (dynamical) warming. In fact, the mesosphere is not in radiative equilibrium, as large scale dynamical heating and cooling contributes.
The mesosphere hosts some strange and beautiful phenomena. These include *noctilucent* clouds, the giant lightening discharges known as *sprites*, *meteors* and *airglow*. Noctilucent clouds, called like this because they are visible from ground only during night-time, are the highest clouds found in the Earth's atmosphere, which are restricted to the very cold

temperatures at the summer mesopause at high latitudes. The height of these clouds means that they are illuminated by direct sunlight when the Sun for the observer has passed below the horizon i.e., they are brightly lit during twilight. Sprites are giant upward lightning discharges. They are launched into the mesosphere from the top of thunderstorms. The top of the mesosphere is the *mesopause* at a height of about 80–100 km. Figure 1.3 shows the mesopause altitude as observed during the cruise of the ship MS Polarstern, in 1996 (Von Zahn et al., 1996). It exhibits a high mesopause height (near 100 km) over the whole winter hemisphere and equatorial region. However, at 24°N the mesopause abruptly drops down towards a summer height of about 85 km. The mesopause is the region in which extra-terrestrial material is brought into the Earth's atmosphere by ablating meteoroids which give off the bright flashes of light sometimes visible as meteors. The ablation of meteors leaves behind layers of metallic chemical species. One of these chemicals, sodium (Na), creates a layer in the atmosphere from which there is a very weak emission of light. This is known as an airglow layer, see also Section1.5.

1.1.4 The Thermosphere

The Thermosphere (literally the "hot sphere") is the layer above the mesosphere that extends out to heights of ∼500–1000 km. The thermosphere comprises only a tiny fraction of the atmosphere's mass, less than 0.01% of the total. Below the thermosphere, gases made of different types of atoms and molecules are thoroughly mixed together by turbulence in the atmosphere. In the thermosphere and above, gas particles collide so infrequently that the gases become separated based on the types of chemical elements they contain. Additionally, the far-UV and EUV radiation in the thermosphere make the trace gases which are stable in the middle atmosphere, like O_2, N_2, CO_2, dissociated or ionized. As a result, its chemical composition changes significantly with height, as can be seen in Figure 1.4. Above about 100 km molecular diffusion influences the atmospheric chemical species, separating them according to mass (i.e., in the lower thermosphere, molecular Nitrogen dominates, whereas higher up, atomic oxygen becomes the dominant constituent, and even further up, atomic hydrogen is dominant).

There are strong diurnal changes in the temperature of the thermosphere and the temperature also varies strongly with changing solar activity. In the thermosphere, it can reach more than 1000°C. These high temperatures result from the absorption of short-wavelength solar radiation in the ultraviolet and extreme ultraviolet wavelength range (from 121.6 nm to 170 nm) by molecular and atomic oxygen as well as nitrogen. This short-wave radiation also ionizes the atmosphere and leads to the formation of the *ionosphere*. The *ionosphere* is embedded within the neutral gas of the thermosphere.

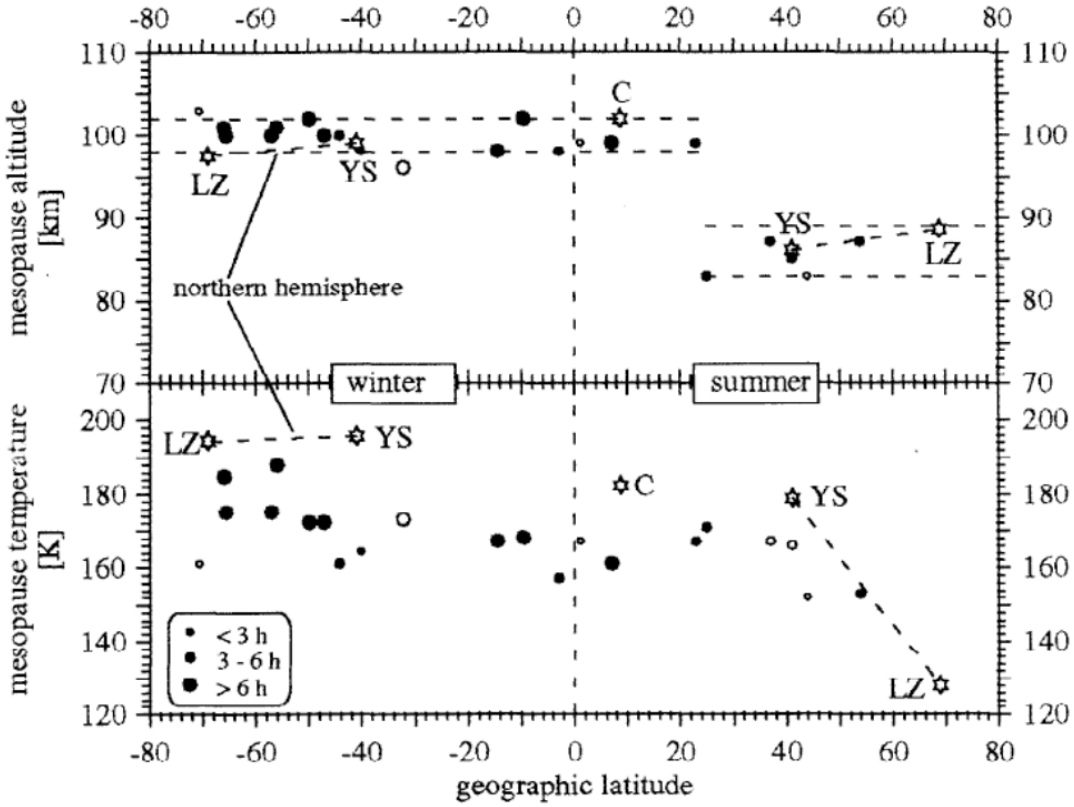

Figure 1.3: Lidar observations of mesopause heights from May and June 1996 operated on board the research vessel MS PolarStern providing temperature profiles from both hemispheres (Taken from Von Zahn et al. (1996))

1.1.5 The Exosphere

The *exosphere* (literally the "outer sphere") is the outer-most layer of the atmosphere. This region is the transition between atmosphere and space. Its lower boundary is the *thermopause / exobase* at an altitude that ranges from ∼500 km to ∼1000 km (depending on solar activity) and it extends out to about 10,000 km (Dzubenko et al., 2003). This is the only layer from which atmospheric gases, atoms and molecules can escape the Earth's atmosphere.

1.1.6 Other classifications of the atmospheric structure

Other classifications of the vertical layers of the atmosphere exist based on other physical parameters besides temperature.

Another classification of layers is one that divides the atmosphere into lower, middle and upper regions. These divisions are based on the different physical processes which dominate the behavior in each region. The *Lower Atmosphere* is the troposphere and is dominated by meteorological phenomena i.e., it is the region in which weather systems occur. The *middle*

atmosphere refers to the atmosphere extending from the tropopause up to about 110 km. It includes the stratosphere, mesosphere, and lower thermosphere. In this region the gases are overwhelmingly neutral, so it is largely free from the influence of magnetic and electric fields. The dominant physical processes of the middle atmosphere are therefore those of fluid dynamics, including vertically propagating atmospheric waves of large amplitude. Above the middle atmosphere is the *upper atmosphere* (above about 110 km). Here the air becomes significantly ionized and begins to be strongly influenced by the Earth's magnetic and electric fields.

The atmosphere can alternatively be divided into two regions, the *homosphere* and the *heterosphere*. The homosphere (literally the "same sphere") extends from the Earth's surface up to a height of about 105 km. The homosphere is a region where turbulent mixing yields a near-homogeneous composition of about 78.01% molecular nitrogen (N_2); 20.9% molecular oxygen (O_2); 0.9% argon (Ar); 0.4% carbon dioxide (CO_2) and other trace constituents. This can be seen in Figure 1.4, below about 105 km, where the number density of molecular oxygen and nitrogen decreases at the same rate as the global mean pressure decreases. The *turbopause* marks the ceiling of the homosphere and is also the height below which turbulent mixing dominates. Above the turbopause the mean free path becomes larger than the turbulent displacement of air (i.e., turbulent mixing is strongly damped). The heterosphere (literally "different sphere") is the Eearth's atmosphere above a height of about 105 km. Within this region due to the dominance of molecular diffusion, the molecules and atoms of the atmospheric gases each have individual scale heights.

1.2 Mean meridional circulation of the middle atmosphere

In the troposphere Hadley, Ferrel, and Polar cells are responsible for transporting heat and momentum in the north-south direction (Holton and Hakim, 2012). In the middle atmosphere, the mean meridional circulation is driven by gravity and planetary wave breaking. Waves drive the global scale meridional-vertical circulation pattern connecting the stratosphere and mesosphere. Dissipating planetary waves drive a poleward and downward movement in the lower stratosphere which is called the Brewer-Dobson Circulation (BDC). Above the stratosphere, the mesospheric circulation moves air from the summer to the winter pole. It is driven by dissipating gravity waves, which imply a drag, the so-called gravity wave drag. This moves air upward and equatorwards in the summer hemisphere, downward and polewards in the winter hemisphere. Air in the descending branch of the BDC exits the stratosphere at the extratropical tropopause and affects tropospheric composition. Figure 1.5 shows a schematic of the middle atmosphere circulation.

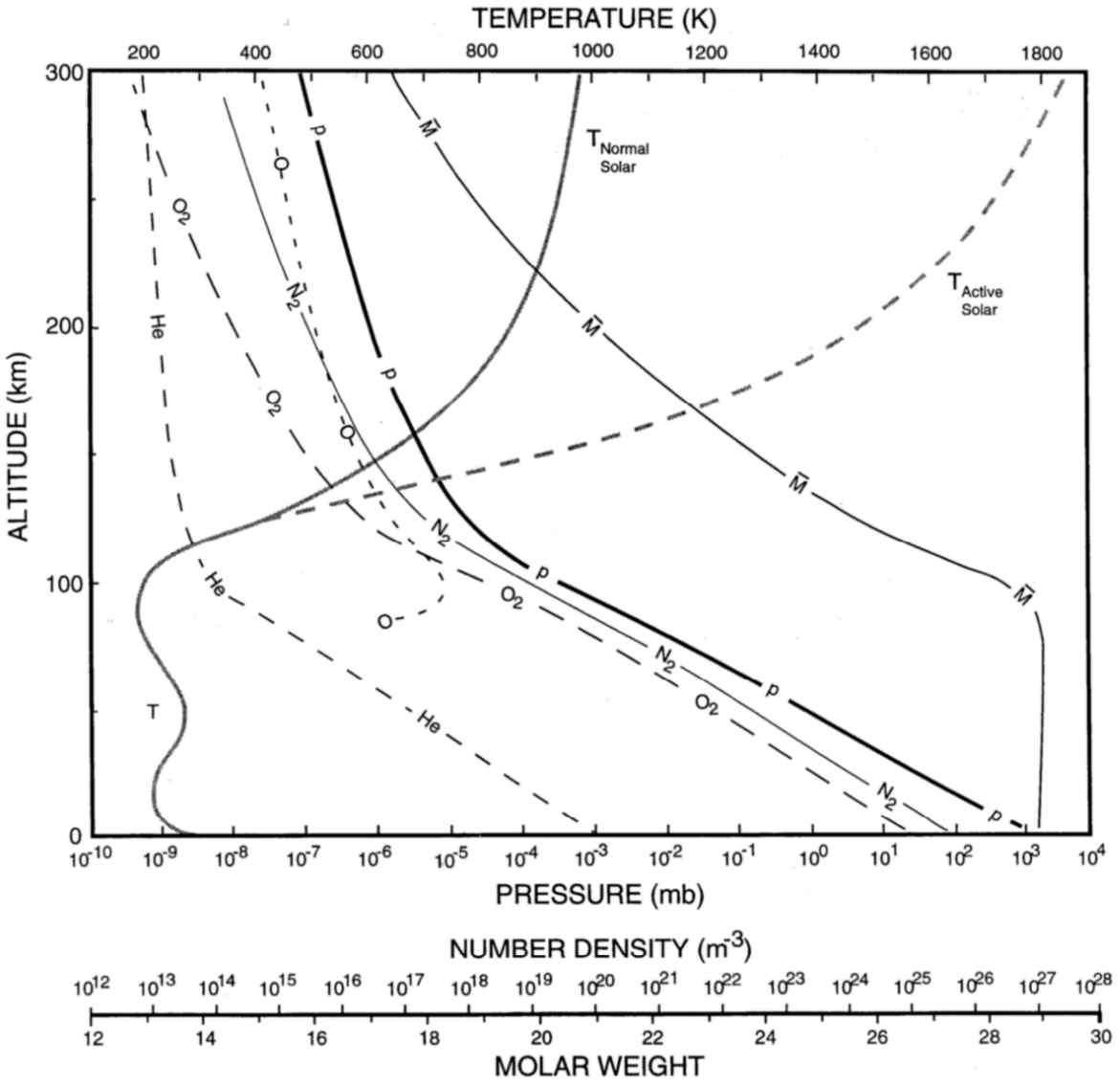

Figure 1.4: Number density of atmospheric constituents (Helium (He), Atomic oxygen (O), Molecular oxygen (O_2) and Molecular Nitrogen (N_2)), mean molar weight ($\bar{M}$), temperature (T) and Global-mean pressure (p) of the atmosphere with height (After Salby (1996), from the U.S. Standard Atmosphere).

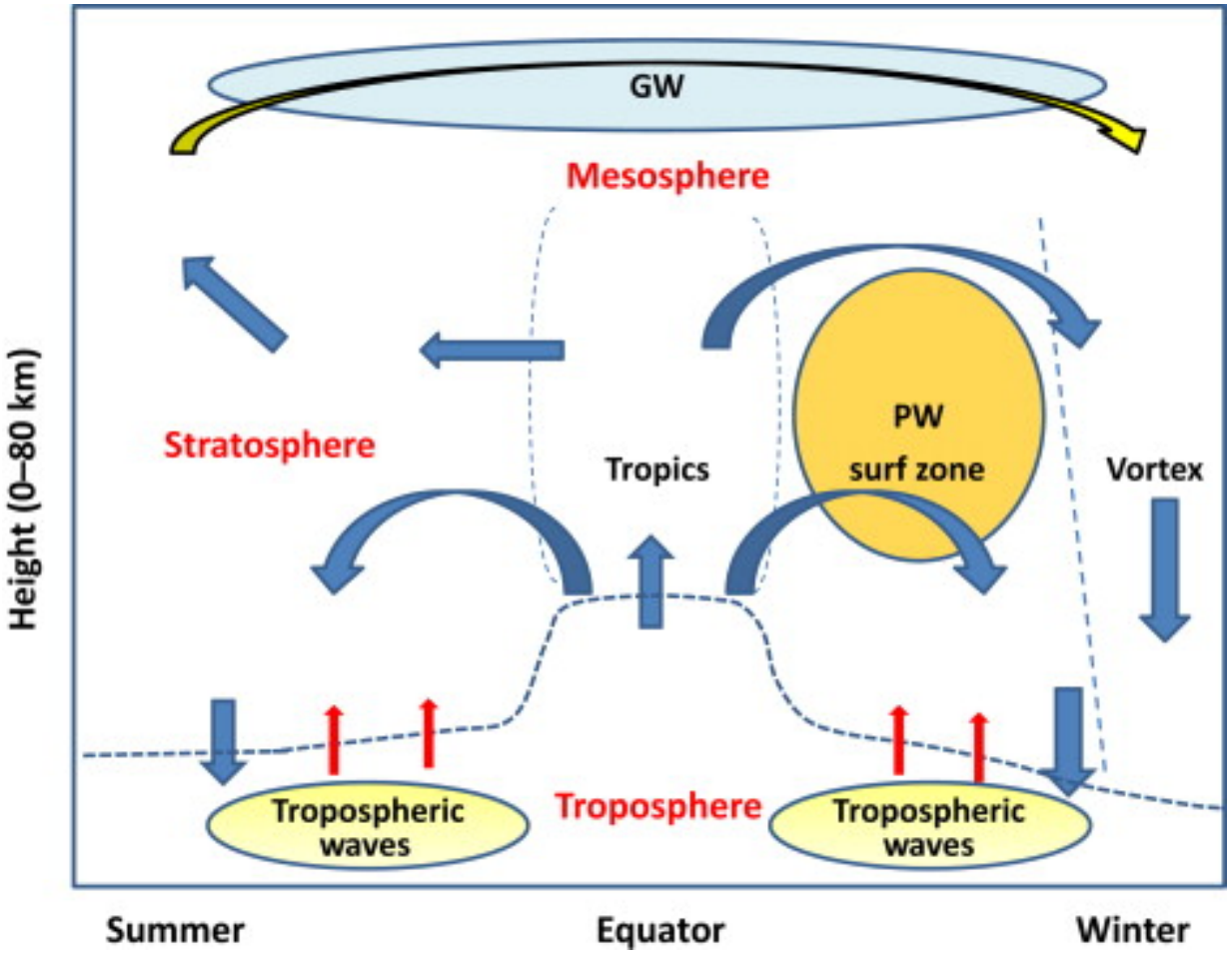

Figure 1.5: Schematic of the transport circulation in the middle atmosphere. Adapted from Strahan (2015).

1.3 Oxygen chemistry in the MLT region

All of the solar energy in the UV region in the wavelength interval 150–300 nm is deposited in the middle atmosphere Council (1994). This energy has an essential role in chemistry, radiation, and dynamics of this region. Inversion of the atmospheric temperature profile at about 15 km, which defines the tropopause, is the direct effect of heating from solar UV radiation absorbed by ozone in the middle atmosphere. Only solar radiation with shorter wavelengths which reaches the middle atmosphere, has very little contribution and sporadic X-ray and Lyman α radiations at 121.6 nm. The ozone layer is produced by the interaction between the solar UV radiation with the middle atmospheric molecular and atomic oxygen. Photodissociation of the molecular oxygen by solar UV radiations at 170–242 nm (Schumann-Runge bands, and Herzberg continuum) is the most important source of atomic oxygen and therefore for ozone production in the middle atmosphere. Produced by a combination of atomic and molecular oxygen, ozone itself is photodissociated by solar UV radiation in the 240–300 nm range (in the Hartley band and continuum).
The main production and loss of ozone in the MLT can be summarized as follows:

$$O_2 + h\nu \rightarrow O + O \tag{1.1}$$

$$O_3 + h\nu \rightarrow O(^1D) + O_2 \tag{1.2}$$

$$O + O_3 \rightarrow 2O_2 \tag{1.3}$$

$$O(^1D) + O_2 \rightarrow O + O_2(^1\Sigma) \tag{1.4}$$

$$O + O_2 + M \rightarrow O_3 + M \tag{1.5}$$

At the top of the MLT, photolysis of ozone by extreme UV or UV radiation (e.g. Reaction 1.12) is prevalent which results in the production of atomic and molecular oxygen.
Figure 1.6 shows the zonal mean climatology of oxygen species in different months averaged over 2003–2011 from SABER data[1], see also Section 2.2.3. It is apparent that ozone dominates around and just above the stratopause (40–50 km). In the lower mesosphere around 50 to 60 km, ozone and atomic oxygen have similar mixing ratios. In the upper mesosphere and lower thermosphere, atomic oxygen is much more abundant than ozone. Around 85–95 km, a secondary maximum in the ozone concentration is observed. This behavior is governed by the relative reaction speeds of the ozone formation reaction ($O + O_2$) and the O_2 photolysis rate. In the upper mesosphere and lower thermosphere, the O_2 photolysis is much faster than the $O + O_2$ reaction which is pressure dependent (see reaction 1.5); in the lowermost mesosphere, the ozone formation reaction is comparable or faster.

[1] http://saber.gats-inc.com/browse_data.php

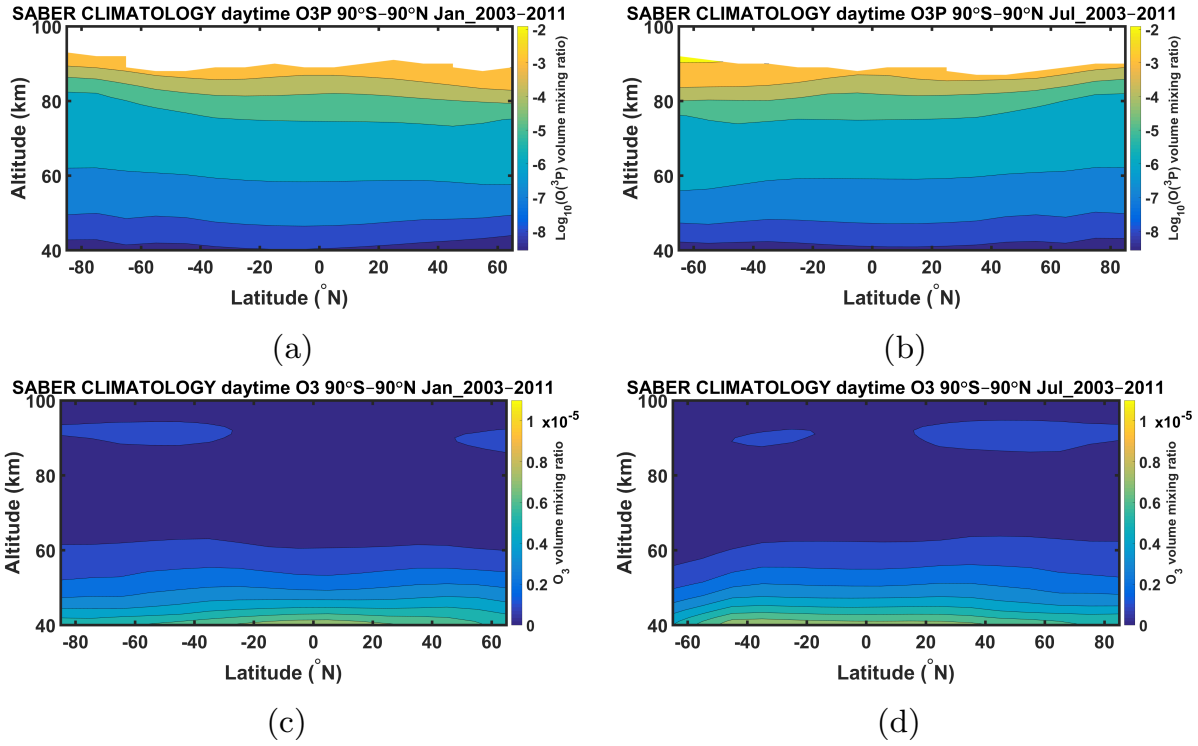

Figure 1.6: SABER climatologies of oxygen species in the MLT region, averaged over years 2003-2011. (a) Atomic oxygen volume mixing ratio for January (b) same as (a) for July. (c) Ozone volume mixing ratio for January (d) same as (c) for July (http://saber.gats-inc.com/browse_data.php contains SABER data, see, e.g., Subsection 2.2.3.

1.4 Greenhouse Effect and Middle Atmosphere Cooling

For a long while now, evidence has shown that increases in manmade greenhouse gases raise temperatures of the lower atmosphere. Greenhouse gases, such as carbon dioxide (CO_2), trap the Sun's energy, which has been absorbed by the Earth and re-emitted, which would otherwise be allowed to escape. This effectively warms the lower atmosphere and surface temperatures (Pachauri et al., 2014).

It is clear that human activity affects the Earth's atmosphere. The release of chlorofluorocarbons (CFCs) has significantly increased the rate of destruction of the protective ozone layer by influencing chemical reactions in the polar stratosphere (e.g. the Antarctic ozone hole (WMO, 2018)[2]). CFC concentrations in the stratosphere have been relatively stable in recent years, and are now showing signs of decline due to the action of the Montreal Protocol (WMO, 2018). Although Dameris et al. (2014) stated that a noticeable decrease in the size of the ozone hole is not expected until at least ∼2018, WMO (2018) indicated that there are emerging indications that the Antarctic ozone hole has diminished in size and depth since the year 2000, for the first time.

The state of the knowledge about climate change is summarized, e.g., in the report of the Intergovernmental Panel on Climate Change IPCC (2013). Atmospheric concentrations of carbon dioxide, methane, and nitrous oxides have increased to a level which is unprecedented at least during the last 800,000 years. The carbon dioxide concentrations have increased compared to the pre-industrial era by as much as 40%, mainly due to the anthropogenic emissions from fossil fuels and secondarily because of the emissions resulted from land-use changes. The oceans have absorbed about 30% of the anthropogenic emitted carbon dioxide which resulted in the acidification of the oceans. The net radiative forcing is positive, and yields the net uptake of energy by the climate system. The greatest contribution in the total radiative forcing is due to increase of atmospheric concentrations of CO_2 since 1970s. Each of the last three decades is considered as the warmest period compared to the previous time spans since 1850s.

Most of the climate change aspects will remain unchanged for several centuries even if the CO_2 emissions stop. This represents the significant multicentury formed climate change which is caused by the past, current, and future emissions of CO_2 (IPCC, 2013).

This is due to the lower number of collisions between molecules at these heights due to the low density. Since the late 1970's, a general cooling trend of approximately 1°C per decade has been clearly identified in the stratosphere Randel et al. (2009). Several modeling studies have investigated scenarios of greenhouse cooling in the stratosphere and mesosphere (Akmaev and Fomichev, 2000; Bremer and Berger, 2002; Akmaev, 2002, 2003). Akmaev and Fomichev (2000) suggested that the stratospheric ozone depletion may contribute to

[2]Link to the report: https://www.esrl.noaa.gov/csd/assessments/ozone/

the cooling in the mesosphere and thermosphere. Bremer and Berger (2002) examined the effect of the stratospheric ozone changes on mesospheric temperatures. They found that although confined to the stratosphere, ozone depletion has a profound cooling effect on mesospheric temperatures, which is comparable to or exceeding that of the CO_2 forcing (Bremer and Berger, 2002). For example, a study of Thomas (1996b) shows that under a doubled carbon dioxide-methane climate, it is possible that the mesopause will be cooled globally by 5–10 K and its water content enhanced by 50–100%. This in turn can extend the area covered by mesospheric clouds equatorward over major population areas. The occurrence of Noctilucent clouds is also thought to be increasing and they are being seen at lower latitudes than previously recorded (Cumberland, 2012). Although the middle atmosphere has been dubbed a "Miner's Canary" (Thomas, 1996a) for global change (Beig et al. (2003); Von Zahn (2003); Akmaev et al. (2006)), but it is still unclear how these changes affect the dynamics and chemistry which determine the state of the atmosphere.

1.5 Airglow

Airglow is an optical phenomenon of the high atmosphere in the 60–100 km altitude range, which occurs both during the day and the night. These emissions of this tenuous light in the atmosphere originate directly or indirectly from solar radiation. The solar radiation leads atoms and molecules to excited states that when decay to their fundamental states of energy, they release the excess energy in the form of electromagnetic radiation. The emissions of airglow have been used to monitor the atmosphere remotely. The main applications are related to the mesospheric temperature, wind and the dynamics of the mesosphere/thermosphere (Bageston et al., 2012).

1.5.1 Introduction

Atmospheric airglow in the mesosphere and thermosphere above approximately 60 km is formed by the fluorescence emission from the excited states of the atoms and molecules. Atoms and molecules in the mesosphere and lower thermosphere can be excited by means of absorption of solar radiation (photoluminescence) or by exothermic chemical reactions (chemiluminescence). Atomic and molecular excited states of oxygen produce an important contributing series in the terrestrial airglow. This contribution will be discussed in more detail in Subsection 1.5.2.
Among other contributions to the airglow are atomic sodium and hydroxyl radicals.
There is a metal layer of sodium atoms mainly due to the ablation of the meteors entering this region in the ∼82–105 km altitude range at which the maximum concentration is found at about 91 km altitude (Wayne, 1991). In the daytime, sodium atoms are excited directly

by solar radiation at 589.0 nm and 589.6 nm in the yellow region of the visible spectrum. At night, oxidation and reduction reactions constitute a cycle chain which excites Na(^{2}P) by oxidation of O_3.

$$Na + O_3 \rightarrow NaO + O_2 \tag{1.6}$$

followed by the reduction of NaO to yield excited ^{2}P or ground state ^{2}S sodium atoms.

$$NaO + O \rightarrow Na(^2P) + O_2 \tag{1.7}$$

$$NaO + O \rightarrow Na(^2S) + O_2 \tag{1.8}$$

In a layer at ∼87 km with ∼8 km thickness (Grygalashvyly et al., 2014) vibrational–rotational transitions between the lowest nine levels of ν'' in the electronic ground state of the OH results in an observed emission system called "OH Meinel bands". The observed transitions are not only limited to the "allowed" $\Delta\nu''$ =1, but also include "forbidden" $\Delta\nu'' > 1$ transitions. The allowed transitions, known as "fundamentals" lies between 4500 nm (ν'' = 9 → 8) and 2800 nm (ν'' = 1 → 0) and are intrinsically the strongest feature of the night-glow. The forbidden transitions known as "minors' with $\Delta\nu''$ = 4, 5, ... lie in the < 1000 nm wavelength range, and although much weaker than the fundamentals, they are more readily detected without interference with the thermal background of the atmosphere or detectors. There is a distinct cut-off at ν'' = 9 without any observed excitation in the ν'' = 10 (corresponding to 337 $KJ.mol^{-1}$). Atomic hydrogen reacts with ozone to form OH in the following excitation mechanism:

$$H + O_3 \rightarrow OH + O_2 + \ 332\ kJ\ mol^{-1} \tag{1.9}$$

which is exothermic in the range 312 and 337 kJmol-1, and strongly chemiluminescent with OH (ν''<9) as emitter. Reproduction of the H atoms in the atmosphere is supported by the

$$O + OH \rightarrow O_2 + H \tag{1.10}$$

reaction. Trace abundances of H or H_2O can contribute to a catalytic system.

1.5.2 Photochemistry of the Oxygen Airglow

The contributing processes in the mesospheric and lower thermospheric airglow are depicted schematically in Figure 1.7.
Atomic oxygen recombination (Barth, 1964) which is denoted by the reaction (1.11) and shown with (k) in Figure 1.7, produces the excited states molecules O_2*:

$$O(^3P) + O(^3P) + M \rightarrow O_2^* + M \tag{1.11}$$

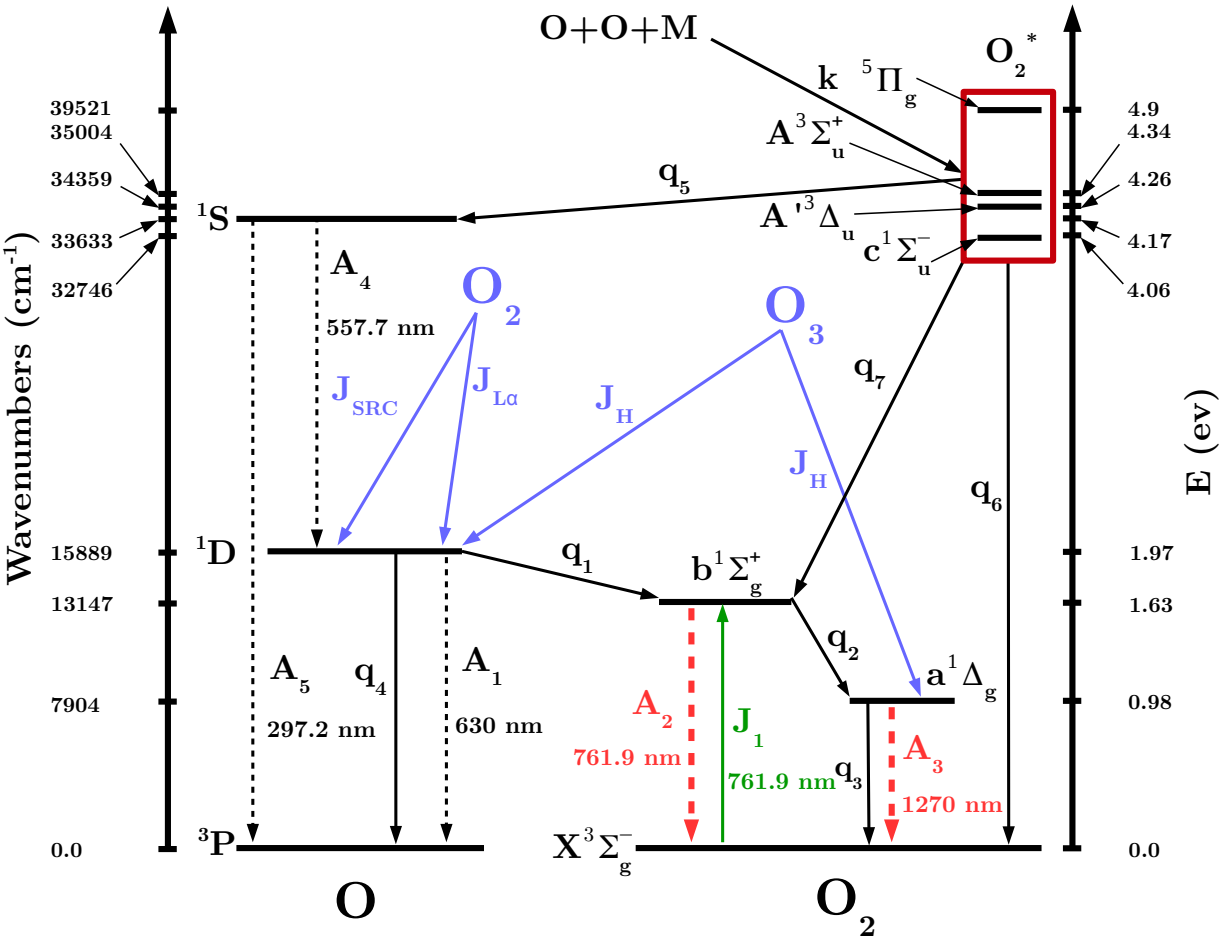

Figure 1.7: Schematic overview depicting processes that contribute to the oxygen systems in the airglow. See text for explanation (adapted from Zarboo et al. (2018).)

O_2* denotes each of the seven states below the first dissociation limit. Bates and others discuss that the population distribution among these states can best be estimated statistically, among them $^5\Pi_g$ is produced in about 40 percent of the collisions (Smith (1984); Bates (1988); Wraight (1982)). Most of the O_2* which results from recombination is found in the $A^3\Sigma_u^+$ state (Slanger and Copeland (2003)), and in a recent review Huestis (2013) concludes that all of the recombining atoms pass through the Herzberg states $c^1\Sigma_u^-$,$A'^3\Delta_u$, and $A^3\Sigma_u^+$. Stegman and Murtagh (1991) presented quenching parameters resulting from analyzing the measurements of the near ultraviolet portion of the nightglow to fit the synthesized spectra of the O_2 Herzberg states. These parameters set an upper limit of 10 percent for producing $O_2(c^1\Sigma_u^-)$ in the association reaction of atomic oxygen. Proper

consideration of the products of (1.11) could be complex (Kirillov, 2014). Recent research investigated this problem, for example Kirillov (2012).
Ozone photolysis (J_H in Figure 1.7 and reaction (1.11)) in the Hartley band ($\lambda < 310\ nm$) can result in the first electronic excited states of atomic oxygen $O(^1D)$ and molecular oxygen $O_2(a^1\Delta_g)$ (DeMore (1966)).

$$O_3 + h\nu(\lambda \leq 310nm) \rightarrow O(^1D) + O_2(a^1\Delta_g) \tag{1.12}$$

Molecular oxygen photolysis in the Schuman-Runge continuum (J_{SRC} in Figure 1.7, reaction 1.12) and in Lyman-alpha ($J_{Ly\alpha}$ in Figure 1.7, reaction 1.14) results in the electronically excited state atomic oxygen $O(^1D)$ (Nicolet (1971)):

$$O_2(X^3\Sigma_g^-) + h\nu(310 \leq \lambda \leq 175nm) \rightarrow O(^3P) + O(^1D) \tag{1.13}$$

$$O_2(X^3\Sigma_g^-) + h\nu(\lambda = 121.6nm) \rightarrow O(^3P) + O(^1D) \tag{1.14}$$

Quenching (collisional de-excitation) processes are depicted with solid black arrows and denoted by (q_i) in Figure 1.7. O_2* which is produced by reaction 1.11 can be quenched by atomic oxygen to produce $O(^1S)$ via reaction (1.15) (q_5 in Figure 1.7) (Barth and Hildebrandt (1961)) or be quenched by molecular oxygen to produce $O_2(b^1\Sigma_g{}^+)$ via reaction (1.16) (q_6 in Figure 1.7) (Greer et al. (1981)):

$$O_2^* + O(^3P) \rightarrow O(^1S) + O_2(X^3\Sigma_g^-) \tag{1.15}$$

$$O_2^* + O_2(X^3\Sigma_g^-) \rightarrow O_2(b^1\Sigma_g^+) + O_2(X^3\Sigma_g^-) \tag{1.16}$$

$O(^1D)$ by quenching with $O_2(X^3\Sigma_g{}^-)$ produces $O_2(b^1\Sigma_g{}^+)$ via reaction (1.17) which combines q_1 and q_4 in Figure 1.7 (Mlynczak and Olander (1995)):

$$O(^1D) + O_2(X^3\Sigma_g^-) \rightarrow O_2(b^1\Sigma_g^-) + O(^3P) \tag{1.17}$$

Light absorption of the solar radiation at 761.9 nm produces $O_2(b^1\Sigma_g{}^+)$ via:

$$O_2(X^3\Sigma_g^-) + h\nu(\lambda = 761.9\ nm) \rightarrow O_2(b^1\Sigma_g^+) \tag{1.18}$$

in the sunlit mesosphere (Mlynczak et al. (1993)) which is depicted in Figure 1.7 as a radiative excitation J_1.

According to reaction (1.19), $O_2(b^1\Sigma_g{}^+)$ can be deactivated by colliding with each of the abundant species such as O_2, N_2, CO_2, etc. (denoted by "M") which is denoted by q_2 in Figure 1.7 (Mlynczak and Olander (1995)):

$$O_2(b^1\Sigma_g^+) + M \rightarrow O_2(a^1\Delta_g) + M \tag{1.19}$$

Note that the above equation is a fast process (spin conserved).
$O_2(a^1\Delta_g)$ can be in turn quenched via (1.20) (q_3 in Figure 1.7) to yield $O_2(X^3\Sigma_g{}^-)$:

$$O_2(a^1\Delta_g) + M \rightarrow O_2(X^3\Sigma_g^-) + M, \tag{1.20}$$

which is a slow process (spin forbidden because the ground state is $O_2(X^3\Sigma_g{}^-)$).
Spontaneous radiative emissions are depicted as dashed arrows and are denoted by (A_i) in Figure 1.7. O(^{1}S) decays to O(^{1}D) by 557.7 nm emission (oxygen green line, reaction (1.21), A_4 in Figure 1.7) which is fast (because it conserves the spin) (Barth and Hildebrandt (1961)):

$$O(^1S) \rightarrow O(^1D) + h\nu(\lambda = 557.7nm). \tag{1.21}$$

Reactions 1.11,1.15, and 1.21 are known generally as the Barth mechanism (Barth and Hildebrandt (1961); see the review of Bates (1981)). The green line emission allows to derive atomic oxygen density near 100 km, as shown for example by Lednyts'kyy et al. (2015). The 297.2 nm oxygen line of the ultraviolet nightglow (Slanger et al. (2006)) is produced by O(^{1}S) via reaction 1.22 (Khomich et al. (2008)):

$$O(^1S) \rightarrow O(^3P) + h\nu(\lambda = 297.2\ nm), \tag{1.22}$$

which is depicted in Figure 1.7 by A_5.
O(^{1}D) which is produced by (J_H, 1.12), (J_{SRC}, 1.13), ($J_{LY-\alpha}$, 1.14), or (A_4, 1.21) can be deactivated to the O(^{3}P) ground state via slow emission (forbidden regarding the spin):

$$O(^1D) \rightarrow O(^3P) + h\nu(\lambda = 630.0\ nm), \tag{1.23}$$

which produces red line at 630.0 nm denoted by A_1 in Figure 1.7 (Khomich et al. (2008)).
Among the strongest features of the daytime and nighttime airglow are the infrared atmospheric band ($a^1\Delta_g \rightarrow X^3\Sigma_g{}^-$) and atmospheric band ($b^1\Sigma_g{}^+ \rightarrow X^3\Sigma_g{}^-$) of molecular oxygen (Wayne (1994)). These spontaneous radiative emissions, which I deal with in this work, are depicted by thick dashed red arrows in Figure 1.7. These two emissions are emitted by deactivation of the two molecular excited states $O_2(b^1\Sigma_g{}^+)$ at 761.9 nm via

reaction 1.24 (A_2 in Figure 1.7) and $O_2(a^1\Delta_g)$ in 1.27 μm via reaction 1.25 (A_3 in Figure 1.7) (Mlynczak et al. (1993)):

$$O_2(b^1\Sigma_g^+) \rightarrow O_2(X^3\Sigma_g^-) + h\nu(\lambda = 761.9\ nm), \tag{1.24}$$

$$O_2(a^1\Delta_g) \rightarrow O_2(X^3\Sigma_g^-) + h\nu(\lambda = 1.27\mu m). \tag{1.25}$$

Assuming that the processes depicted in Figure 1.7 describe the photochemistry and chemistry well, one can deduce ozone densities from the daytime atmospheric and infrared atmospheric volume emission rates in the $O_2(b^1\Sigma_g{}^+)$ and $O_2(a^1\Delta_g)$ (hereafter $O_2(^1\Sigma)$ and $O_2(^1\Delta)$ respectively) bands. For this purpose, the rates of all of the processes such as q_1 and q_4 in Figure 1.7 and in the reactions 1.17 and 1.19 should be known (e.g. Evans et al. (1968); Thomas et al. (1983); Mlynczak and Olander (1995); Mlynczak et al. (2001)).

1.5.3 Observation of the Oxygen Airglow

Molecular oxygen airglow was measured from several previous space-born platforms and rocket experiments.

The measurements of the $O_2(^1\Sigma)$ band include the Fabry-Perot interferometer on-board Dynamics Explorer-2 (DE-2) (Skinner and Hays (1985)) which is used to study the measurements of the overall brightness of the emission. The High Resolution Doppler Imager (HRDI) aboard the Upper Atmosphere Research Satellite (UARS) (Hays et al. (1993)) measured Doppler shifts in the rotational lines of the $O_2(^1\Sigma)$ atmospheric band in order to determine the winds in stratosphere, mesosphere and lower thermosphere. The WIND Imaging Interferometer (WINDII) on the same satellite (Shepherd et al. (1993)) measured wind, temperature and emission rates. The TIMED Doppler Interferometer (TIDI) on-board Thermosphere, Ionosphere, Mesosphere Energetics and Dynamics (TIMED) (Killeen et al. (2006)) did remote sensing measurements of the upper atmospheric winds and temperatures based on $O_2(^1\Sigma)$ emissions. Remote Atmosphere and Ionosphere Detector System (RAIDS) on the KIBO module of the International Space Station (Christensen et al. (2012)) measured limb brightness of the vibrational (0,0), (0,1), and (1,1) $O_2(^1\Sigma)$ band from 80 to 180 km. The Optical System for InfraRed Imaging Spectroscopy (OSIRIS) on-board Odin satellite (Sheese et al. (2010)) was used to extract the temperatures in the mesosphere-lower thermosphere (MLT) region from $O_2(^1\Sigma)$.

The previous measurements of the $O_2(^1\Delta)$ band include observations from Near-Infrared Spectroscopy Experiment on the Solar Mesosphere Explorer (SME). SME measured the emissions from $O_2(^1\Delta)$ produced by O_3 photolysis (Thomas et al. (1984)). The Infrared Atmospheric Airglow Radiometer (IRA) aboard the OHZORA satellite measured mesospheric ozone profiles derived from $O_2(^1\Delta)$ emissions (Yamamoto et al. (1988)). One part

of the Optical System for InfraRed Imaging Spectroscopy (OSIRIS) on the Odin satellite is a three channel InfraRed Imager (IRI) which observes scattered sunlight and airglow of the atmospheric infrared band of oxygen at 1.27 μm (Llewellyn et al. (2004)). TIMED (Thermosphere-Ionosphere-Mesosphere Energetics and Dynamics)/SABER (Sounding of Atmosphere using Broadband Emission Radiometry) data were used to measure the $O_2(^1\Delta)$ airglow emission with one channel with the central wavelength of 1.27 μm (Gao et al. (2011b)).

All of the above studies include satellite observations from only one of the O_2 bands, i.e., either $O_2(^1\Sigma)$ or $O_2(^1\Delta)$. Simultaneous measurements of the $O_2(^1\Sigma)$ and $O_2(^1\Delta)$ airglows is part of the rocket experiment of the (METEORS) MEsospehric-Thermospheric Emissions for Ozone Remote Sensing. This was launched from White Sands missile range, New Mexico (Mlynczak et al. (2001)) and was used to derive ozone concentrations separately from each of the O_2 bands.

Our work for the first time provides global long time observation and retrievals of the molecular oxygen airglow from SCIAMACHY/ENVISAT, see Section 2.1, in both of the $O_2(^1\Sigma)$ and $O_2(^1\Delta)$ bands at the same time.

2 Satellite data-sets

In this chapter, I will summarize the data-sets used in the thesis. In Section2.1, SCIAMACHY data are described, in Section 2.2 other satellite data-sets used for validation of data-products obtained in this thesis are described.

2.1 The SCIAMACHY instrument

2.1.1 General features

The SCanning Imaging SpectroMeter for Atmospheric CHartographY (SCIAMACHY) is a passive remote sensing spectrometer which observes backscattered, reflected, transmitted, or emitted radiation from the Earth's atmosphere and surface in the wavelength range 240–2380 nm. Detectors are 8 photodiode arrays, separating the spectra in 8 channels with different noise etc., ranging from the UV to the near IR, with a wavelength resolution of 0.2 nm. This instrument was part of the atmospheric chemistry payload on-board the European Envisat (Environmental Satellite), which was operational from March 2002 to April 2012. It crossed the equator at 10:00 local time with its sun-synchronous orbit, 98.55° inclination, 799.8 km mean altitude, 100.59-min orbit period, and 35 days repeat cycle, coordinated with MIPAS MA/UA mode once every 30 days. MIPAS (the instrument on the same Envisat satellite (see Subsection 2.2.2)) MA/UA mode was introduced on a regular basis as of once every 10 days in March 2007 (García-Comas et al., 2014). These two modes of operation are the middle atmosphere mode (MA; covering 18–102 km, in 3 km vertical steps) and the upper atmosphere mode (UA; covering 40–102 km, in 3 km steps, and 102–170 km, in 5 km steps) (Oelhaf, 2008). With Equator crossing local time of 10 a.m., SCIAMACHY has three different viewing geometries: nadir, limb, and sun-moon occultations (Figure 2.1), with the nominal limb scans ranging from 0–90 km (Bender et al., 2013). From July 2008 to April 2012, it observed the mesosphere and lower thermosphere (50–150 km) regularly twice a month for 15 consecutive orbits, that is, once around the globe. This special MLT limb mode scans the mesosphere and lower thermosphere in 30 limb points from 50 to 150 km with the vertical displacement of about 3 km and are restricted to the dayside (downleg) semi-orbit. These scans were scheduled in place of the nominal mode scans and there were 30 limb scans along one semi-orbit. Overall, there

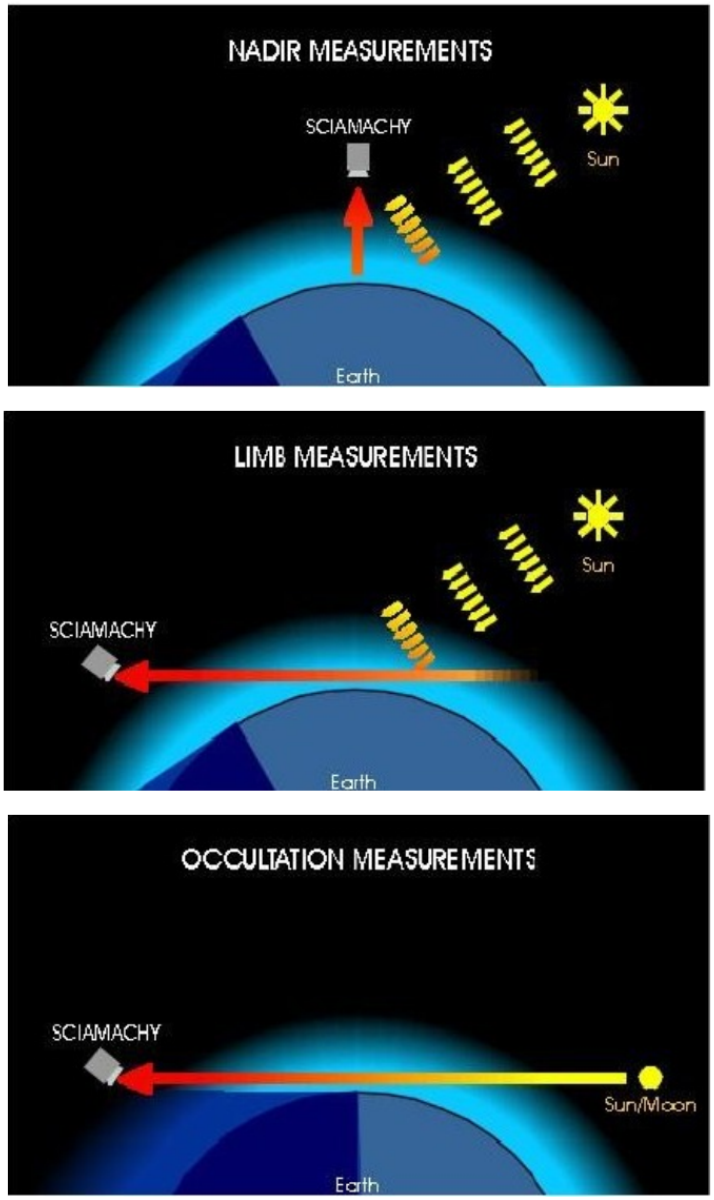

Figure 2.1: Schematic of the measurement modes of SCIAMACHY, (top) nadir measurement mode, (middle) limb measurement mode, and (bottom) occultation measurement mode. (Adapted from university of Bremen, Institute of Environmental Physics, at: http://www.iup.uni-bremen.de/sciamachy/instrument/modes/index.html, Gottwald and Bovensmann (2010)).

were 84 days of mesosphere lower thermosphere limb measurements. In this work, I use the visible and near infrared spectra in the MLT limb viewing geometry from channel 4 (595–811 nm) and channel 6 (1200-1360 nm) to retrieve emission intensities and volume emission rates (VERs) from the $O_2(^1\Sigma)$ and $O_2(^1\Delta)$ airglow bands. The SCIAMACHY wavelength range include also the red and green oxygen lines, at ∼630 nm and ∼557 nm respectively.

In order to produce data for our work, I use SCIAMACHY level 1b version 8.02 and the SCIAMACHY command line tool *sciaL1c* from the SCIAMACHY calibration tools. I used two windows for each of the two bands: 750–780 nm for the $O_2(^1\Sigma)$ band, and 1200–1360 nm for the $O_2(^1\Delta)$ band. These two bands are electronic transitions with a rotational-vibrational structure clearly visible from Figures 2.2 and 2.3. The bands observed in Figures 3.3b and 2.3b for $O_2(^1\Delta)$ are a mixture of the (0,0), (1,1), (1,0), and (0,1) transitions, with the (0,0) and (1,1) transitions dominating (Rothman et al., 2005). In Figures 2.2c and 2.3c, mostly (0,0) and (1,1) transitions are observable for $O_2(^1\Sigma)$ (Rothman et al., 2005). The measured spectra at ≈360 km is used as the dark spectrum which I subtract from the spectra in all of the other tangent heights. This spectrum contains some residual (read-out) spectral patterns which remained from the calibration step and subtracting it from other spectra which have almost the same pattern cancels them out. For the $O_2(^1\Delta)$ band, there are two masked pixels in almost all of the scans which are located around 1262 nm and 1282 nm. These are not used.

2.1.2 Daytime spectra

A typical dayside (downleg) SCIAMACHY orbit begins with a measurement of the twilit atmosphere, and following that a solar occultation measurement during the sunrise at high northern latitudes, and a sequence of the optimized limb-nadir scans (Bovensmann et al. (1999)). Our criterion for separating day-time from night-time observations is that the tangent point solar zenith angle is less than or equal 88 degrees. Using this method, I avoid twilight measurements and all of the measurement points are located in the dayside.

Examples of the daytime calibrated spectra for orbit number 41455, are shown in Figure 2.2a for $O_2(^1\Sigma)$ and Figure 2.2b for $O_2(^1\Delta)$ at mean latitude of 17.3 degrees N and mean longitude of 94.3 degrees E, measured on 03/02/2010.

The spectral region for observing the daytime $O_2(^1\Sigma)$ band consists of a Rayleigh scattering background which distorts the retrieval. Consequently it is necessary to subtract the estimated Rayleigh scattering in order to yield the $O_2(^1\Sigma)$ emission spectrum. This background scattered features are attributed in part to up-welling radiation, multiple scattering in the lower atmosphere, and terrestrial albedo. This results in the absorption signal for $O_2(^1\Sigma)$ (Sheese et al. (2010)). In order to account for the multiple scattering and the absorption from the ground state $O_2(X^3\Sigma_g^-)$ to $O_2(^1\Sigma)$, a background signal forming

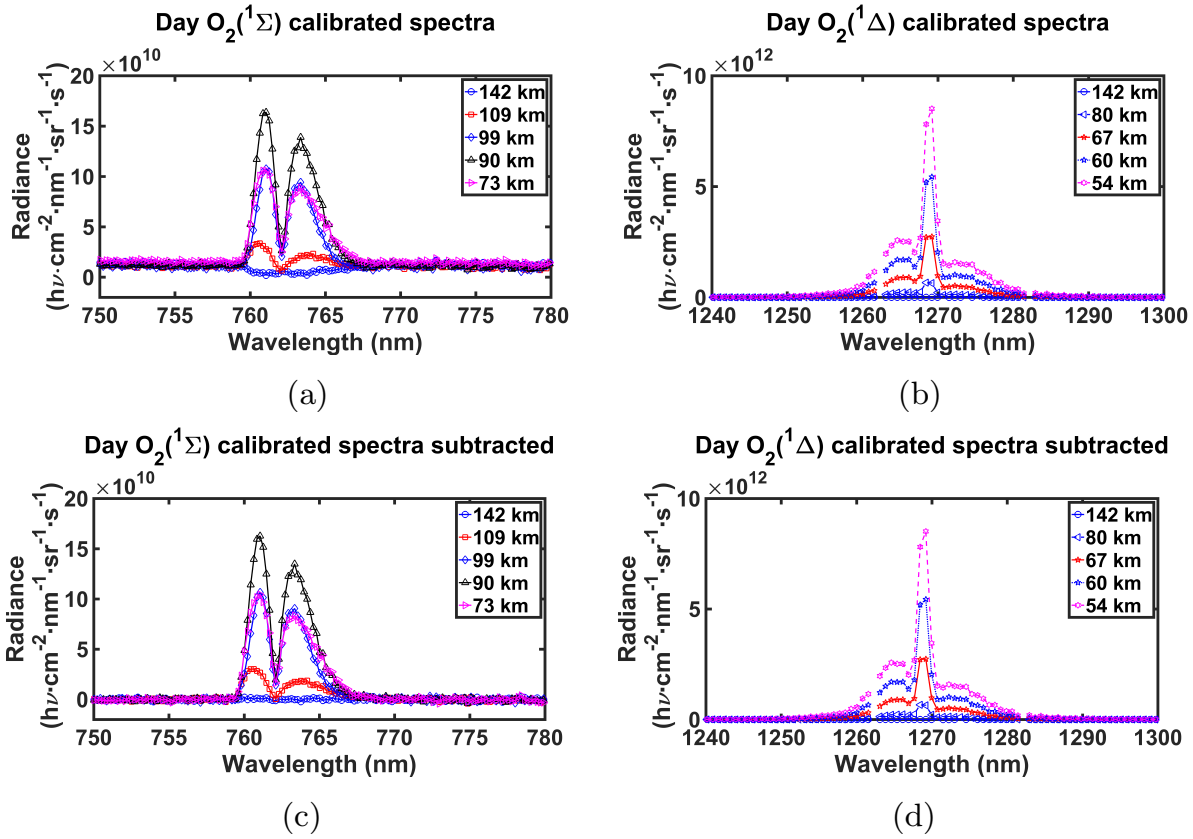

Figure 2.2: Examples of the daytime calibrated spectra, and the background-corrected spectra. (a) $O_2(^1\Sigma)$ on 03/02/2010, orbit 41455, mean latitude 17.3°N, mean longitude 94.3°E. (b) as (a) but for $O_2(^1\Delta)$ band. (c) as (a) but with background correction applied. (d) as (b) but with background correction applied. Note the missing pixels in $O_2(^1\Delta)$ (b) and (d) (adapted from the published material Zarboo et al. (2018).).

the $O_2(^1\Sigma)$ spectrum at the highest altitude ($\approx$ 148 km) is scaled to the out of band spectra in each tangent altitude and then subtracted. I consider 750–759 nm and 767–780 nm as out-of-band. After this correction, I subtract a linear background in each level. An example of the subtracted background spectrum containing $O_2(^1\Sigma)$ emission is shown in Figure 2.2c.

For the $O_2(^1\Delta)$ band, the absorption signal in the background spectrum is negligible compared to the daytime $O_2(^1\Sigma)$ band spectra, therefore I subtract only a linear background from the observations. An example of the daytime $O_2(^1\Delta)$ band spectrum with the background subtracted, is shown in Figure 2.2d.

2.1.3 Twilight spectra

Since the solar zenith angle of the tangent points to be under the horizon varies with altitude, I use equation 2.1 to calculate the solar zenith angle where the sun is just at the horizon for each of the tangent points (R is the Earth's radius and h is the altitude of the tangent point):

$$\alpha_{horizon} = \frac{\pi}{2} + cos^{-1}\left(\frac{R}{R+h}\right). \tag{2.1}$$

As a criterion to select the twilight spectra, I remove each limb scan in which there is at least one measurement point which has a solar zenith angle less than the result of equation 2.1. I obtain spectra of $O_2(^1\Sigma)$ as shown in Figure 2.3a without and Figure 2.3b with background correction for the example orbit 41455. Figure 2.3b shows the twilight $O_2(^1\Sigma)$ spectrum, and Figure 2.3d shows the background corrected twilight $O_2(^1\Delta)$ spectra for the same example orbit (41455). It is apparent that the background signal for the twilight $O_2(^1\Sigma)$ and $O_2(^1\Delta)$ is negligible. $O_2(^1\Sigma)$ peak emission is one order of magnitude lower during twilight than during daytime. For $O_2(^1\Delta)$ the peak emission during twilight is about two orders of magnitude lower than the peak emission during the daytime.

2.2 Other satellite instruments

2.2.1 OSIRIS/ODIN

Launched on 20 February 2001, ODIN was used until spring of 2007 aiding in the study of star formation, and in February 2019 it celebrates its 19 years in orbit, functioning nominally. The Optical Spectrograph and InfraRed Imaging System (OSIRIS) on board the Odin satellite, is a limb-viewing instrument that consists of three infrared imagers and an optical spectrograph (OS), which observes Rayleigh-Scattered sunlight and airglow emission at wavelengths of 275–810 nm. OSIRIS started measuring since November 2001, and continues to measure to the present. A single scan vertical field of view corresponding to 1 km at the tangent point, absolute limb pointing knowledge is better than 0.5 km at the tangent point. The wavelength range includes the oxygen atmospheric band $O_2(^1\Sigma)$ at ∼762 nm. The shape of this emission is temperature dependent, and temperature profiles in the MLT region are inverted by fitting the observed to modelled emission spectra (Sheese et al., 2010). The objectives of the satellite mission are investigations of stratospheric ozone, mesospheric ozone, the summer mesosphere and coupling of atmospheric regions. The satellite is in a sun-synchronous orbit at 600 km, with the ascending node at 1800 local time, and pointed in the limb, sweep over ∼10–100 km altitude range.

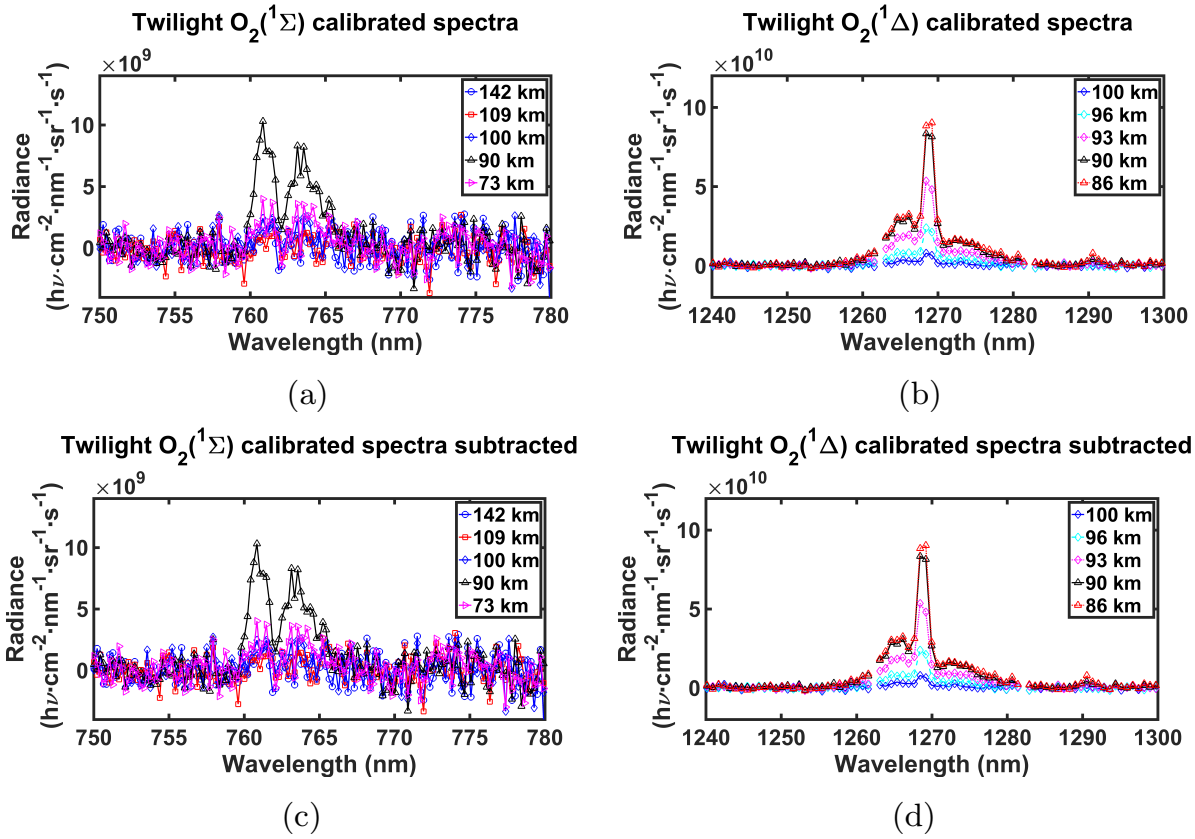

Figure 2.3: Examples of the twilight calibrated spectra, and the spectra from which the background $O_2(X^3\Sigma_g^-)$ to $O_2(^1\Sigma)$ absorption has been subtracted. (a) for the 03/02/2010, orbit number 41455, mean latitude of 78.0°N, mean longitude of 226.5°E for $O_2(^1\Sigma)$ band. (b) as (a) but for the $O_2(^1\Delta)$ band. (c) as (a) but with background subtracted. (d) as (b) but with background subtracted.

2.2.2 MIPAS/ENVISAT

MIPAS, the Michelson Interferometer for Passive Atmospheric Sounding is a mid-infrared emission spectrometer which is part of the core payload of ENVISAT (Fischer et al., 2008), on the same satellite as SCIAMACHY, but looking in the opposite direction: SCIAMACHY looks in flight direction, MIPAS to the back of the flight direction. Launched on March 2002, it scans across the horizon detecting atmospheric spectral radiances which are inverted to vertical temperature, H_2O, O_3, CH_4, HNO_3 and NO_2 and many more trace gas profiles, and cloud distributions. MIPAS was operating in the spectral region between 4.15 and 14.6 μm (685-2410 cm^{-1}). It scans at 5–150 km tangent height, with 3 km vertical resolution. The instrument provided two special observation modes dedicated to the middle atmosphere

(MA, 18—102 km) and upper atmosphere (UA, 42—172 km). After a test phase of 12 measurement days from January 2005 to October 2007, about 1 day every 3 months, the measurements using these modes were scheduled regularly on 2 days every 10 days of nominal mode measurements (7–72 km) beginning November 2007 (Raspollini et al., 2013). SCIAMACHY MLT mode was coordinated with the MIPAS MA/UA measurements in such a way that they coincide every 30 days.

2.2.3 SABER/TIMED

The Sounding of Atmosphere using Broadband Emission Radiometry (SABER) instrument is one of the four instruments on NASA's TIMED (Thermosphere Ionosphere Mesosphere Energetics and Dynamics) satellite. It was launched in December 2001, with the main goal of observing ozone abundance and the energy balance of the terrestrial mesosphere by means of measuring the $O_2(^1\Delta)$ airglow emission at 1.27 μm (Mlynczak and Olander, 1995). SABER measures the atmosphere globally using a broadband limb-scanning infrared radiometer in the 1.27–17 μm spectral range (James M. Russell, 1999). Equator local crossing time of SABER changes because of its inclination of 74.1 ° (±0.1 °).

3 Volume Emission Rates of O_2

In this chapter, the O_2 airglow is investigated in detail. The retrieval of emission intensities and volume emission rates from the observed spectral features are given in Section 3.1, in Section 3.2 a validation of $O_2(^1\Delta)$ VERs is provided, and results are discussed in Sections 3.3. An investigation of the underlying processes driving the O_2 dayglow using a photochemical model is provided in Subsection 3.3.3. The retrieval strategy and some of the results have already been published in Zarboo et al. (2018).

3.1 Retrieval of emission intensities and volume emission rates

3.1.1 Emission intensities

In this section I present a method for the derivation on the emission intensities for both $O_2(^1\Sigma)$ and $O_2(^1\Delta)$ from daytime and twilight airglow emission. Emission intensity is defined as the flux of energy in a given direction per second per unit wavelength range per unit solid angle per unit area perpendicular to the given direction (Liou, 2002). For inversion of the observed radiation I set up 30 layers around the Earth, such that each layer is centered at one tangent altitude. I denote the observed spectral emissions with Y, the pathlength through each of the observation pathlines through each of the atmospheric layers with L, and the wavelength dependent emission intensity from the layer with X. L is calculated from the geometry of the observation, so that each element of the matrix L could be iteratively calculated by the Pythagorean relation between the radius of the two consecutive atmospheric layers:

$$L_{ij+1} - L_{ij} = [h_{j+1}^2 - h_j^2]^{\frac{1}{2}}, \tag{3.1}$$

in which L_{ij+1} and L_{ij} is the ith pathlength through the $j+1$ and jth atmospheric layers, h_{j+1} and h_j is the height of the $j+1$th and jth atmospheric layers respectively, as shown schematically in Figure 3.1. Assuming no self-absorption, the following linear relation is obtained:

$$Y = LX. \tag{3.2}$$

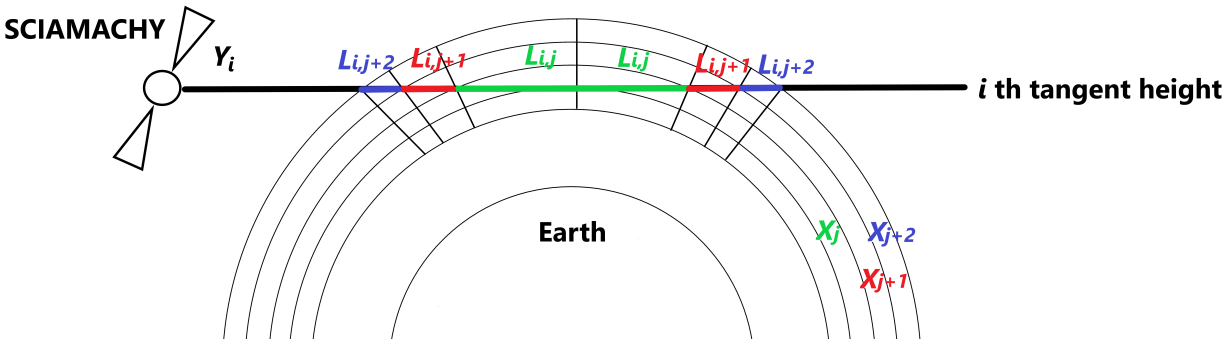

Figure 3.1: Schematic view of the pathlengths (L_{ij}s) through the atmospheric layers. Emission intensities through each layer is shown by X_js; The observed spectra through the ith tangent height is denoted by Y_i.

In equation 3.2, dim(Y) = the number of atmospheric layers × the number of spectral points=30×144 for the $O_2(^1\Sigma)$ and 30×210 for $O_2(^1\Delta)$. dim(L) = the number of the atmospheric layers×the number of tangent heights in each scan= 30×30. dim(X)=the number of atmospheric layers×the number of spectral points in the corresponding wavelength interval = 30×144 for $O_2(^1\Sigma)$ and 30×210 for $O_2(^1\Delta)$. $||Y - LX||^2 = \epsilon$ is minimized by solving the least-squares problem. The solution (linear inverse problem) is obtained by

$$(L^T S_y^{-1} L)X = L^T S_y^{-1} Y \tag{3.3}$$

if

$$L^T S_y^{-1} L \tag{3.4}$$

can be inverted. This is equivalent to:

$$X = (L^T S_y^{-1} L)^{-1} L^T S_y^{-1} Y. \tag{3.5}$$

Here the error covariance matrix S_y has diagonal elements corresponding to the out-of-band variances of the background corrected spectra in each altitude.
The emission intensities were calculated for the spectra described in sections 2.1.2 and 2.1.3. Examples of the emission intensities for daytime $O_2(^1\Sigma)$ are shown in Figure 3.2a and for daytime $O_2(^1\Delta)$ in Figure 3.2b. The spectral shape of the rotational-vibrational $O_2(^1\Sigma)$ band and the $O_2(^1\Delta)$ band are clearly visible in the daytime $O_2(^1\Sigma)$ and $O_2(^1\Delta)$ bands respectively. It is found that the largest values for the $O_2(^1\Sigma)$ band are located around 90 km altitude. Daytime $O_2(^1\Delta)$ emission intensities are largest in the lowermost observational altitudes, i.e., 54 km (Figure 3.2b). It is also found that the largest $O_2(^1\Delta)$ emission intensities are about two orders of magnitude greater than the largest values of the $O_2(^1\Sigma)$ band in the corresponding limb scan. Figure 3.2c shows the twilight $O_2(^1\Sigma)$

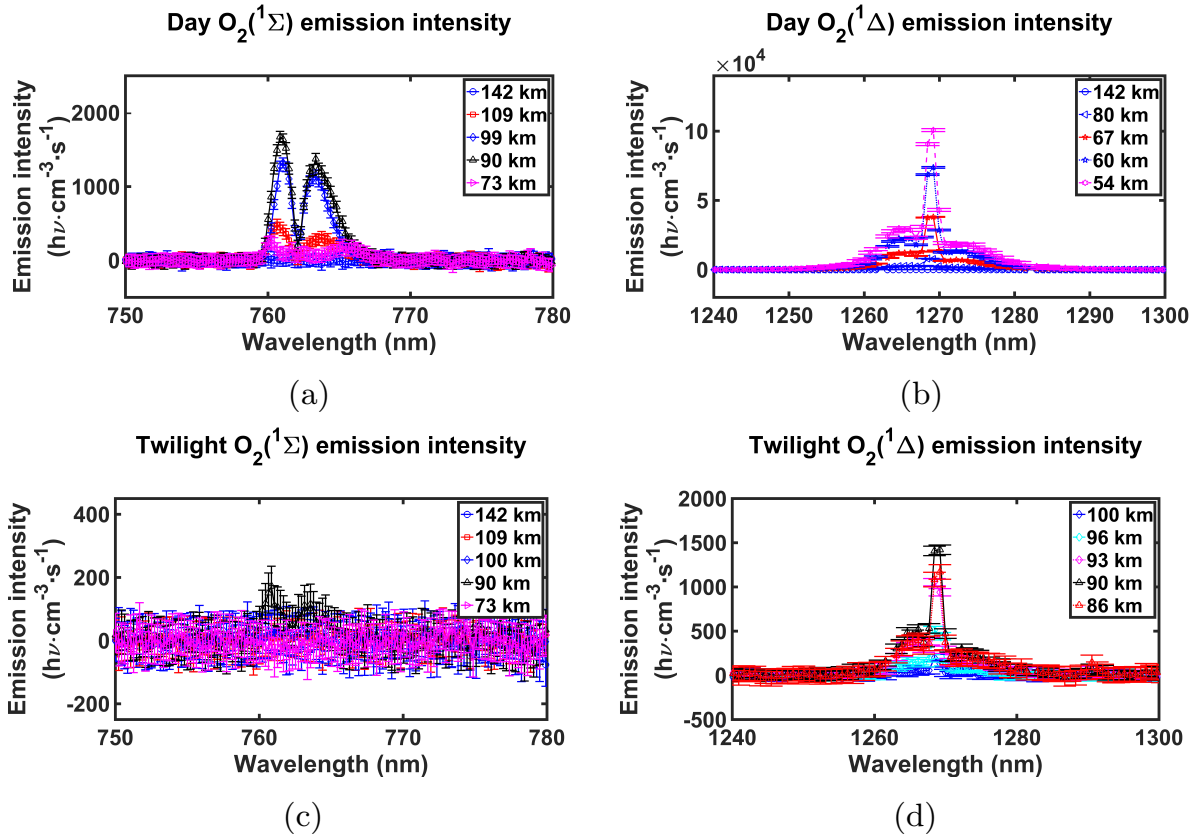

Figure 3.2: Examples of the emission intensities that are obtained by solving eq. 3.5. (a) for the daytime $O_2(^1\Sigma)$ band, on the date 03/02/2010, orbit number 41455, mean latitude of 17.3°N, mean longitude of 94.3°E. (b) as (a) but for $O_2(^1\Delta)$ band. (c) for the twilight $O_2(^1\Sigma)$ band on the date 03/02/2010, orbit number 41455, mean latitude 78.0°N, mean longitude 226.5°E. (d) as (c) but for $O_2(^1\Delta)$ band. Error bars represent the retrieval errors (adapted from published material Zarboo et al. (2018)).

emission intensities, and Figure 3.2d shows the twilight $O_2(^1\Delta)$ emission intensities for the same orbit but retrieved from the three MLT twilight limb scans (see subsection 2.1.3). The twilight $O_2(^1\Sigma)$ band is one order of magnitude smaller than daytime in the largest values. The twilight $O_2(^1\Delta)$ band signal is more prominent, but is about two orders of magnitude smaller than the daytime. Twilight $O_2(^1\Delta)$ emission intensities are largest in the 83–96 km altitude, comparable to $O_2(^1\Sigma)$ (Figure 3.2d shows only a selection of altitudes).

The overbars in the panels of Figure 3.2 describe a measure of the instrument noise derived from the square roots of each of the diagonal elements of the retrieval error covariance matrix S_a for each of the altitudes:

$$S_a = GS_yG^T, \tag{3.6}$$

in which the contribution function matrix G is defined as follows:

$$G = (L^T S_y^{-1} L)^{-1} L^T S_y^{-1}. \tag{3.7}$$

The signal-to-noise ratio is derived from the ratio of the emission intensity in each channel to the square root of the diagonal of the error covariance matrix as defined in Equation3.6. Hereafter, I use "significant" for the data with signal to noise ratios of greater than one. The strongest daytime $O_2(^1\Sigma)$ signals occur in around 83–99 km, see Figure 3.2a. Twilight $O_2{}^1\Sigma)$ emission intensities have large noise which masks the signal, see Figure3.2c. $O_2(^1\Delta)$ emission intensities are significant for the whole altitude region during daytime (see Figure 3.2b), in 86–93 km altitude during twilight (see Figure 3.2d).
Daytime emission intensities of $O_2(^1\Sigma)$ are in the following used to retrieve the temperatures at MLT altitudes as described in Chapter 4.

3.1.2 Volume emission rates

In this section, I describe the derivation of volume emission rates from the emission intensities obtained in Section 3.1.1 for $O_2(^1\Sigma)$ and $O_2(^1\Delta)$ daytime airglow. I integrate spectral emission intensities from 759 nm to 767 nm for $O_2(^1\Sigma)$ and 1255 nm to 1285 nm for $O_2(^1\Delta)$ on the wavelength interval and on the full sphere solid angle to obtain band integrated volume emission rates of the $O_2(^1\Sigma)$ and $O_2(^2\Delta)$:

$$\int_0^{4\pi} \int_{\lambda_1}^{\lambda_2} ei \, d\lambda \, d\Omega \tag{3.8}$$

Volume emission rate profiles for a sample satellite orbit (41455 on 03/02/2010) for daytime $O_2(^1\Sigma)$ and $O_2(^1\Delta)$ are shown in Figures 3.3a and 3.3b respectively. Examples of the latitude-altitude distributions of the volume emission rates for the whole orbit for daytime $O_2(^1\Sigma)$ are shown in Figure 3.4a and for the daytime $O_2(^1\Delta)$ is shown in Figure 3.4b. For the calculation of the noise in the derived volume emission rates, I used error propagation from the noise in the emission intensities into the derived volume emission rates. The blank regions represent the regions with the signal to noise ratios of less than one. $O_2(^1\Sigma)$ VER has its maximum in the 90-98 km altitude range which is two orders of magnitude smaller than the maximum $O_2(^1\Delta)$ VER. Figure 3.3b shows that the SCIAMACHY MLT

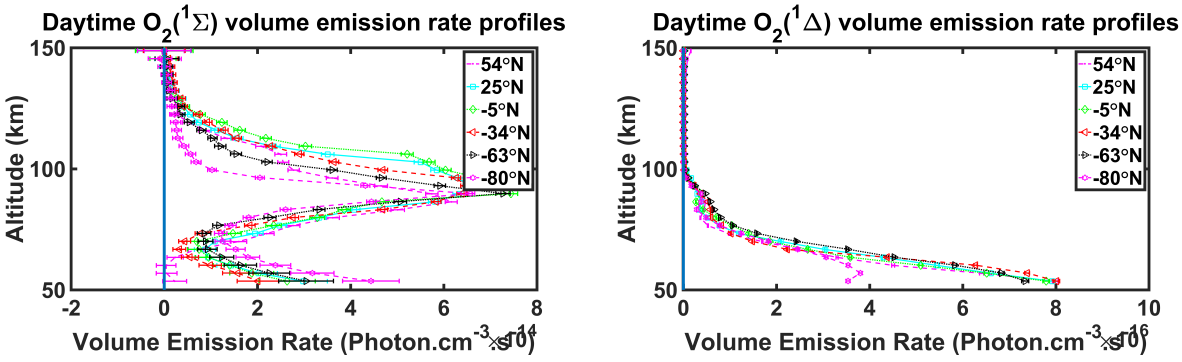

Figure 3.3: Typical profiles of the VER for different latitudes. (a) for daytime $O_2(^1\Sigma)$ VER, on the date 03/02/2010, orbit number 41455. (b) as (a) for daytime $O_2(^1\Delta)$ band. Error bars represent the retrieval errors. The zero line is marked with a vertical blue straight line. Adapted from published material Zarboo et al. (2018).

volume emission rate profiles have largest values at the bottom of the observation range, around 54 km. Some volume emission rate profiles sometimes show secondary maximums in the 80–90 km altitude range, which are at least one order of magnitude smaller than the largest daytime $O_2(^1\Delta)$ VER. The measurement errors of the volume emission rates for different orbits show that the $O_2(^1\Sigma)$ volume emission rates are significant from 65 to 140 km altitude range, and do not depend on latitude. Investigating altitude profiles of the volume emission rates (not shown here) we see that the $O_2(^1\Sigma)$ volume emission rates have the largest SNR below 125 km and above 85 km. Based on the $O_2(^1\Delta)$ the SNR shown in Figure 3.4f, $O_2(^1\Delta)$ is significant below 100 km.

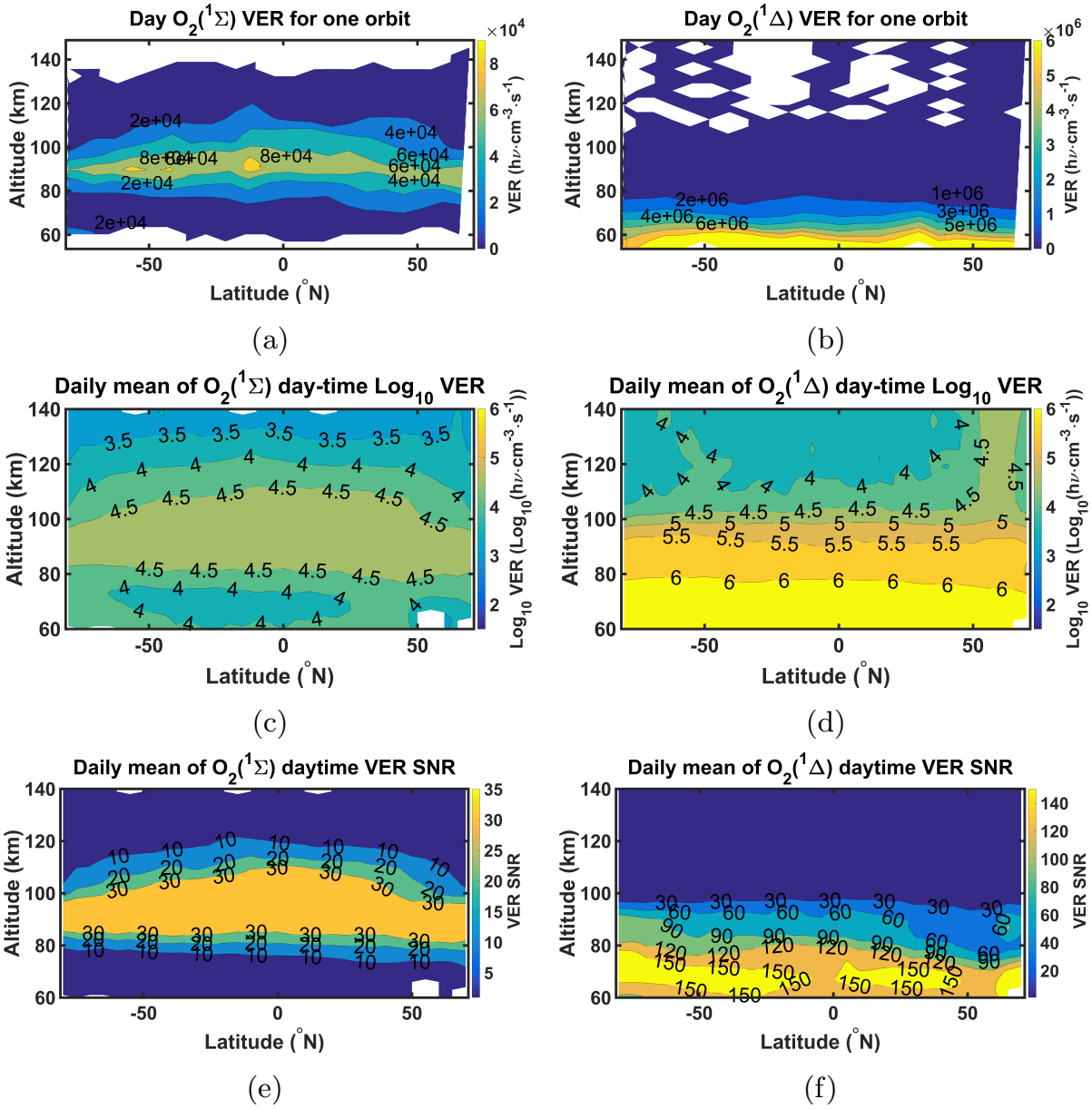

Figure 3.4: Latitude-altitude contours of the daytime VER. (a) for one satellite orbit, the $O_2(^1\Sigma)$ band, date: 2010/02/03, orbit number: 41455. (b) as (a) for $O_2(^1\Delta)$. Signal to noise ratios less than one and large noisy values are excluded. (c) and (d) as (a) and (b) respectively, averaged on the all of the orbits on the whole day of 03/02/2010, with the same logarithmic scale. Negative values are excluded. (e) Signal to noise ratios of the daily mean of $O_2(^1\Sigma)$ VERs. Areas where the signal to noise ratio is less than 1 are excluded. (f) as (e) for $O_2(^1\Delta)$ band (adapted from the published material Zarboo et al. (2018)).

In a region north of the South Atlantic and off the Brazilian coast, the Earth's magnetic field is anomalously low and the ionizing radiation can increase several orders of magnitude. This region is called the Southern Atlantic Anomaly (SAA, e.g. Kurnosova et al. (1962)) and any spacecraft passing this region can give wrong instrument readings. In our retrievals, volume emission rates SNRs in orbits which cross this region are affected by the SAA. SAA affects $O_2(^1\Sigma)$ measurements more than $O_2(^1\Delta)$ measurements. The most dramatic effect of the SAA on our dataset is on $O_2(^1\Sigma)$ volume emission rate SNR, although the values are still significant in the altitude range of 80–100 km.

3.2 Validation of $O_2(^1\Delta)$ VERs

In the following I will compare my results of the $O_2(^1\Delta)$ VER to observations from the SABER instrument (see Section 2.2). SABER volume emission rates are available only for $O_2(^1\Delta)$ as it is essentially an infrared radiometer (see Subsection 2.2.3), and OSIRIS $O_2(^1\Sigma)$ VERs are not available[1], I restrict my comparisons to the SABER $O_2(^1\Delta)$ band. For this comparison, 19 days between 12/01/2009 and 15/03/2012 are chosen such that solar local times of SCIAMACHY and SABER have the best coincidences, restricting the local solar time of SABER to 9-11 am, because as discussed in Section2.2.3, the Equator local crossing time changes during the time.
Figure 3.5 shows comparisons of the latitude-altitude distributions of the daytime zonal mean $log_{10}(O_2(^1\Delta)VER)$ between SCIAMACHY (left panel) and SABER (right panel) instruments exemplarily for three days. Comparisons for other selected days are shown in Appendix 7.1. These comparisons show that magnitude and structure of the $O_2(^1\Delta)$ VER is reproduced by both instruments reasonably well. The differences include larger VERs in SCIAMACHY above about 105 km, which according to Figure 3.4f, are located in the region where the signal to noise ratios are small. Other differences arise from variation of latitudinal coverage of SABER data which arise from the non sun-synchronous orbit of SABER. Comparisons for other selected days are shown in Appendix 7.1.
Averaging over the whole common days, results in Figure 3.6a and 3.6b a comparison of mean $O_2(^1\Delta)$ VERs averaging over all common days is shown.
It is apparent that the $O_2(^1\Delta)$ VERs from SCIAMACHY and SABER are in good agreement, especially in the ∼70–120 km altitude range, in which the SCIAMACHY instrument shows the best signal to noise ratio. The secondary maximum of $O_2(^1\Delta)$ is clearly seen by both instruments. Below 70 km altitude, SCIAMACHY VERs are systematically lower then SABER VERs. Reasons for this disagreement will be investigated below.

[1]For the OSIRIS retrievals, it wasn't necessary to determine the absolute A-band intensities (nor the VERs), so these were never actually calculated; personal communication with P. Sheese, 19/12/2017.

As a summary of the above statement, a) the lat/alt structure shown in both instruments is highly consistent; b) lower values shown in most cases by SABER above 100 km, are probably due to lower noise. To investigate this in more detail, relative differences as defined by:

$$100 \times \left(1 - \frac{O_2(^1\Delta)VER_{SABER}}{O_2(^1\Delta)VER_{SCIAMACHY}}\right) \tag{3.9}$$

are shown in Figure 3.6c and 3.6d. and the spectra of the SCIAMACHY in Figures 3.6e and 3.6f respectively. The right panel of the Figure 3.6 is similar to the left panel, except that

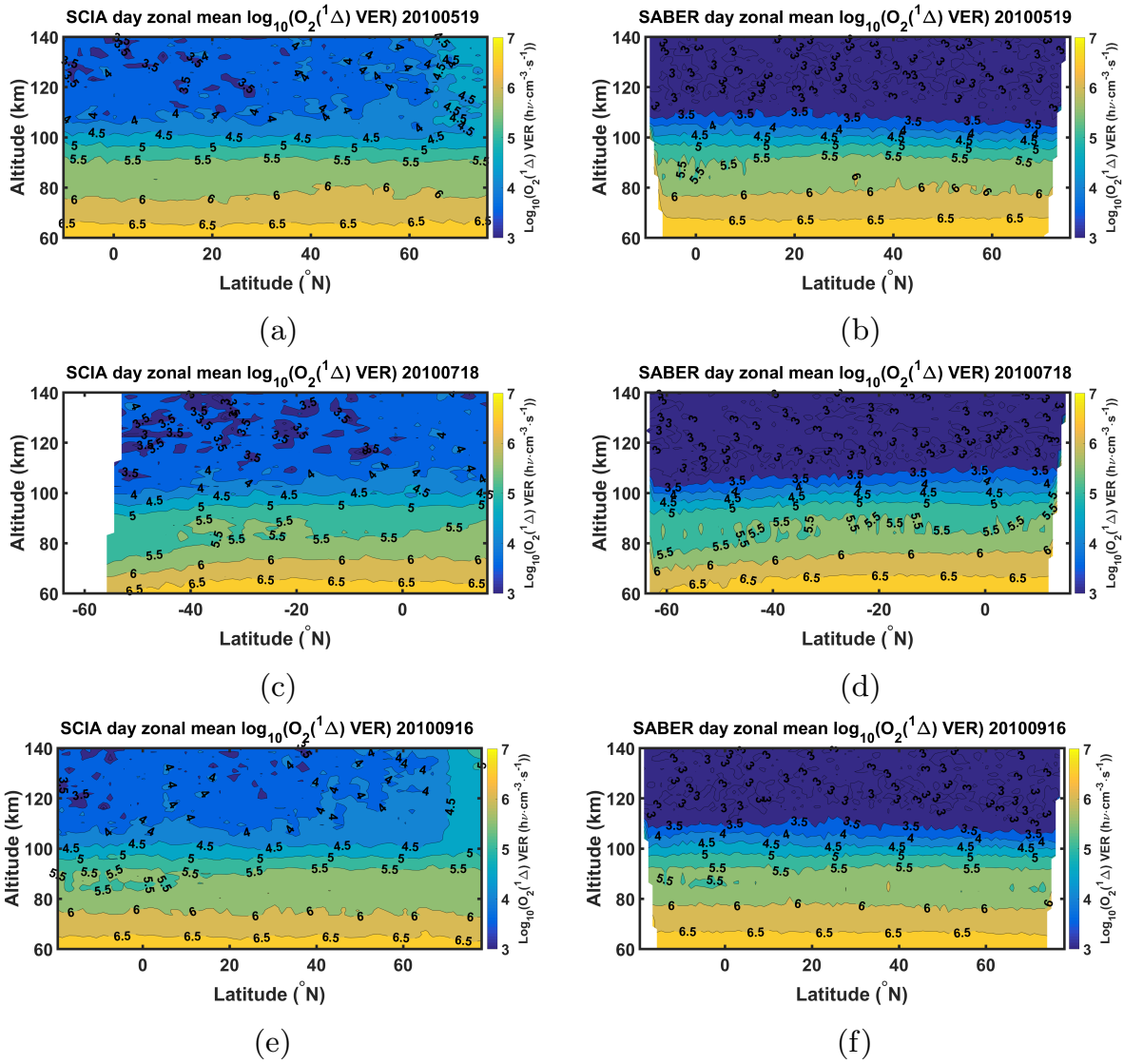

Figure 3.5: Comparison of latitude-altitude variation of zonally averaged $O_2(^1\Delta)$ $log_{10}(VER)$ of SCIAMACHY (left panel) and SABER (right panel) on 19/05/2010 (up), 28/07/2010 (middle), and 16/09/2010 (bottom).

the background spectra of $O_2(^1\Delta)$ is subtracted from the signal, as it is done for $O_2(^1\Sigma)$ described in Zarboo et al. (2018).
SCIAMACHY spectra are shown to indicate that a) there is no (obvious) other spectral signal in this range which could affect the broad-band SABER observation; b) SCIAMACHY applies a background correction, but SABER does not, but comparison of the SCIAMACHY results with and without the background correction (left and right panels of Figure 3.6) shows that this is not the reason for the difference. SABER applies a correction for self-absorption which affects the results below 70 km altitude (M. Mlynczak, personal communication), and it is concluded that this is the most likely reason for the difference, highlighting that a similar correction could be applied to SCIAMACHY VERs in the future.
The vertical structure is captured very consistently by both instruments, showing the maximum in the lower mesosphere around 60 km, as well as a secondary maximum at around 87 km altitude. Also as seen by Figures 3.6c and 3.6d there is a $\leq$20% difference between the two instruments in the $\sim$75–100 km altitude range. Relatively big differences as of 50-100% are observed above $\sim$100 km which is the result of very weak airglow intensity and different signal-to-noise ratios between the two instruments, according to Figure 3.4f. There still exists $\leq$44% average difference between the instruments between $\sim$60 and $\sim$75 km altitude, which as will be discussed in Section 4.2 could be due to the increasing role of the molecular oxygen self absorption with decreasing altitude, or the background subtraction which I applied to the SCIAMACHY data.
This could be due to three reasons. 1) SCIAMACHY employs a background correction for backscattered solar and upwelling radiation; 2) as SABER uses a filter with a large bandwidth to observe the $O_2(^1\Delta)$ radiation, the detector bandwidth might include other emission signals which can not be detected or corrected for, and 3) SABER provides a correction for self-absorption below 80 km altitude (M. Mlynczak, personal communication). To test the first assumption, SCIAMACHY results in Figure 3.6 are shown with and without the background correction applied. Results are very similar, indicating that the background correction does not contribute significantly to the difference. To test the second assumption, selected spectra of the SCIAMACHY instrument are shown in Figures3.6e and 3.6f, indicating that no other emission signals are observed in this spectral region. To conclude, the most likely reason for the observed difference between SCIAMACHY and SABER $O_2(^1\Delta)$ VERs below 75 km is self absorption, and this is indeed consistent with estimates of the transmission along the line-of-sight using HITRAN line intensities.

3.3 Spatial-temporal variability of O_2 VERs

I calculate the daily mean volume emission rates as follows. I binned the measurements into 5° latitude bins from pole to pole (85°N to 85°S). In each bin, the measurements which

are located in the plus-minus 2.5° of each latitude are attributed to that latitude, and are averaged to obtain daily mean VER. An example of the latitude-altitude distribution of daytime $O_2(^1\Sigma)$ VER (on 03/02/2010) is shown in Figure 3.4c and of daytime $O_2(^1\Delta)$ VER in Figure 3.4d (VERs with low signal to noise ratio and large measurement errors are excluded). Daily mean $O_2(^1\Sigma)$ VERs have maximums in the range of 1–2 orders of magnitude smaller than $O_2(^1\Delta)$. Same as our results for a single orbit (section 3.1.2) we see the largest values for $O_2(^1\Delta)$ VER below 60 km and the largest values for the $O_2(^1\Sigma)$ VER around 90 km.
In order to investigate the signal to noise ratio of daytime VER, Figure 3.4e shows the signal to noise ratios of the daily mean $O_2(^1\Sigma)$ VERs. We see the strongest daytime $O_2(^1\Sigma)$ signal with a signal to noise ratio of >30 in the 70–130 km altitude range. The strongest twilight $O_2(^1\Sigma)$ signal is seen between 84 km and 95 km (not shown here). Figure 3.4f shows that the stronger $O_2(^1\Delta)$ signal is observed below 105 km, with the strongest signal of > 150, at 60 km to 80 km. The strongest twilight $O_2(^1\Delta)$ signal is observed in the altitude range of 83–97 km (not shown here).
In the following, I discuss the variations of the daily mean VERs versus latitude and time. For every day, daily averages are formed for specific latitude areas, which are 5° from pole to pole (85°N to 85°S), with 2.5° width, i.e., averaged over ±2.5°. Then, I assess the temporal variations in the mesosphere and lower thermosphere (70–140 km) in 30°N. Then, I discuss the peak values, altitude of the peak values, and variations of the centroid altitudes as a function of time and latitude.

3.3.1 Time series at 30°N

By calculating the daily mean VERs for all of the days in which there are SCIAMACHY MLT limb scans, I obtain the daily averaged time series for the daily mean VERs from 07/2008 to 03/2012. An example of these times series selected for 30°N for all altitudes combinations is shown in Figure 3.7a for daytime $O_2(^1\Sigma)$ VER and in Figure 3.7b for daytime $O_2(^1\Delta)$ VER. It is observed that a semi-annual variation with the strongest $O_2(^1\Sigma)$ in the range 90–95 km during May-June and September-November, and the weakest signals in December-March with a secondary minimum in August. The highest values of the $O_2(^1\Delta)$ VER are located at the lowest observational altitudes, which are mainly formed by ozone photodissociation (Thomas et al. (1984)), which will be discussed in more detail in Section3.3.3. I observe secondary maxima in $O_2(^1\Delta)$ which occur mainly in May-June and September-November (early summer and Autumn) in the altitude range of 75–95 km. The secondary maxima of $O_2(^1\Delta)$ occur at the same altitude range and with the same temporal variations as $O_2(^1\Sigma)$. These are discussed in more detain in the following section.

3.3.2 Peak values variation

Here, I investigate the daily mean VERs in the mesosphere and lower thermosphere with respect to altitude and time. For this, we extract the peak values of daily mean VERs for $O_2(^1\Sigma)$ and for $O_2(^1\Delta)$, in the 85–100 km altitude range, which are shown in Figures 3.8a and 3.8b respectively. In Figures 3.8b, 3.8d, and 3.8f only regions are shown in which the secondary maximums of $O_2(^1\Delta)$ exist. The altitudes of the peak values are also obtained. The peak values of the $O_2(^1\Sigma)$ VER in the middle to low latitudes (60°S - 60°N) seem to correlate with the maximum intensity of solar radiance, see Figure 3.8g. It is apparent that the overall behavior of the annual variations of the peak values of the $O_2(^1\Sigma)$ volume emission rates matches qualitatively well with the minimums of the solar zenith angles and thus maximums of the solar radiance. Additionally, it is observed that attenuations in the peak values in the late northern winters, mainly from late January until early March each year. This will be further investigated in Section 5.1 for the case of spring 2009.
Secondary maxima of the $O_2(^1\Delta)$ VERs are limited to high latitude winters. The correlation between the $O_2(^1\Sigma)$ VERs with the solar radiation suggests the formation due to sunlight, either with ozone photolysis (1.12) and (1.17), or abundance of atomic oxygen due to stronger O_2 photolysis. In the latter case, the formation of the excited states can be due to atomic oxygen recombination (1.11) and (1.16). High values in the high latitudes, where the solar flux is low, generally suggests other sources such as atomic oxygen recombination (Thomas et al. (1984)). This is true for $O_2(^1\Sigma)$, where the high values occur at high latitudes in winter and spring. These high values are supposed to be due to downward transport of atomic oxygen into the mesosphere-lower thermosphere. The sensitivity of the airglow to different parameters will be investigated in more detail in Section 3.3.3
Altitudes of the peak values of $O_2(^1\Sigma)$ and $O_2(^1\Delta)$ are shown in Figures 3.8c and 3.8d respectively. Altitudes of the peak values of $O_2(^1\Sigma)$ follow approximately the maximums of the solar radiance, as compared to Figure 3.8g, but show highest values in low to middle latitudes. The altitude range of the peak values is <94 km at low latitudes, <90 km at high latitudes. Enhanced maximum values in high northern hemisphere springs with higher peak altitudes <92 km are also observable.
Very low peak values of VERs, and very high values of altitudes of the VERs in the higher-most southern latitudes in the northern winters, correspond to the low signal to noise ratios and are lower than our level of significance.
In regions where the secondary maximums of $O_2(^1\Delta)$ exist, the altitude of the peak values occur in the altitude range of ∼84–89 km.
Estimation of the altitude of the peak values is affected by the instrument noise and vertical resolution. A more stable criterion is centroid altitude h_{CA}:

$$h_{CA} = \frac{\sum_i a_i v_i}{\sum_i v_i} \tag{3.10}$$

in which v_i is the volume emission rate at altitude a_i which ranges from ∼50 km to ∼150 km for $O_2(^1\Sigma)$ and from ∼85 km to ∼100 km for $O_2(^1\Delta)$. Figure 3.8e shows the centroid altitudes for daytime $O_2(^1\Sigma)$ and Figure 3.8f shows the centroid altitudes for daytime $O_2(^1\Delta)$.

The maximum h_{CA} for the $O_2(^1\Sigma)$ correlates with (maximum intensity) of solar radiance. The altitude range of the $O_2(^1\Delta)$ h_{CA} is between 85 km and 95 km (according to Figure 3.8f), as compared with altitudes of the peak values, show gentler variation which well resemble the minimum solar zenith angle variations depicted in Figure 3.8g. We also observe the high values of h_{CA} in the narrow band at northern polar latitudes, where the solar flux is low. Due to the large solar zenith angle, Reaction 1.25 is the most important contributor and this suggests atomic oxygen recombination as a source. Very low values of h_{CA}s, in the higher-most latitudes, mainly in hemispheric winters correspond to low signal to noise ratios of the corresponding VERs (not shown here) and are lower than our significance level.

Figures 3.8c, 3.8d, and 3.8f show a decrease in the peak $O_2(^1\Delta)$, altitude of the peak $O_2(^1\Delta)$, and $O_2(^1\Delta)$ h_{CA} respectively between November 2010 and February 2011. This is because of a change in the limb sequence so that the tangent heights are shifted in these days and are seen in the lower altitudes. The altitude registration of each observation during this period is recorded at ∼1 km lower value comparing to other times and according to Equation 3.10 this makes ∼1 km change in h_{CA}s. However, this has no noticeable effect on the VER time series in Figures 3.7a, 3.7b, 3.8a and 3.8b.

3.3.3 Discussion of the temporal spatial variations

Spatial-temporal variations in the peak values and altitude of the peak values suggest that the daytime $O_2(^1\Sigma)$ and $O_2(^1\Delta)$ VERs in the 80–100 km altitude range are formed by a combination of ozone photolysis and atomic oxygen recombination. This is already known according to the Khomich et al. (2008), and the schematic shown in Figure 1.7. In high latitudes during winter and spring, atomic oxygen recombination dominates, but in the sub-polar region, ozone and O_2 photolysis are more important.

In order to test whether these results are consistent with our understanding from photochemical production or loss of $O_2(^1\Delta)$ and $O_2(^1\Sigma)$, a simple photochemical model is set up which covers the production and loss processes summarized in Section 1.5.2 (Reactions 1.11 to 1.25). The ozone profile is adapted from the mean global multi-annual mean from Smith (1984). Temperature, total air density, molecular nitrogen and molecular oxygen are calculated from the MSIS model. Photolysis rates are adapted from the 3dctm model (Sinnhuber et al., 2018) and calculated for different solar zenith angles. Constants and temperature-dependent reaction rates are shown in Tables 3.1 and 3.2 respectively . The model calculates $O_2(^1\Sigma)$ and $O_2(^1\Delta)$ in photochemical equilibrium considering all formation

Notation	Value	Comment
k_{boltz}	1.38064852e-23	J/K
R_{2N_2}	0.791	
R_{2CO_2}	380.*1.e-6	
R_{2H_2O}	1.e-6	
J_{2g}	2.04e-9	Hitran-based estimate of O2(1Σ)
		production by resonance fluorescence (Rothman et al., 2005)
$q_{O^1S\_O}$	5.0e-12	quenching of O1S and O
$q_{O^1S\_O2}$	5.0e-12	quenching of O1S and O2
$q_{O^1S\_N2}$	2.32e-12	quenching of O1S and N2
$A_{O^1S\_O1D}$	1.26	green line, from NIST database (Ralchenko et al., 2008)
$A_{O^1S\_all} =$		
$A_{O1S\_O1D} + 0.0754$	1.228	total O1S radiative loss
k_{O_O1S}	6e-12	bildet O(1S)
k_{O_tot}	0.04*3.3e-9	+6e-12
$k_{O_2\_sig}$	0.04*6.6e-12	quenching of O2* with
		O2, all branches
A_c	0.66	(Stegman and Murtagh, 1991)
		loss of O2*, following Lednyts'kyy et al. (2015)
		relative to channel leading to O1S
C_0	13.	radiative loss of O2*
C_1	224.	quenching by O
C_2	17.	quenching by O2
		rates for O2(1Sigma) loss
A_Σ	0.0758	A_k
		value from Mlynczak and Nesbitt (1995)
$q_{O2(^1\Sigma)\_O3p}$	8.e-14	
$q_{O2(^1\Sigma)\_CO2}$	4.2e-13	
$q_{O2(^1\Sigma)\_O2}$	3.9e-17	rates for $O_2(^1\Delta)$
A_Δ	1.47e-4	
$q_{O2(^1\Delta)\_O3P}$	2.e-16	
$q_{O^1D\_O^1S}$	1.0	branching of O1D
		quenching to $O_2(^1\Sigma)$

Table 3.1: Constants used in the photochemical model

Notation	Value	Comment
k_1	2.76e-34 $\cdot$ ρ exp(720/T)[a]	$O + O + M \rightarrow O_2 + M$
k_2	6.e-34 $\cdot$ $\rho \cdot (T/300)^{-2.4}$	$O + O_2 + M \rightarrow O_3 + M$
$q_{O(^1D)\rightarrow O_2}$	$3.3e-11 \cdot \exp(55./T)$	quenching of O(1 D) with O_2
$q_{O(^1D)\rightarrow N_2}$	$2.15e-11 \cdot \exp(110/T)$	quenching of O(^{1}D) with N_2
$q_{O_2(^1\Sigma)\_N_2}$	$1.8e-15 \cdot \exp(45/T)$	quenching of $O_2(^1\Sigma)$ with N_2
$q_{O_2(^1\Sigma)\_O2}$	3.6e-18$\cdot$exp(-220/T)	quenching of $O_2(^1\Sigma)$ with O_2

[a]T: Temperature; ρ: density

Table 3.2: Temperature dependent rates used in the photochemical model

pathways; to estimate the contributions of the different formation pathways, equilibrium estimates are also provided considering the individiual pathways, e.g., by quenching from O(^{1}D) only from ozone photolysis, by quenching from O(^{1}D) only from the so called Barth process, by resonance fluorescence, and by ozone photolysis and $O_2(^1\Sigma)$ quenching.
A detailed description of the model can be found in Zarboo et al. (2018), and Figure 3.9 is adapted from their work, showing the contributions of the different production pathways of the O_2 dayglow for one specific situation. It is inferred from Figure 3.9 that below about 82 km, $O_2(^1\Sigma)$ is formed in almost equal portions by quenching of O(^{1}D) and resonance excitation of $O_2(X^3\Sigma_g^-)$ for $O_2(^1\Sigma)$, while above that level, the quenching of O(^{1}D) is dominant. The $O + O$ reaction has about an order of magnitude less contribution in producing $O_2(^1\Sigma)$ compared to the other two branches even in the region where it has the greatest contribution (about 90 km). This is consistent with the ratios between twilight and daytime emission intensities of about ten, as discussed in section 3.1.1, regarding that during night and twilight $O_2(^1\Sigma)$ is formed only by $O + O$ reaction. Formation of $O_2(^1\Delta)$ is dominated by ozone photolysis at all altitudes, although below 90 km, quenching of $O_2(^1\Sigma)$ contributes about 10–25%.
To further investigate the sensitivity of the O_2 airglow to the different contributors, sensitivity studies have been carried out with the photochemical model varying the input parameters ozone, O_2 and O density by +-20%, and the solar zenith angle between zero and 88°. Results are presented in Figure 3.10 for $O_2(^1\Delta)$ and Figure 3.11 for $O_2(^1\Sigma)$.
Difference in ozone by ±20%, leads to a 15% to -21% difference in $O_2(^1\Delta)$ airglow at 85 km. This effect decreases up to 102.5 km falling to +2% to -3%. Then its magnitude increases as of 5.5% to -7% difference at 105 km and approaches zero at 106 km and altitudes upwards. Figure 3.10b shows that ±20% change in molecular oxygen leads to ∓10% change in $O_2(^1\Delta)$ airglow at 70 km and approaches zero up to 80 km altitude. Then this effect changes its sign and increases monotonically such that it reaches +30% to -50% change at 110 km. Figure 3.10c shows that ±20% change in atomic oxygen results in the decrease/increase of 6% change in $O_2(^1\Delta)$ airglow at 95–102 km. This effect approaches zero at 105 km altitude

and changes its sign such that at 106 km reaches -4% to +3% change in $O_2(^1\Delta)$ and higher up it decreases fast and approaches zero. Figure 3.10d shows that increasing solar zenith angle from 0 to 88° results in 30% increase to 5% decrease in the $O_2(^1\Delta)$ at 82 km. It decreases as much as -3% to +1% at 90 km altitude, and higher up it increasingly grows. In summary, the $O_2(^1\Delta)$ dayglow is dominated by ozone photolysis below 95 km. Above 100 km, the solar zenith angle dependence is by far the largest, with smaller contributions of O_2 quenching. Atomic oxygen affects the $O_2(^1\Delta)$ dayglow in the altitude region 90–105 km, but its contribution is small compared to the other parameters tested even there.

Figure 3.11a shows that increasing or decreasing O_3 as much as 20%, leads to 10% to -15% change in the $O_2(^1\Sigma)$ airglow. This becomes very small at 97.5 km altitude and at 102 km it ranges in the ±5, and approaches zero at 107 km. Figure 3.11b shows that changing O_2 as much as ±20%, leads to ±20% change in $O_2(^1\Sigma)$ airglow up to 90 km, and to 30% to -60% change of airglow at 102.5 km, and remains constant further up. Figure 3.11c shows that the effect of increasing or decreasing atomic oxygen in the $O_2(^1\Sigma)$ remains near zero, and then at 102.5 km reaches ±7.5% and then up to 107.5% and further up it approaches zero. Figure 3.11d shows that increasing solar zenith angle from 0 to 88° leads to 7.5% to -10% change in the $O_2(^1\Sigma)$ airglow at 82 km, and strictly increases higher than 90 km.

To summarize, the O2(1Sigma) dayglow is dominated in comparable amounts by ozone photolysis (presumably via O(1D) quenching) and O2 (quenching) below 95 km. Above 95 km, the strongest variability comes from the solar zenith angle, with higher solar zenith angles leading to lower signals. Atomic oxygen contributes in the altitude region 95-105 km presumably due to the O+O self reaction, but as for O2(1Delta), its contribution is small compared to the other parameters.

In the altitude of the $O_2(^1\Sigma)$ maximum (85–95 km) and the $O_2(^1\Delta)$ second maximum (85–90 km), the O_2 dayglow is dominated by ozone photolysis, with smaller contributions coming from O_2 quenching and the $O + O$ self-reaction. The solar zenith angle dependence is still rather small in this altitude region. It is concluded that it is possible that the strong maxima observed in this altitude region during high-latitude winter and spring are due to enhanced atomic oxygen from the thermosphere; but in this case, atomic oxygen would have to increase by at least an order of magnitude. More likely is that these maxima are derived indirectly, due to an increase in ozone in the second maximum following the atomic oxygen increase, and due to decreased values of O_2 in thermospheric air which leads to an increased lifetime of the O_2 dayglow.

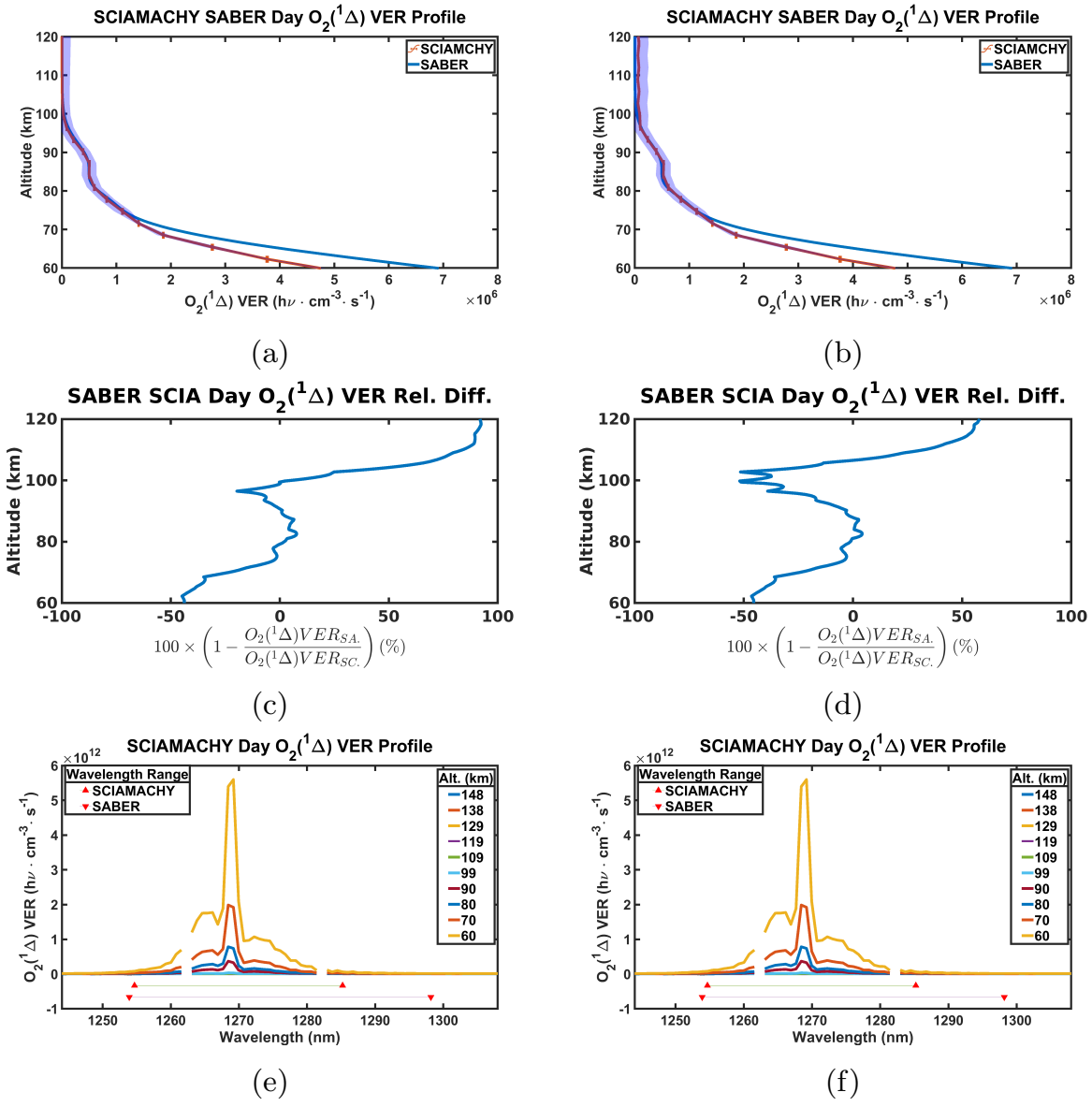

Figure 3.6: SCIAMACHY vs. SABER daytime $O_2(^1\Delta)$ VER as averaged profiles on the measurement days with common solar local time, i.e., 10 a.m. for SCIAMACHY (with 1σ errorbars) and 9:30–11:00 a.m. for SABER (a) and (b), and the relative difference between the two instruments, with the shaded blue representing the 1σ (c) and (d). (e) and (f) show SCIAMACHY $O_2(^1\Delta)$ spectra at some selected altitudes. left panel represents the spectra and right panel represents the spectra from which the background is subtracted. Horizontal bars denotes the wavelength range over which SCIAMAHCY and SABER get their integrated spectra for $O_2(^1\Delta)$ band.

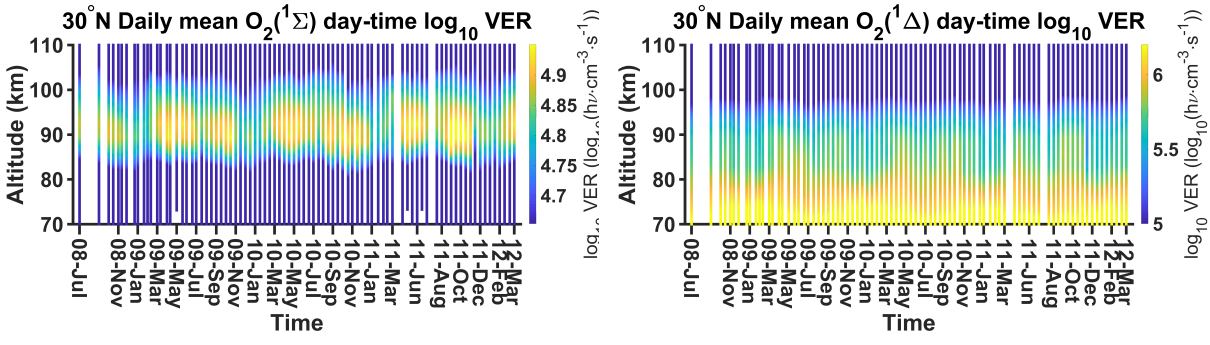

(a) (b)

Figure 3.7: Time series of the daily mean VER. (a) for daytime $O_2(^1\Sigma)$ VER, 30°N, 07/2008 to 03/2012. (b) as (a) for daytime $O_2(^1\Delta)$ band (adapted from the published material Zarboo et al. (2018)).

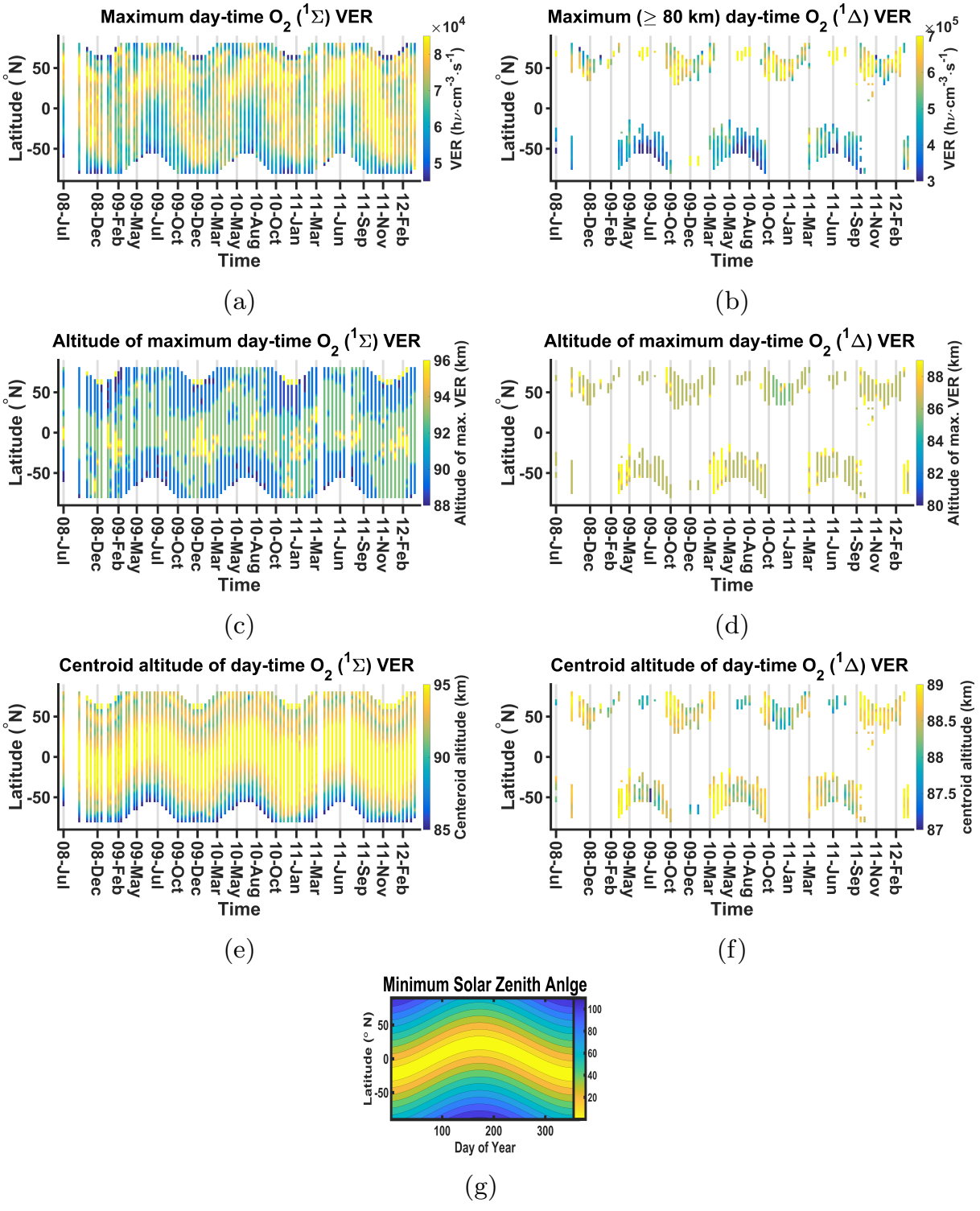

Figure 3.8: (a) Time series of the maximal daily mean $O_2(^1\Sigma)$ VER. (b) as (a) for $O_2(^1\Delta)$ band. (c) Time series of the altitudes of the maximum daily mean $O_2(^1\Sigma)$ VER. (d) as (c) for $O_2(^1\Delta)$ band. (e) Time series of the centroid altitudes of the daytime $O_2(^1\Sigma)$ daily mean VER (km). (f) as (e) for $O_2(^1\Delta)$ band. (g) Typical of the minimum solar zenith angle (degrees). (Panels (a) to (f) are adapted from the published material Zarboo et al. (2018)).

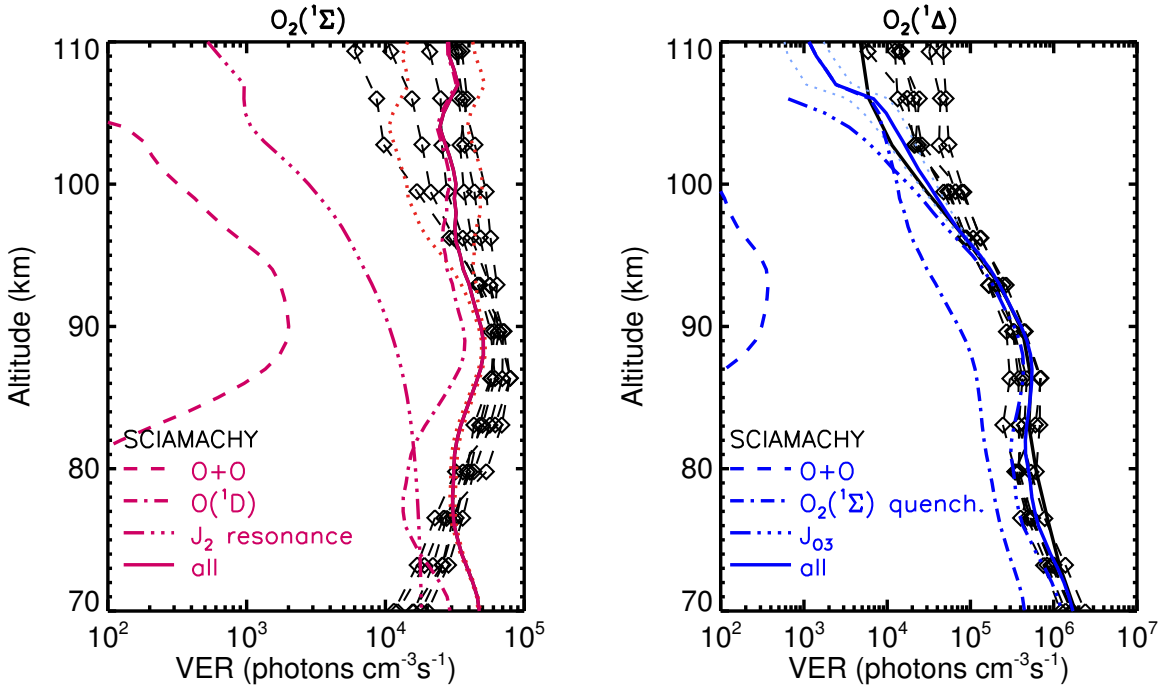

Figure 3.9: Modeled VERs of $O_2(^1\Sigma)$ (left) and $O_2(^1\Delta)$ (right). Solid lines are the mean of all model results for solar zenith angles 0, 10, 20, 30, 40, 50, 60, 70, 80, 88° considering all formation processes; dotted lines show the variability due to photolysis reactions (± standard deviation). The dashed, dash-dotted, and dash-dot-dot lines show the contributions of individual formation processes: $O + O$, $O(^1D)$ quenching and resonant excitation for $O_2(^1\Sigma)$, $O + O$, $O_2(^1\Sigma)$ and ozone photolysis for $O_2(^1\Delta)$. Black lines with symbols are SCIAMACHY profiles at five latitudes observed on February 3, 2010 (see Figure 3.3)(The figure is adapted from the published material Zarboo et al. (2018)).

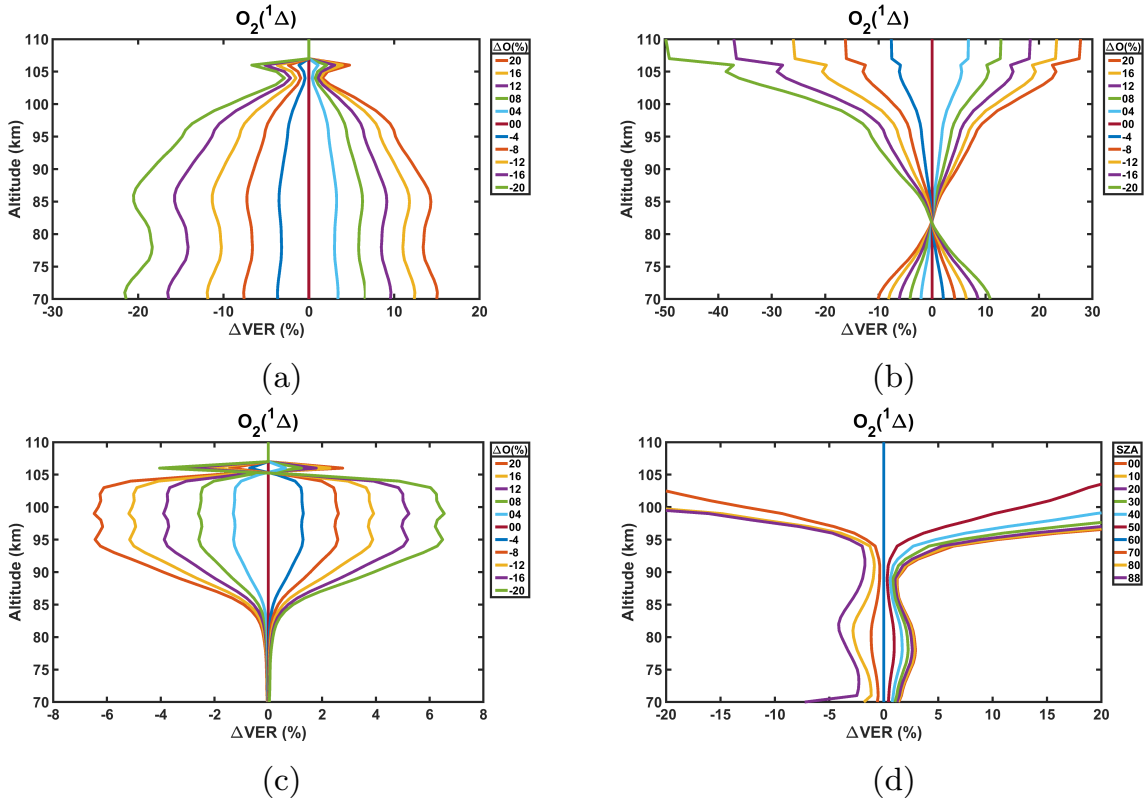

Figure 3.10: Sensitivity tests after changing (a) ozone, (b) molecular oxygen, (c) atomic oxygen number densities between -20–20%, and (d) solar zenith angle between 0–88° in the production of $O_2(^1\Delta)$ VERs in the 70–110 km altitude range.

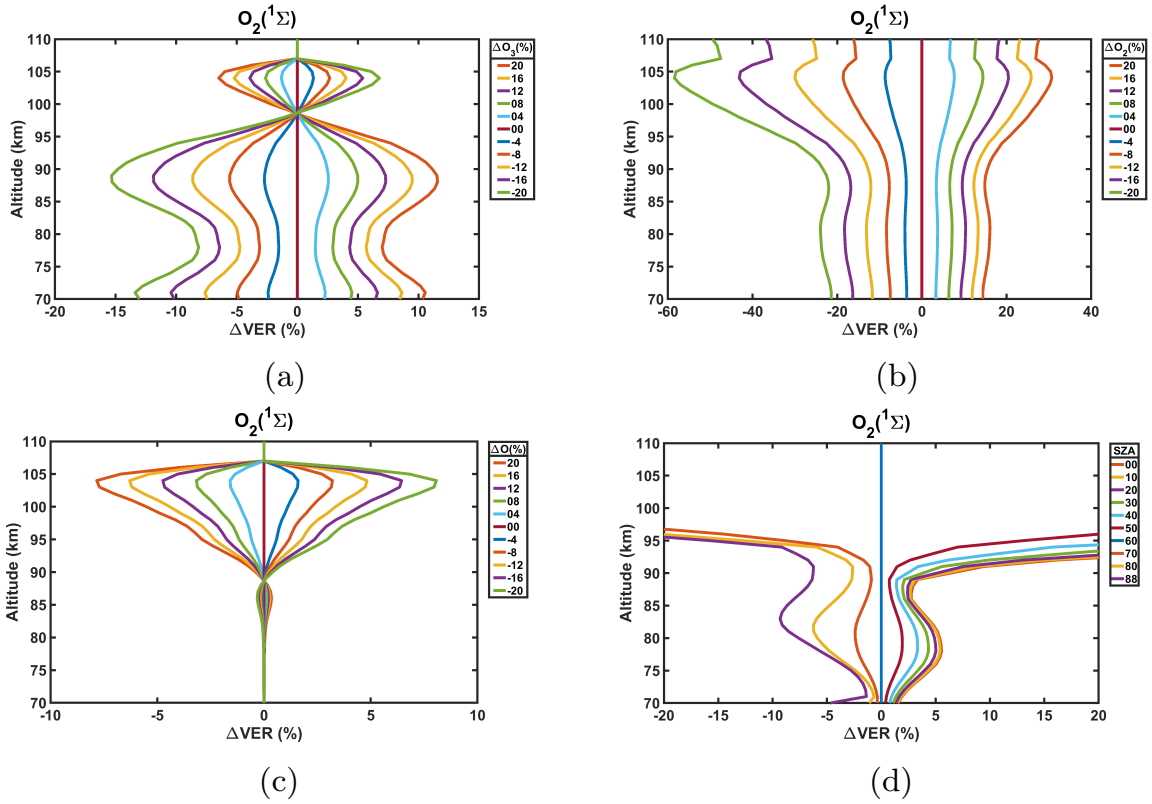

Figure 3.11: Same as Figure 3.10 except for the production of $O_2(^1\Sigma)$ VERs.

4 Temperature Retrieval

In the following, the derivation of the temperature from fitting the modelled spectra to the measured emission intensities are discussed in Section 4.1. Also, comparison of the resulting temperature profiles to other instruments such as SABER, MIPAS, and OSIRIS is presented in Section 4.4, and the temporal-spatial variations of temperature in the MLT and climatologies of temperatures are discussed in Sections 4.5 and 4.6 respectively.

4.1 Description of the temperature retrieval

The intensity of a spectral line depends on the transition probability and the frequency ν, as well as on the number of molecules in the initial state (Herzberg, 1950). Thus for a theoretical prediction of intensities, a knowledge of the numbers of molecules in the various initial states is necessary, in addition to a knowledge of the transition probabilities. Since the lifetime of $O_2(^1\Sigma)$ species are almost 12 seconds (Brasseur and Solomon, 2006), the rotational states could be considered in *thermal equilibrium*. Under thermal equilibrium conditions, the distribution of the rotational lines is well known theoretically. The temperature dependence of the intensities of the rotational lines of the $O_2(^1\Sigma)$ emission makes it possible to derive the temperature by fitting the observed emission spectra to modelled emission spectra. The observed O_2 bands are rotational-vibrational bands. In the observation of this rotational-vibrational lines, the rotational lines are in thermal equilibrium independent of the vibrational lines, so the rotational lines are important in the temperature retrieval.
The emission intensities and center wavelengths of 144 spectral lines within the $O_2(^1\Sigma)$ (759–767) nm are calculated for emission temperatures between 60–1000 K at 1 K intervals, using the $O_2(^1\Sigma)$ upper and lower state vibrational and rotational constants determined by Babcock and Herzberg (1948) and updated with values from the 2004 HITRAN spectroscopic database (Rothman et al., 2005, for more details see Appendix 7). For each temperature, the modelled emission line spectrum is convolved with the SCIAMACHY slit function and binned into wavelength intervals that correspond to the SCIAMACHY CCD pixelated spectrum in the $O_2(^1\Sigma)$ region. The modelled spectra are each normalized such that the sum of intensities over the spectrum is equal to 1 photons/s/cm^3. As the emission temperature increases the higher rotational levels become more populated, and as shown in Figure 4.1,

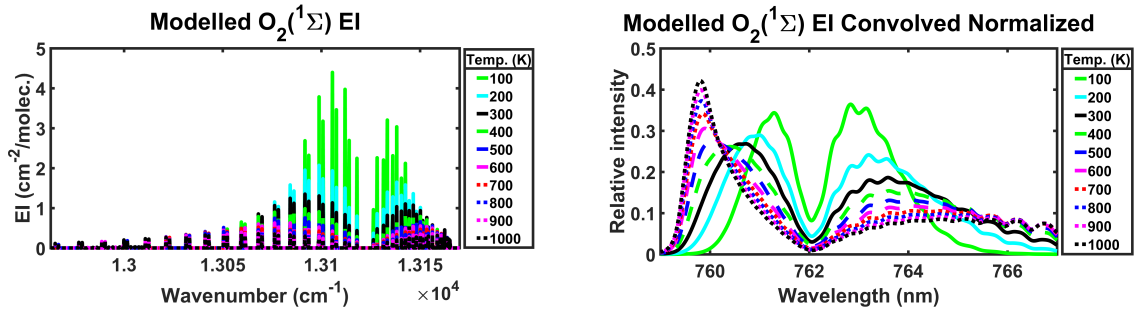

(a) (b)

Figure 4.1: Modelled $O_2(^1\Sigma)$ emission intensities in the wavenumber domain as provided by the relations mentioned in Section 4.1 and (b) theoretical curves as convolved with SCIAMACHY slit function and normalized to 1 in the wavelength domain at different temperatures .

the overall effect on the normalized spectrum is to decrease the relative line intensities near the center of the band and to increase those in the wings of the band.
At each height, z, the inverted spectrum, I(z), is compared to the modelled emission spectra E(T). As noted above, both the inverted and modelled spectra have been normalized such that the sum of intensities over the spectrum is equal to 1 photons/s/cm^3. The sum of the square difference between the inverted and modelled $O_2(^1\Sigma)$ spectra is calculated according to 4.1.

$$S(z,T) = \sum_{p}^{N} [I_p(z) - E_p(T)]^2 \tag{4.1}$$

where p is the pixel index and N is the number of pixels in the $O_2(^1\Sigma)$ spectra. The retrieved temperature at height z_i is taken as the temperature that minimizes S(z_i,T).
As the radiative lifetime for the $O_2(^1\Sigma)$ is 12 s, the $O_2(^1\Sigma)$ relative population distribution of rotational states is in local thermodynamic equilibrium, so that the retrieved rotational temperature is the local atmospheric temperature. I got the emission intensities from SCIAMACHY, by the method which is described in Section 3.1.1. Different theoretical curves for different temperatures between 100–1000 K are shown in Figure 4.1. demonstrating the impact of temperature and the SCIAMACHY wavelength resolution on the observed $O_2(^1\Sigma)$ signal. In figures 4.2a and 4.2b examples of the fitted spectra and modelled spectra are shown, for 90 km and 100 km respectively. The retrieved temperatures are 182 K and 170 K respectively. As for Figure 4.1, the broader the shape of the spectra, yields higher temperature in the retrieval.

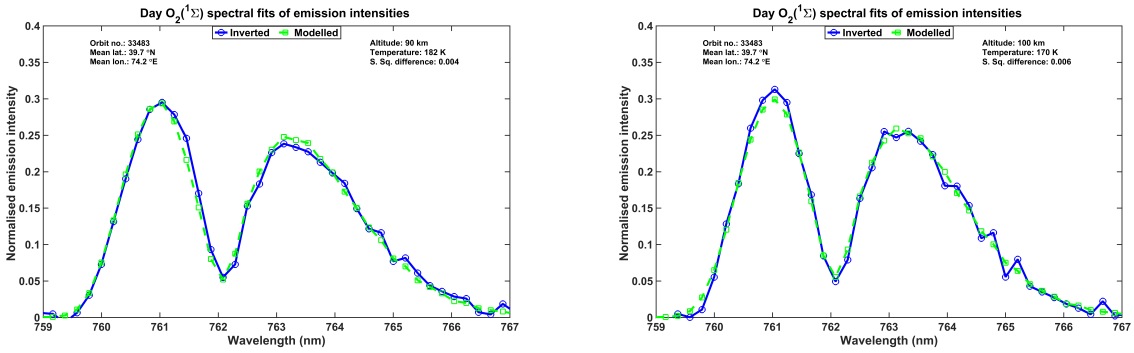

(a) (b)

Figure 4.2: An example of the spectral fits of the inverted emission intensity (blue curve with circles) with modelled emission intensity (green curve with squares). (a) for 90 km altitude, date: 2008/07/26, orbit number: 33483, latitude 39.7° N, longitude 74.2° E. (b) as (a) for 100 km altitude.

4.2 Sensitivity study of the temperature retrieval

In the following I will investigate the sensitivity of the retrieved temperatures by varying input parameters of the retrieval such as a wavelength shift, peak exclusion, and wing exclusion. O_2 self absorption plays a role below ∼90 km altitude and must be considered (Sheese et al., 2010), but studying this effect could be the subject of future work.

4.2.1 Spectral shift

In this section, a sensitivity test regarding the effect of the wavelength displacement of the simulated spectra and fitting it on the measured spectra is conducted and the effect of this displacement on the retrieved temperatures is investigated. The rationale behind this sensitivity test is to minimize a probable error in the wavelength registration of the SCIAMACHY instrument. The case study for one example date 03/02/2010 at 90 km altitude with 0.1 nm wavelength displacement towards longer wavelengths results in 4 K decrease of the retrieved temperature compared to the displacement retrieval without wavelength shift. For a wavelength displacement as much as 0.1 nm towards the longer wavelengths resulted in the considerable decrease of the residuals (sum of the squared differences between the simulated and measured spectra) as much as 49% as shown in Figure 4.3a and 4.3b for the unchanged and displaced retrievals, respectively. This indicates a systematic problem of the wavelength registration of SCIAMACHY in this channel. To address this problem, in the following, a spectral shift is fitted simultaneously with the temperature. Carrying out many wavelength displacement sensitivity tests it is found that

wavelength displacements over the [-0.1,0.1] nm wavelength interval with 0.025 nm increment steps can result in the considerable improvement of the accuracy of the temperature retrieval.

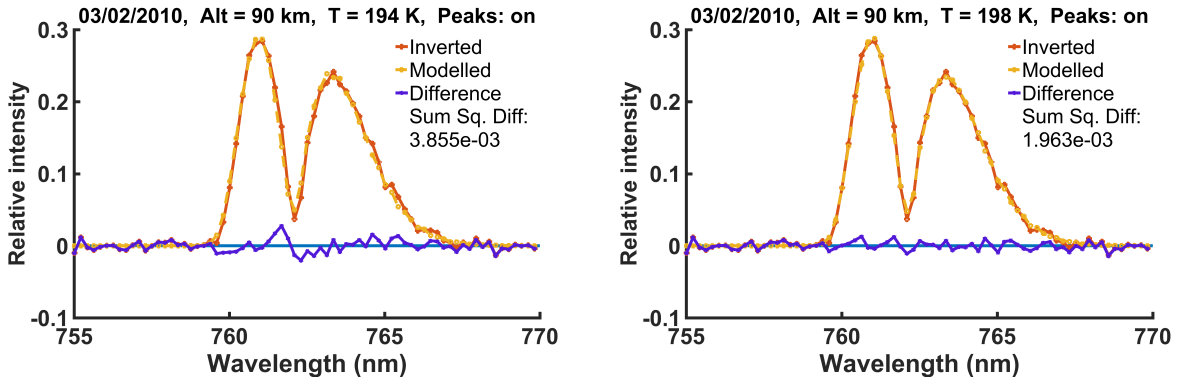

(a) (b)

Figure 4.3: Examples of the spectral fits used to retrieve the temperature from measured SCIAMACHY emission intensities fitted with simulated spectra without wavelength displacement (a), and the modelled spectra shifted by 0.05 nm towards longer wavelengths (b).

4.2.2 Peak exclusion

In this section, the retrieval of the temperature by fitting the simulated $O_2(^1\Sigma)$ spectrum to the SCIAMACHY measured spectrum over the two different spectral intervals is presented.. This test was undertaken at two different altitudes of 83 km and 90 km in order to investigate the effect of the spectral deformation of the measured spectra in the direction of the optical path due to the self-absorption in different regions of the $O_2(^1\Sigma)$ spectrum and finding the best fit. The spectral regions in the case of "peak exclusion" are [755,760.4] nm, [761.7,762.7] nm, and [764.2,770] nm. The spectral regions for the "peak inclusion" is [755,770] nm. Comparing results at two altitudes for the two cases, i.e., "peak inclusion" and "peak exclusion" cases, a 6 K temperature decrease at 83 km, and an 1 K decrease at 90 km is observed with respect to the "peak inclusion" case, as shown in Figures 4.4 and 4.5. This result implies that below 90 km the effect of self absorption on the deformation of the $O_2(^1\Sigma)$ especially over the [761.7,760.4] nm and [764.2,762.7] nm is more important. It is concluded that with "peak exclusion" it is possible to retrieve more accurate temperatures below 90 km by decreasing the effect of self absorption on the deformation of the $O_2(^1\Sigma)$ spectrum. Temperatures retrieved from $O_2(^1\Sigma)$ observations by the OSIRIS instrument have also been shown to be affected by self-absorption below 90 km altitude (Sheese et al., 2010), which leads to a shift towards colder temperatures (Patrick Sheese, personal communication). Self-absorption could be corrected in the altitude range 80–90 km, though not below as the

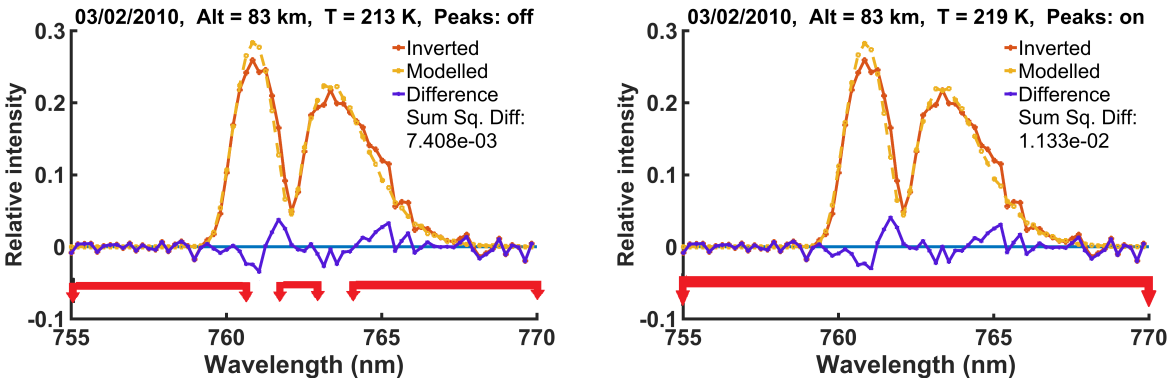

Figure 4.4: Instances of the temperature retrieval by fitting the simulated $O_2(^1\Sigma)$ to the SCIAMACHY measured spectra, on 03/02/2010, 83 km. (a) Fitting only [755,760.4] nm, [761.7,762.7] nm, and [764.2,770] nm wavelength intervals for the fit. (b) Fitting the [755,770] nm wavelength interval. Red lines indicate the wavelength range which is included in the fit.

$O_2(^1\Sigma)$ signal is optically dense there. Therefore we did not correct for it here, but this could be addressed in the future.

4.2.3 Wing exclusion

In order to investigate the effect of the self absorption on the $O_2(^1\Sigma)$ spectral deformation through the optical depth on the [755, 760.4] nm, [761.7, 762.7] nm, and [764.2, 770] nm (I called these intervals *wings* of the spectra) at different altitudes, a sensitivity test is undertaken as follows. Two spectral fits at 83 km and 90 km altitudes over [762.7,764.2] nm and [760.4,761.7] nm are undertaken and are compared to the spectral fits including the full [755,770] nm. It is observed that at 90 km the retrieved temperature is the same, but at 83 km the retrieved temperature is 19 K higher, as shown in Figures 4.6 and 4.7. This indicates that considering the "wings" of the $O_2(^1\Sigma)$ spectrum in temperature retrieval at lower altitudes is more important than considering the "peaks" of the spectrum. Depending on which part of the $O_2(^1\Sigma)$ spectrum is more affected by deformation, it is suggested to exclude peaks of the spectrum to retrieve the temperature.

4.3 Error estimation of temperature

In this section, two different methods for estimation of the uncertainty in the temperature retrieval are presented.
For this purpose, I conducted the spectral fits by adding/subtracting one standard deviation of the spectra (Subsection 3.1.1) from measured emission intensities, and setting the retrieved

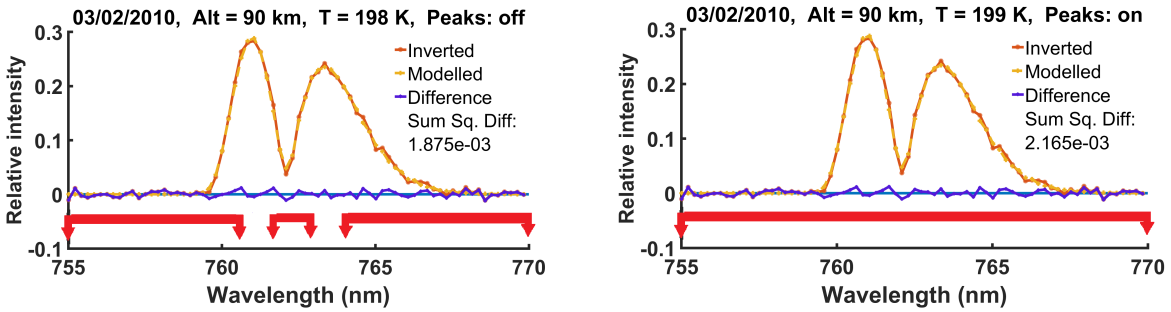

Figure 4.5: Examples of the effect of not considering (a) and considering (b) the "Peaks" regions of the spectrum on the retrieved temperatures. Red lines indicate the wavelength range which is included in the fit. For the definition of the peaks of the spectrum, see text.

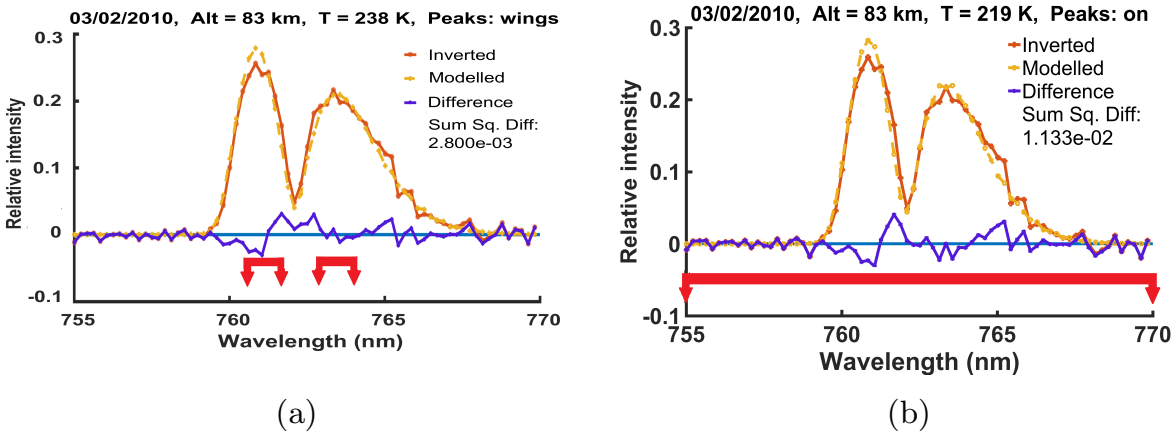

Figure 4.6: Temperature retrieval by fitting the simulated $O_2(^1\Sigma)$ spectra to SCIAMACHY measured spectra on 03/02/2010, 83 km. (a) taking [762.7,764.2] nm and [760.4,761.7] nm as the wavelength region to calculate the best fit. (b) taking [755,770] nm wavelength region to fit. Red arrows denote the "wings" spectral region. Red lines indicate the wavelength range which is included in the fit.

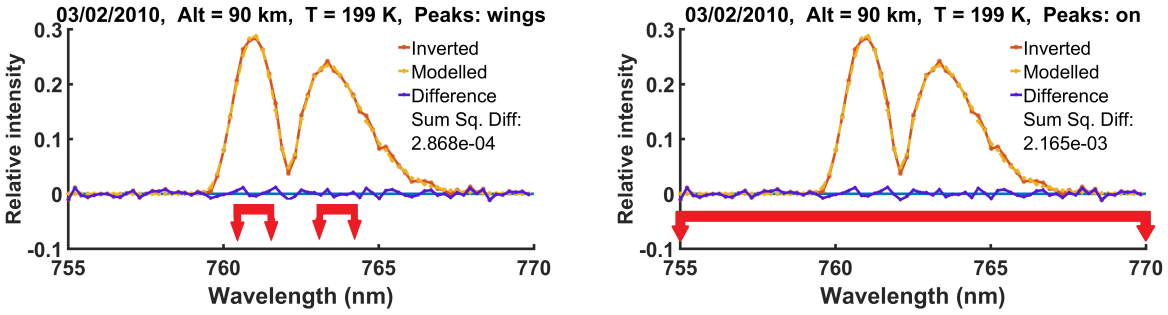

Figure 4.7: Temperature retrieval by fitting the simulated $O_2(^1\Sigma)$ spetra to SCIAMACHY measured spectra on 03/02/2010, 90 km. (a) taking [762.7,764.2] nm and [760.4,761.7] nm as the wavelength region to calculate the best fit. (b) taking [755,770] nm wavelength region to fit. Red lines indicate the wavelength range which is included in the fit.

temperatures as plus/minus one standard deviation to the original retrieved temperatures (lower panel of the Figure 4.8). For the upper panel I have used a method similar to the method Sheese et al. (2010) used, i.e., I simulated the retrieved temperatures which construct similar residuals to the residual of the original retrieved temperature.
This method works well around 90 km altitude, but leads to very large values above 105 km and below 80 km (Sheese et al. (2010)'s method worked worse, as shown in the upper panel). The left panel of Figure 4.8 correspond to the uncertainty in the retrieval of the unchanged wavelength spectral fits, and the right panel represents the uncertainty in the retrieval of temperature with 0.05 nm wavelength shift, as described in Subsection 4.2.1.
The Southern Atlantic Anomaly (SAA), as discussed in Section 3.1.2 affects $O_2(^1\Sigma)$ VERs, although the values are still significant. In our study, the regions with high values of noise, are filtered out from our retrieval, so SAA affected spectra are not included in the retrievals.

4.4 Validation of retrieved temperatures

I have compared the retrieved temperatures to other instruments including SABER on the TIMED satellite, MIPAS on the ENVISAT satellite, and OSIRIS on the ODIN satellite (see also Section 2.2). Daily averages of the retrieved temperatures are provided binned into 15° latitude bins for all SCIAMACHY measurement days. For comparing the SCIAMACHY retrieved temperatures to other instruments, observations taken on the same day with solar zenith angles smaller than 88° (considered as day-time) are averaged over the whole measurement period. This provides an average over up to 26 days.

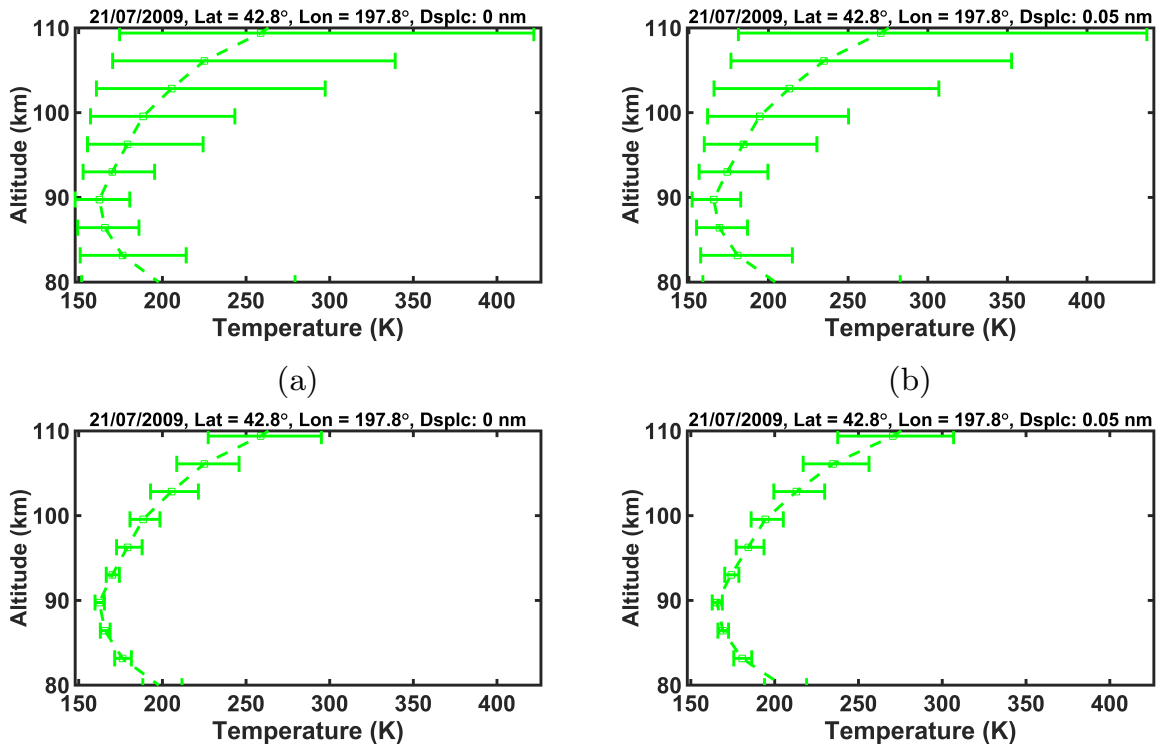

Figure 4.8: Retrieved temperature profiles on 21/07/2009, at 42.8°N, 197.8°E with different error estimation methods. (a) Simulation of the temperature retrieval errors with modelled spectra and without any displacement in the wavelength interval. (b) Same method as (a) with 0.05 nm displacement in the wavelength interval. (c) Simulation of the temperature retrieval errors with measured spectra and without any displacement in the wavelength interval. (d) Same method as (c) with 0.05 nm displacement in the wavelength interval.

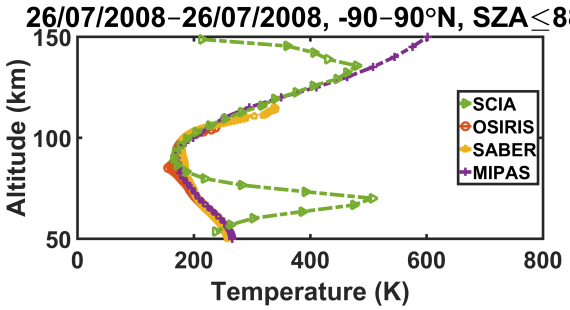

Figure 4.9: Vertical profile of the SCIAMACHY in comparison with OSIRIS, MIPAS, and SABER.

In Figure 4.11, mean profiles and the difference of other instruments to the SCIAMACHY retrieved temperatures are shown, for instance at latitudes 45–60°, 30–45°, and 15–30° North and South. The full comparison of all latitude areas is shown in the Appendix in Figures 7.7 to 7.8.

The comparison of the profiles shows that SCIAMACHY has the best agreement with MIPAS as shown in Figures 4.10 and 4.11. Below ∼110 km MIPAS has warmer temperatures, but above ∼110 km in the southern hemisphere MIPAS temperatures are colder than SCIAMACHY. Going further up, the MIPAS-SCIAMACHY differences strongly increase. OSIRIS has a larger difference to SCIAMACHY, except at southern tropical latitudes, where the difference is smaller. SABER show differences of ≤10 K below ∼105 km at ±45°N. Similar patterns of the differences are shown in Figures 7.7 to 7.9 for different latitude bins.

According to Figure 4.9, the discrepancy between the retrieved temperatures of the SCIAMACHY and other instruments again starts to increase above ∼120 km altitude, which is because of the very weak signal as can be seen as very low signal to noise ratios in Figure 3.4. This difference is the reason that the comparisons are limited to ∼95–120 km altitude range. MIPAS agrees best overall despite the different measurement technique, possibly due to the same orbit as SCIAMACHY (nearly the same local time). OSIRIS seems to disagree with all others, and the reason for this is not clear, as OSIRIS derives the temperatures in the same way as SCIAMACHY, a better agreement would be expected. Possibly the very different orbit, means larger natural variability. However, SABER, which also has a different orbit, is in better agreement with SCIAMACHY. Similar results are provided by other latitude bins, which are shown in the Appendix, in Section 7.3. Figure 4.9 shows that the SCIAMACHY retrieved temperatures are warmer compared to the other instruments below ∼90 km altitude. This is likely due to self-absorption as discussed in Section 4.2. Therefore, results are restricted to altitudes above 90 km in the following.

Figure 4.10 shows temperature profiles retrieved from SCIAMACHY (green), MIPAS (blue), SABER (yellow), and OSIRIS (red) at 90–120 km altitude range. In the left panel, Southern hemisphere temperature profiles, and in the right panel, Northern hemisphere temperature

profiles at 15° latitude bins are shown. The differences in the Southern hemisphere are smaller than the Northern hemisphere. Despite the different techniques used to retrieve the temperatures in the two instruments, SCIAMACHY and MIPAS have more agreement in the 90–120 km altitude range. The temperatures provided by the OSIRIS instrument at lower than 100 km is colder, but above 100 km is warmer than SCIAMACHY, and although it uses similar technique, have more difference with SCIAMACHY. SABER instrument is more similar to MIPAS, but above 110 km it gives large differences. Figure 4.11 shows that SCIAMACHY is in reasonable agreement with most of the other instruments - except with OSIRIS - at ∼90 km altitude. Going further up, SABER and OSIRIS have increasingly higher temperatures than SCIAMACHY, but MIPAS temperatures are between +11.6 K and -16.4 K compared to SCIAMACHY at 102 km and 115 km respectively.
In the 90–110 km altitude range, SCIAMACHY is mostly warmer than MIPAS. However, above 110 km altitude, there seems to be a latitude-dependent difference, with warmer temperatures in the Northern hemispheres, colder in the Southern hemispheres. The reason is not quite clear, but might be related to the (small) difference in local time, and (large) tidal signals there. For example, OSIRIS instrument on ODIN satellite have 6:00 pm local time, and SABER on TIMED, have variable local time because of its orbital precession (James M. Russell, 1999). Even MIPAS on the same satellite, sees the same airmass about 50 minutes later than SCIAMACHY (Bender et al., 2013). Because of the presence of tidal variability in the MLT temperature field (Liu et al., 2010), different sampling of each instrument introduces variability to the observed temperature field.

4.5 Temperature Time Series

Figures 4.12a to 4.12f show the time series of retrieved temperatures at different latitude bins. Annual variation at high latitudes is easily seen. Annual variability at high latitudes in the whole altitude range is observed, but changing sign around 100 km - in the mesopause region, summer is coldest, in the thermosphere, summer is much warmer than winter. this is seen quite clearly in Figure 4.12. In midlatitudes (30-45°), annual variation has nearly disappeared, instead there seems to be a trend to higher temperatures in the thermosphere - going from solar minimum to solar maximum. In 100-110 km, there still seems to be an annual variation with higher temperature in summer. In the mesosphere below 100 km there is still the reversed annual variation with lower temperature in summer. More latitudes are found in the Appendix (Section 7.4).

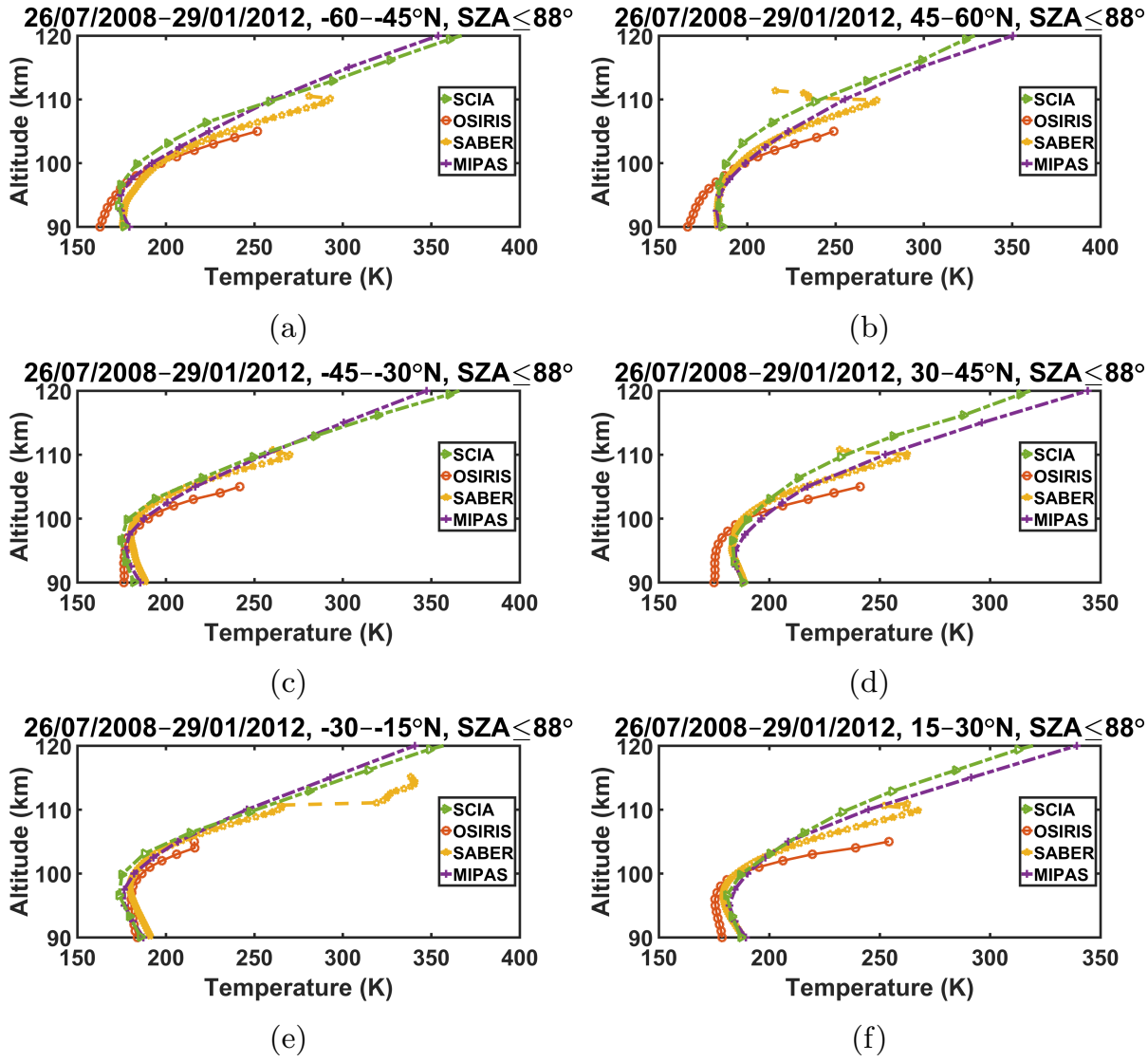

Figure 4.10: Retrieved temperatures profiles from instruments including the SCIA (green), the MIPAS instrument (blue), the SABER instrument (yellow), and the OSIRIS instrument (red) at 15° latitude bins.

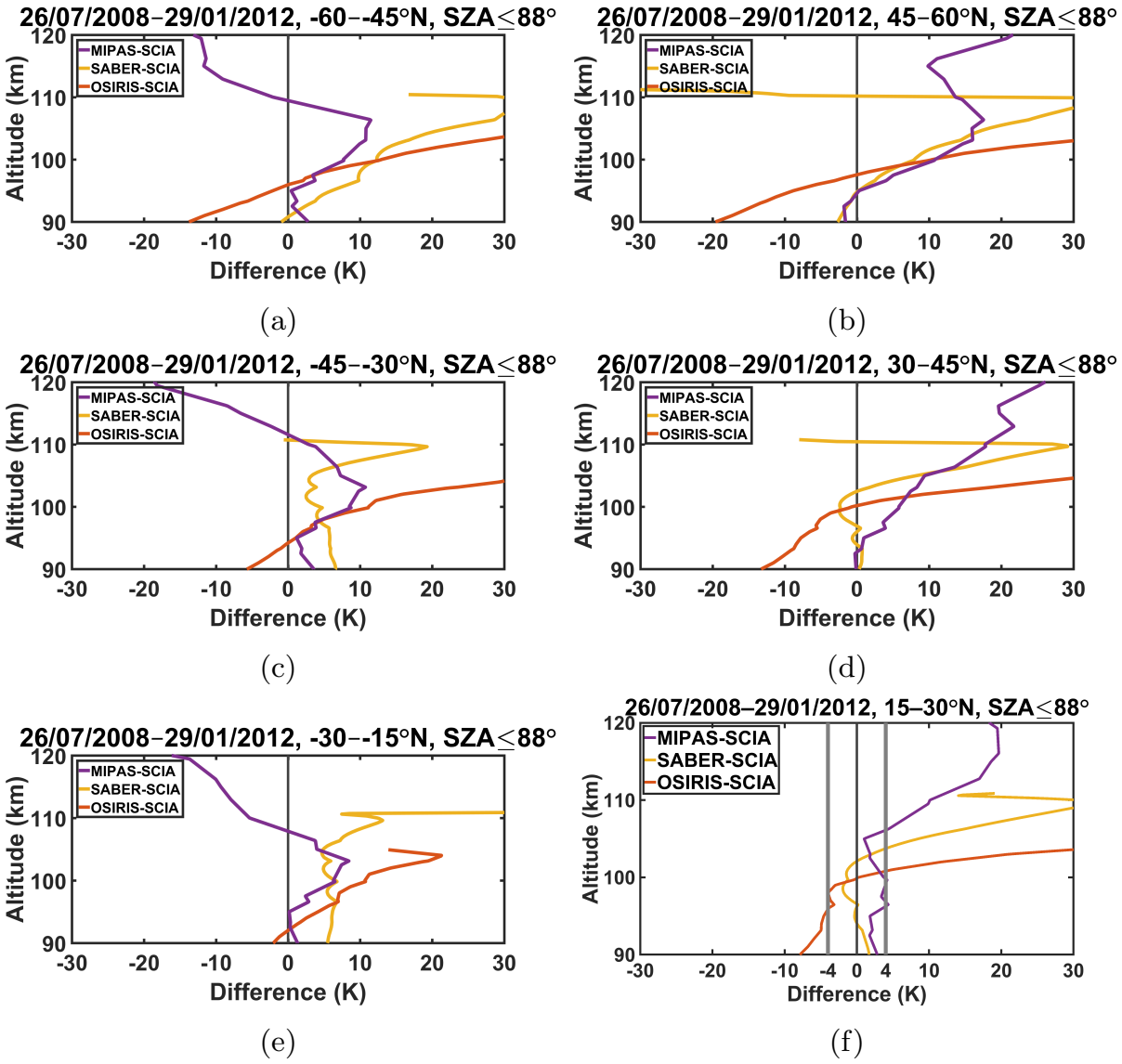

Figure 4.11: Differences between the SCIAMACHY retrieved temperatures profiles with instruments including MIPAS (blue), SABER (yellow), and OSIRIS (red) at 15° latitude bins, corresponding to the profiles shown in Figure 4.10.

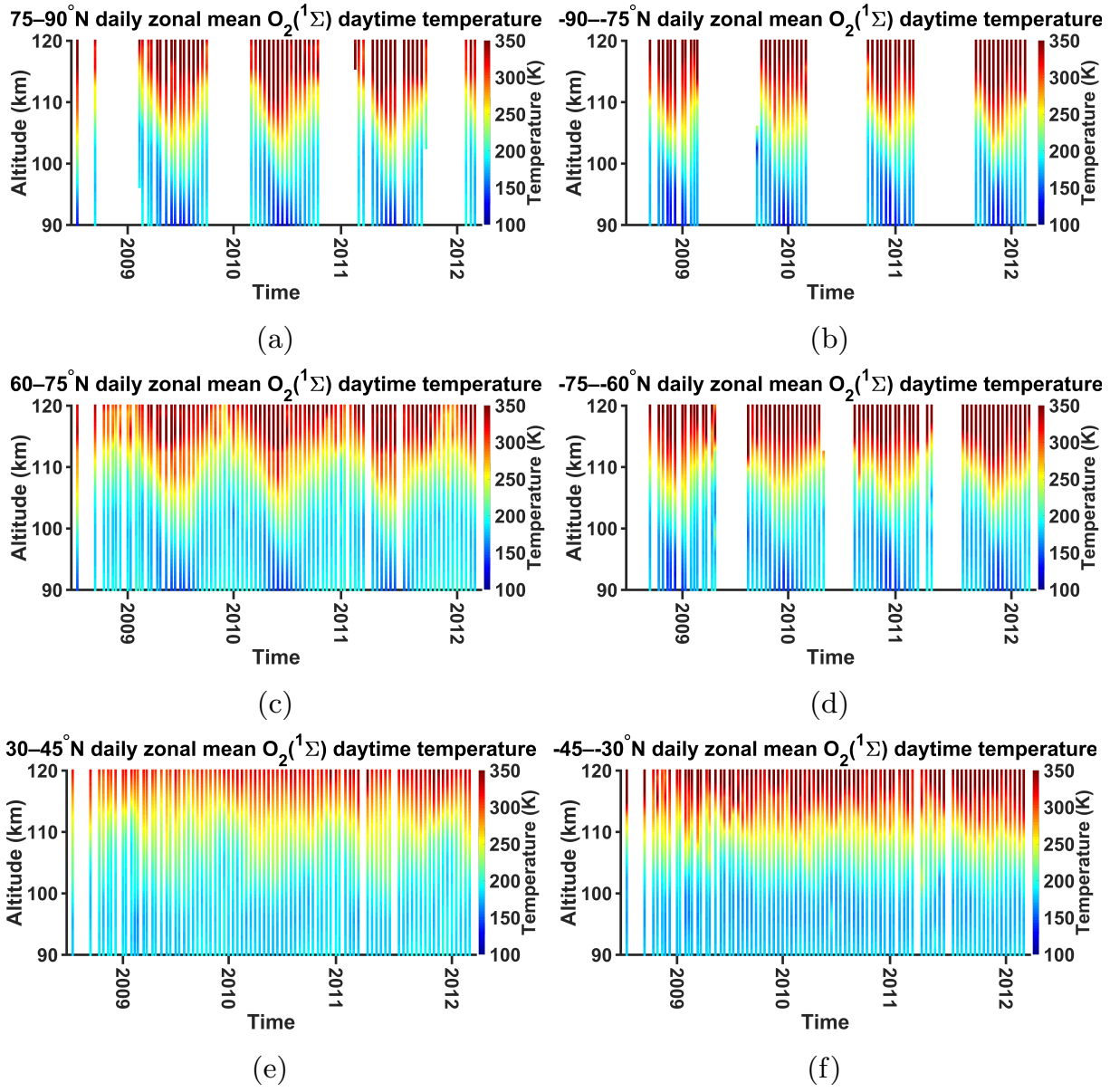

Figure 4.12: Northern hemispheric (left panel) versus southern hemispheric (right panel) time series of the daily zonal mean retrieved temperatures averaged over 15° latitude bins.

4.6 Temperature climatology

Figures 4.13a to 4.13f show annual mean monthly averages of MLT retrieved temperatures exemplarily for January to June. July to December are given in Figure 7.11a to 7.11f in the Appendix, in Section 7.4. The altitude ranges are restricted to 90–105 km, because as discussed in Section 4.2, there are discrepancies in the temperature retrieval below ∼90 km altitude. The upper limit of the Figures 4.13a to 4.13f are restricted to 105 km because of the better representation of the color scale, as the full altitude ranges are shown in Figures 7.11 and 7.13 in Appendix, Section 7.4.
The coldest summer mesopause is easily seen in Figures 4.13f and 7.11f for June and December, respectively. Warmest temperatures appear in the summer in the thermosphere (above 100 km) at high latitudes, that is, above the minimal temperatures of the high-latitude summer mesopause. In the winter hemisphere, the difference between mesosphere and thermosphere temperatures is lower as the vertical temperature gradient is lower there. In the tropics, there is a "tongue" structure of warm temperatures. A two cold cores temperature feature with a warm tongue in between is seen Figure 4.13c for March, and in Figure 7.11c for September, which varies in strength throughout the year. It appears to be stronger during equinoxes than during winter/summer solstices.

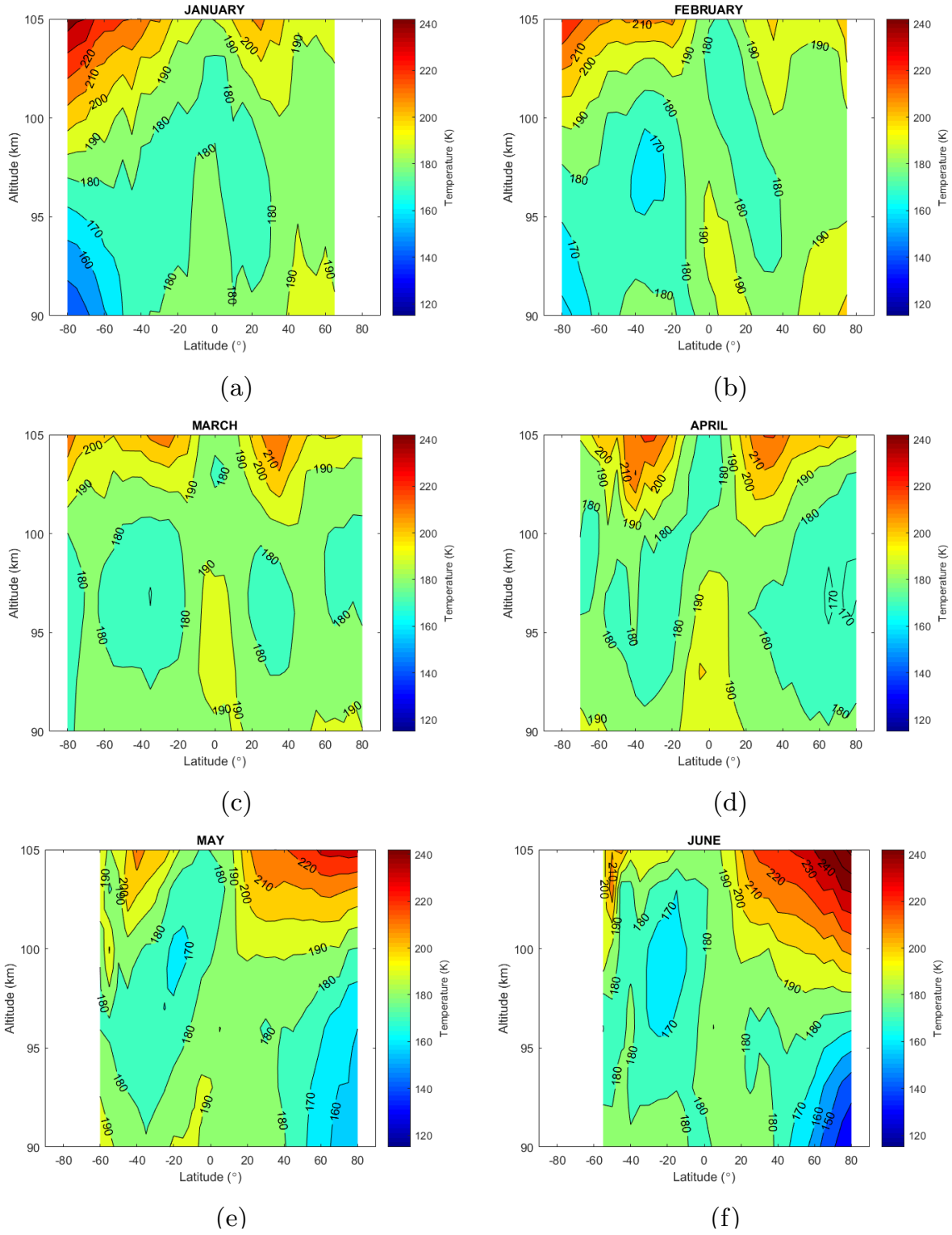

Figure 4.13: Monthly mean climatology of MLT retrieved temperatures

5 Case study: Response of O_2 VERs and temperatures in the MLT region to a sudden stratospheric warming

Stratospheric sudden warmings (SSWs) are dynamical phenomena in the wintertime polar stratosphere which arise from a strong increase in the upward propagating planetary waves which interact with the mean flow (Matsuno (1971)). Among the complex phenomena which a stratospheric sudden warming includes, three major features are observed in the stratosphere: A breakdown of the stratospheric polar vortex, a sudden warming of the stratospheric polar air, and the appearance of circumpolar easterly winds after the weakening and disappearance of the westerly jet (Matsuno, 1971). As a large-scale meteorological process in the winter polar region, it strongly affects vertical coupling in a large range of altitudes, from the stratosphere to the thermosphere (Liu et al., 2010). Pedatella et al. (2018) show strong connection between stratospheric sudden warmings and extensive changes throughout the Earth's atmosphere. A response to sudden stratospheric warmings is even observed in the equatorial total electron content above 200 km altitude (Chau et al., 2012). Understanding these coupling mechanism therefore has the advantage of improved tropospheric and space weather predictions. Based on the temporal evolution of the mesospheric temperature during the SSW, Gao et al. (2011a) have divided the response in the mesosphere into three stages: the normal stage before the onset of the SSW; the cooling stage during the stratospheric warming; recovery phase after the stratospheric warming. In the cooling phase, an abrupt change in the stratospheric zonal wind leads to a filtering out of the gravity waves penetrating upward to the mesosphere. This stops the meridional overturning circulation in the polar and mid-latitude mesosphere, and leads to a decrease in the dynamical heating of the winter-time upper mesosphere, that is, a net cooling. In the so-called recovery phase of the SSWs, reformation of the jet changes the propagation of the gravity wave into the mesosphere. Induced change in the residual circulation results in the enhancement of the air descent. This leads to the diabatic heating and the reformation of the stratopause at about 75–80 km altitude after particularly strong events (Siskind et al. (2010)). According to Harada et al. (2010) a major SSW occurred around 21 January 2009 (Figure 1 of that paper). According to Gao et al. (2011a), the

mesospheric cooling phase of this event lasted from January 15 - 22 2009, and the recovery phase started on January 23. They reported that the O_2 nightlow brightness decreased by a factor of 10 during the cooling stage and then increased by a factor of 3 during the recovery stage, relative to the normal stage. An unusual brightening of the OH airglow has been observed related to a different sudden stratospheric warming occurring in winters 2004 and 2006 (Winick et al. (2009)) and was interpreted as an enhancement of down-welling of atomic oxygen. Funke et al. (2010) discussed that on the SSW of January 2009, they observe clear signatures of a mesospheric cooling and thermospheric warming during the mesospheric cooling phase of the SSW, the latter peaking at ∼120–140 km in agreement with model predictions.

In the following, I will investigate whether the sudden stratospheric warming of January 2009 had an impact on the O_2 dayglow and MLT temperatures. Section 5.1 includes assessing the relationship between the VER time series variations retrieved from both $O_2(^1\Sigma)$ and $O_2(^1\Delta)$ on the SCIAMACHY observation days before, during, and after the stratospheric sudden warming. In Section 5.2, the relationship between the temperature variations on the SCIAMACHY observation days before, during, and after the stratospheric sudden warming event is investigated. In Section 5.3, a summary assessment of the observed changes in O2 dayglow and MLT temperatures is given.

5.1 Relation between VER time series variations and stratospheric sudden warmings-example

Figures 5.1a and 5.1b show the daily mean VER of daytime $O_2(^1\Sigma)$ and $O_2(^1\Delta)$, averaged from 60°N to 70°N during 12/2008 until 04/2009. It is observed that on the last day of the cooling stage, i.e. on 22 January 2009, daily mean VERs of $O_2(^1\Sigma)$ and $O_2(^1\Delta)$ show a strong decrease in the maximum intensity in the altitude range of 82–87 km. Larger intensities are observed on the following SCIAMACHY measurement day by about three weeks later, i.e. on 10 February 2009. This is consistent with a decrease of atomic oxygen due to horizontal mixing and up-welling during the cooling stage, and then downward extension of the MLT region with high number densities of O during the recovery stage of the SSW as discussed by Gao et al. (2011b). The signal to noise ratios of the VERs for $O_2(^1\Sigma)$ are depicted in Figure 5.1c for $O_2(^1\Sigma)$ and Figure 5.1d for $O_2(^1\Delta)$, and show that the observed changes of both airglow signals throughout the SSW are statistically significant.

In summary, we observe a strong decrease of both airglow signals in the 82–87 km altitude range during the cold phase of the event, and a strong increase of a factor of up to 1.6 in the recovery phase. This is consistent with the view of Gao et al. (2011b) of a strong

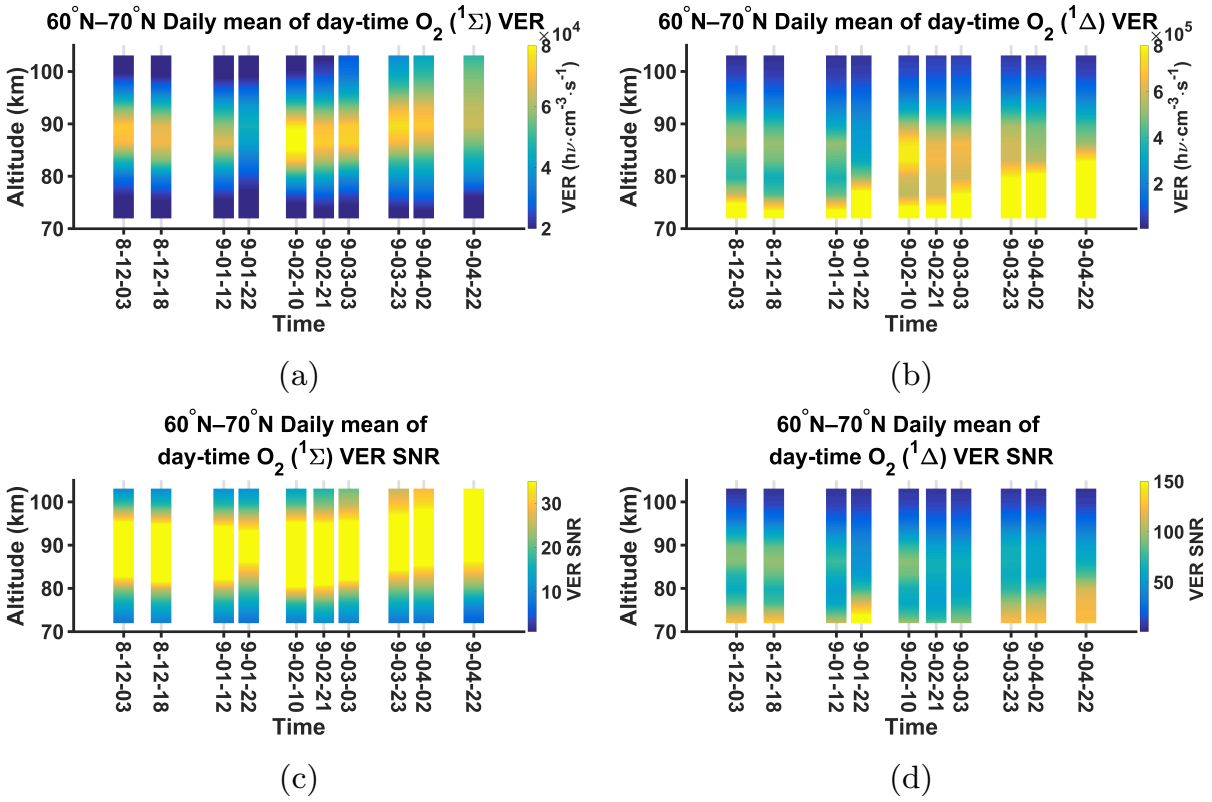

Figure 5.1: (a) Daily mean of the daytime $O_2(^1\Sigma)$ VER from December 2008 to April 2009 averaged between 60°N and 70°N latitude. (b) as (a) for $O_2(^1\Delta)$ band. (c) Daily mean of the signal to noise ratios of the daytime $O_2(^1\Sigma)$ VER for the same dates and latitudes. (d) as (c) for $O_2(^1\Delta)$ VER signal to noise ratios (Zarboo et al., 2018).

increase of atomic oxygen in the recovery phase due to enhanced transport of thermospheric air into the MLT region.

5.2 Relation between temperature time series variations and stratospheric sudden warmings

Figure 5.2 shows the temperature time series averaged over 60°–70°N on the dates before, during and after the stratospheric sudden warming event on 22 January 2009. On the last day of the cooling phase of the stratospheric sudden warming of January 2009 (hereafter SSW of January 2009) the cold mesopause descends and cools compared to before 22 January 2009, and a strong warming develops in the thermosphere (around 113 km). On

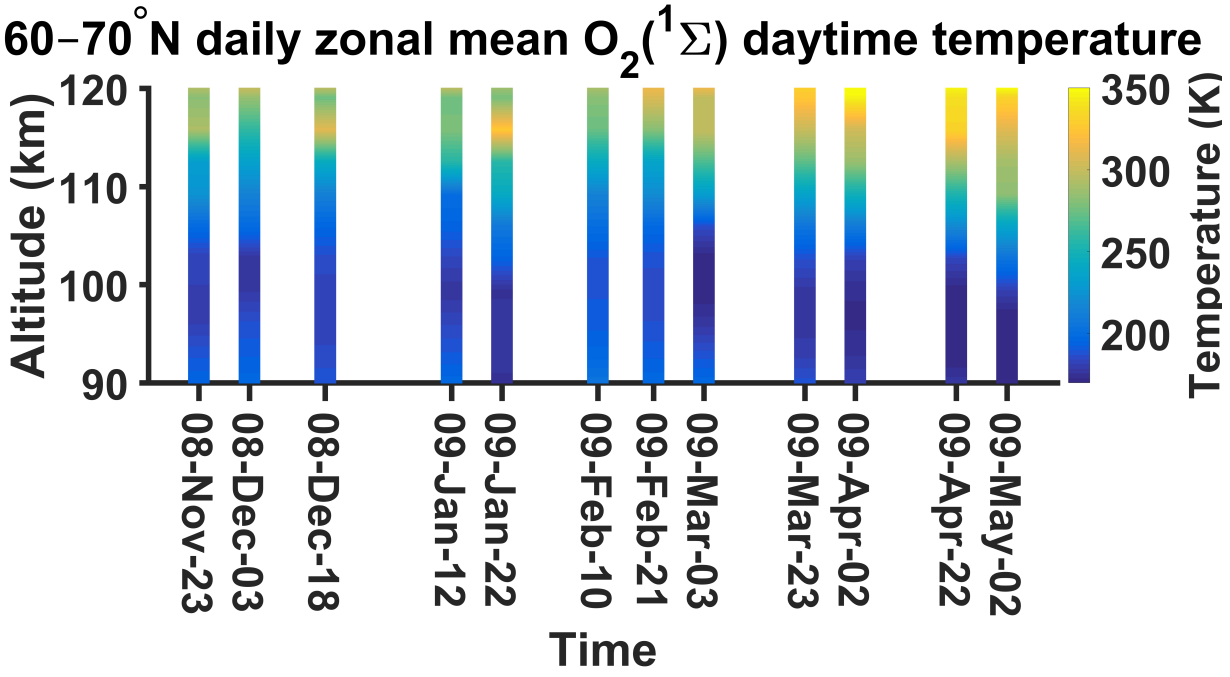

Figure 5.2: Time series of the daytime $O_2(^1\Sigma)$ retrieved temperatures averaged on 60–70°N latitudes. The temporal variation is shown around the stratospheric sudden warming event 2008–09.

the next observation days, i.e., February 10 and 21 of 2009 the temperature minimum of the mesopause disappears and instead, warm temperatures occur which indicates development of a warm layer in these altitudes, that is, an elevated stratopause. This warm layer moves down with time, vanishing from the MLT region above 90 km altitude on March 9, 2009. In the lower thermosphere (113 km), temperatures are again much colder than on January 22, particularly on February 1, 2009. This is consistent with Funke et al. (2010) in the cooling/warming of the mesosphere/thermosphere during the mesospheric cooling phase of the SSW 2009.

Temperature differences versus climatological monthly mean as described in Chapter 4 are shown at 90 km in Figure 5.3 and at 113 km in Figure 5.4 for January 12 and 22 and February 10 and 12, that is, before, during and after the SSW. In 90 km altitude, there was a cooling at high latitudes (40–60°N) after the inception of the SSW of January 2009 event on January 22. A warming evolves at northern tropical latitudes and a cooling in the southern tropical latitudes after the warming on February 10.

At 113 km altitude, a longitude dependent warming/cooling after the inception of the SSW of January 2009 event is observed on January 22. The warming occurs at -60–60°E at high latitudes (40–60°N), while the cooling is observed 60–300°E at extended region of latitudes. A pronounced cooling comes after the warming on 10 February in the whole Northern hemisphere, with a longitudinally extended band of warming in the Southern

hemisphere at -50–0°S. On the next observation day on 21 February, a decrease in the cold and warm features in both hemispheres is observed besides that the cold feature splits into parts. This is consistent with Funke et al. (2010) in the cooling /warming of the mesosphere /thermosphere in the SSW of January 2009 event. The temperatures at 90 and 113 km altitudes, as well as the climatology of temperatures which are subtracted from on January and February are shown in Appendix in Figures 7.14, 7.15 and 7.16 respectively.

5.3 Response of O_2 VERs and temperatures during SSW

During the cooling phase of the January 2009 SSW, a cooling is observed in the uppermost mesosphere (90–100 km) at high latitudes accompanied with a strong decrease of the $O_2(^1\Sigma)$ and $O_2(^1\Delta)$ dayglow. At the same time, the lower thermosphere around 113 km altitude warms considerably. During the recovery phase of the SSW, an elevated stratopause develops at high latitudes, accompanied by a strong increase in the O_2 dayglow. Both signals move down in the following weeks, and recovery to the normal phase is reached by March 2009. At the beginning of the recovery phase on February 10, a strong warming is observed in the upper mesosphere at low latitudes of the Northern hemisphere, indicating that the SSW leads to changes in the uppermost mesosphere covering at least the whole Northern hemisphere. In the following, an explanation of these observations is provided as a disturbance of the meridional overturning circulation connecting the summer and winter hemisphere in the upper mesosphere.

In the mesospheric cooling stage (stratospheric warming stage) the abrupt change in the stratospheric zonal wind leads to filter out the gravity waves penetrating upward to the mesosphere. This stops the meridional overturning circulation in the upper mesosphere and leads to the decrease in the dynamical heating of the winter-time upper mesosphere, i.e., net cooling there. Two possible explanations are provided for the low-latitude response during the recovery phase. In the mesospheric warming stage, there is still a residual transport across the equator due to the branch of meridional overturning circulation in the summer hemisphere. However, the middle to high latitudes transport in the winter hemisphere which leads to a net adiabatic compression is suppressed during the cooling stage, and this suppression leads to a strong adiabatic compression of air, and a net warming, which slowly moves to low latitudes, leading to the observed time lag. The other process which contributes to the mesospheric warming during the recovery phase of the stratospheric warming event is that mesopause cooling at high latitudes leads to the enhancement of the meridional temperature gradient between low and high latitudes which affects zonal (thermal) wind speed at middle latitudes. Filtering gravity waves by zonal wind changes the gravity wave drag at middle latitudes and change in the large scale adiabatic motions due to the gravity wave drag , leads to the subsequent adiabatic warming at low latitudes.

Again, this change at the low and middle latitudes, is followed by the mesospheric cooling at high latitudes with a time lag.

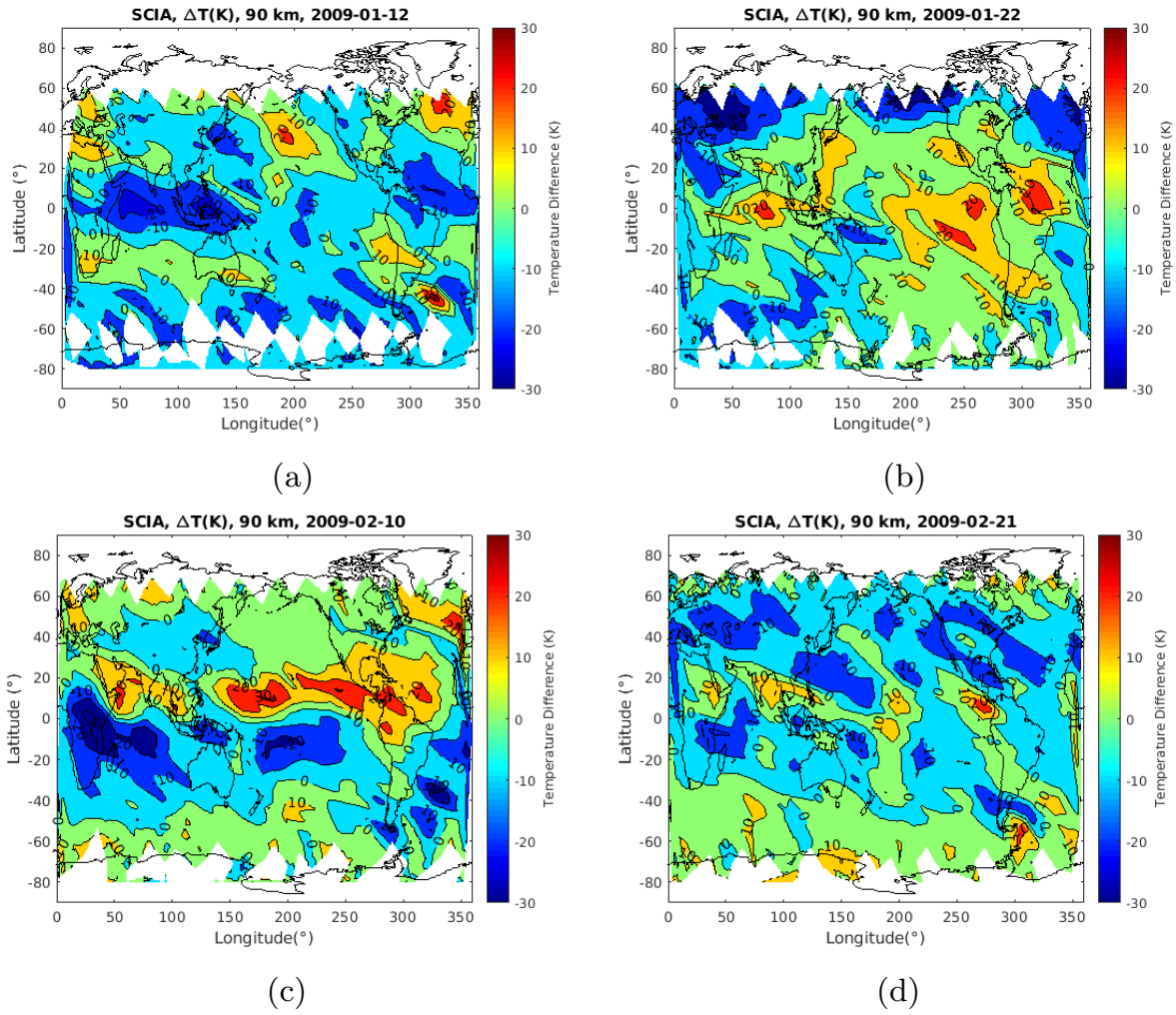

Figure 5.3: Longitude-latitude map of temperature difference with monthly mean climatology at ∼90 km altitude, as retrieved by SCIAMACHY on the MLT scan days during and after the SSW of January 2009 event (See text for SSW of January 2009 event definition.)

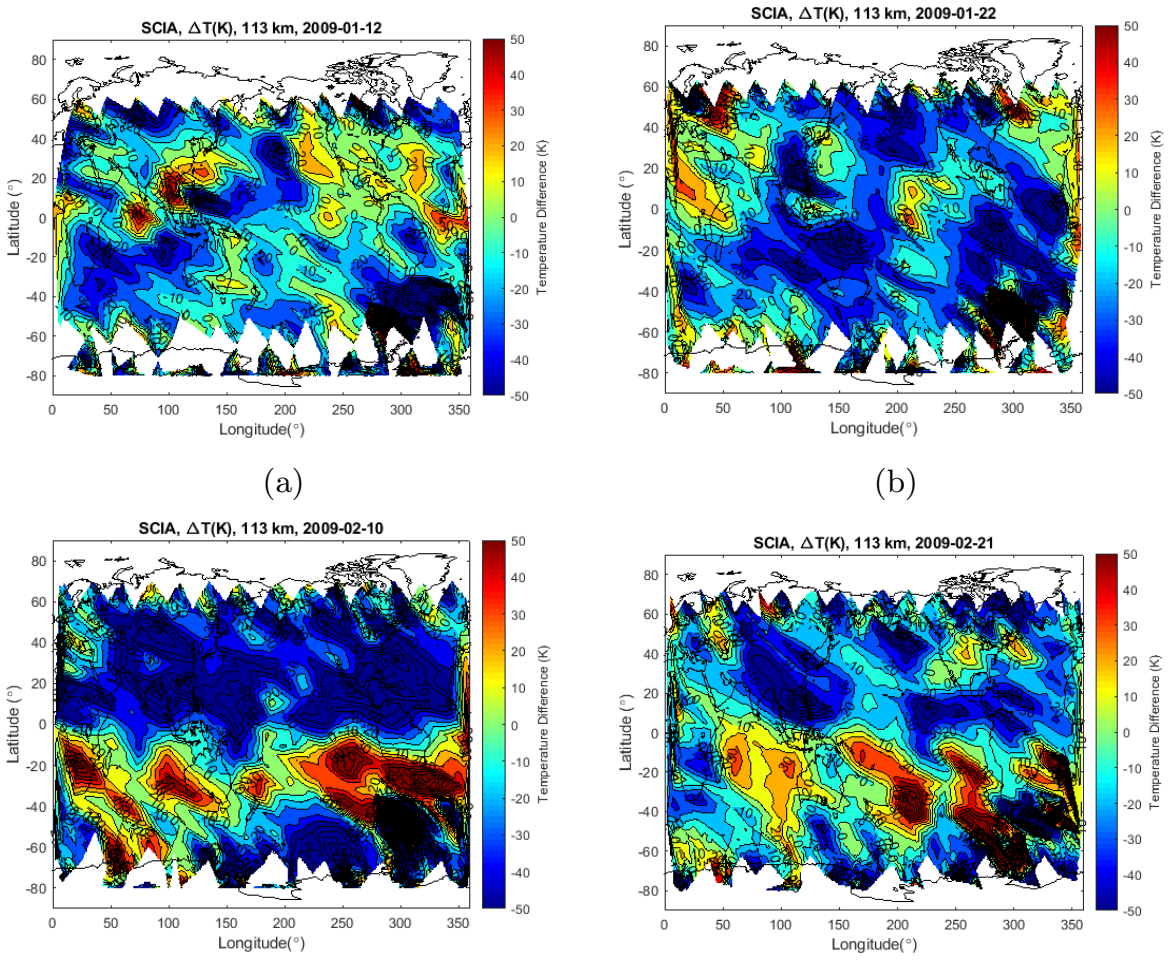

Figure 5.4: Same as Figure 5.3, but for 113 km altitude.

6 Summary and Outlook

In this work, I developed retrieval algorithms for two mesospheric components important for the energy budget of the MLT region, the O_2 dayglow and temperatures, using data from SCIAMACHY on-board the Envisat satellite. I retrieved the emission intensities and volume emission rates of the $O_2(^1\Sigma)$ and $O_2(^1\Delta)$ spectral bands. Analysis of the full time-series has shown that the maximum variability of the $O_2(^1\Sigma)$ emission correspond to the minimum solar zenith angle. At high latitudes in northern springs maximums of $O_2(^1\Sigma)$ are seen which are explained by high concentrations of atomic oxygen resulting from vertical mixing from the lower thermosphere in the stratospheric sudden warming events. Peak values of $O_2(^1\Delta)$ as seen by SCIAMACHY, are qualitatively consistent with being dominated by ozone photolysis, as both ozone and the $O_2(^1\Delta)$ airglow peak in the lower mesosphere. This is confirmed by sensitivity studies with a 1-D photochemical model. The secondary maximum of $O_2(^1\Delta)$ at about 80–90 km is consistent with being formed by the secondary maximum of ozone at these altitudes. They are only observed in hemispheric winters at high latitudes which is consistent with high abundances of atomic oxygen and therefore ozone in these regions. $O_2(^1\Sigma)$ airglow below ∼90 km is mostly affected by molecular oxygen, ozone, and solar zenith angle, respectively. Above ∼90 km solar zenith angle, molecular oxygen, ozone, and atomic oxygen play the important role by their contribution. For influencing the $O_2(^1\Delta)$ airglow below ∼85 km, ozone, molecular oxygen, and solar zenith angle play the most important roles respectively. Above ∼85 km solar zenith angle, molecular oxygen, atomic oxygen, and ozone play the most important roles respectively.

Temperature in the MLT region was retrieved from the $O_2(^1\Sigma)$ emission intensities. Sensitivity studies varying input parameters indicate a spectral shift in the spectra presumably due to problems with the wavelength attribution of the SCIAMACHY spectra in this channel, as well as a large sensitivity to excluding the peaks or parts of the wings of the spectra particularly below 90 km altitude. The latter is probably due to self-absorption, which affects the $O_2(^1\Sigma)$ emissions below 90 km altitude. In the following, I considered the whole spectral interval for $O_2(^1\Sigma)$ emission intensity and developed an optimum selection algorithm for the spectral shift over [-0.1,0.1] nm, I reached the best accuracy in the temperature retrieval at the 90–120 km altitude range. The temperature uncertainty is $\leq\pm 10$ K in this altitude range. Evaluating our retrieved quantities imply reasonable agreement of the averaged temperature profiles in the 90–120 km altitude range with MIPAS, SABER,

and OSIRIS instruments in the ±10 K range. Analyzing temperature time series indicate annual variability in Northern and Southern Hemispheres with higher/lower values during summertime at lower thermosphere/mesopause altitudes. The temperature climatology on the available data-set represents a notable cooling of the summer mesopause in both hemispheres which is consistent with the gravity wave driven motion which induces vertical-meridional circulation in the winter hemisphere and subsequent remarkable enhancement of the temperature gradient in the other hemisphere. In spring and autumn, a structure consisting of two cold cores at mid-latitudes and a warm tongue between them above the equator is seen in the upper mesosphere and lower thermosphere.

Investigating the relationship between the volume emission rates and temperature variations from a few days before, during, and after the stratospheric sudden warming 2009, I observed the following: In both $O_2(^1\Sigma)$ and $O_2(^1\Delta)$ bands, on the onset of the stratospheric warming event 2009, a remarkable de-intensification of the volume emission rates is observed which is in agreement with the up-welling and horizontal mixing which results in the decrease of the atomic and molecular oxygen concentrations and subsequent decrease in the production and loss rates in the $O_2(^1\Sigma)$ and $O_2)(^1\Delta)$ bands. An intensification of the volume emission rates after the event is also observed which is interpreted with the vertical mixing from the lower thermosphere into the MLT. Temperature variabilities show cooling in the mesosphere and warming in the thermosphere during the stratospheric sudden warming event. The effects in the mesosphere are manifested as planetary wave disturbance which approaches tropical latitudes in the form of a warm-cold disturbance.

The data-sets that I derived during my work can be further analyzed to investigate O_2 dayglow and temperature variability in the MLT region. More data-sets can be derived with the retrieval algorithm I developed, and with the data-sets I provided, such as O_3 and solar heating, as this can be derived directly from my results. As an outlook for this work it would be very useful to extend the retrieval algorithm to the twilight and night spectra of $O_2(^1\Sigma)$ and $O_2(^1\Delta)$ bands which encompasses the whole 2002–2012 SCIAMACHY data-set. Also derivation of ozone concentration and solar O_3 heating rates in the mesosphere is suggested. The ozone retrieval does not work above the mesopause, but does work well down to about 60 km from the available data-set to study the energy budget of the MLT region in more detail which is suggested as extensions to this work.

7 Appendix

7.1 Additional Figures of Chapter 3

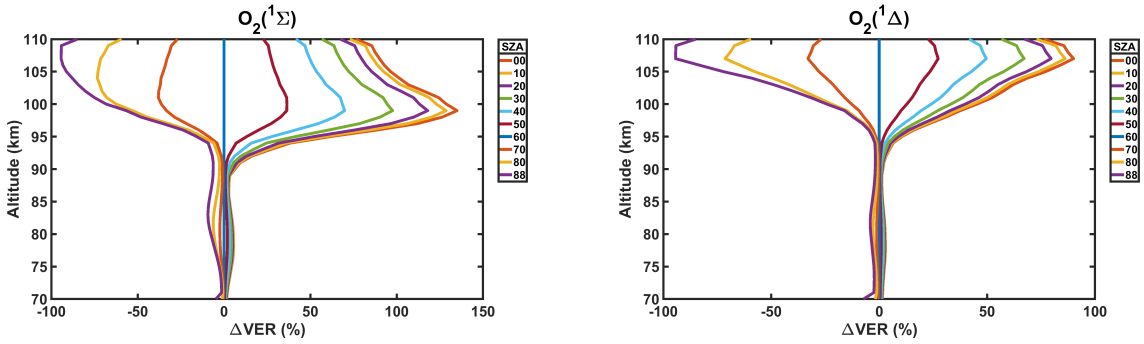

(a) (b)

Figure 7.1: FIgure 3.10 and 3.11 with the wider range to focus on effect of changing in solar zenith angle on the $O_2(^1\Sigma)$ (left) and $O_2(^1\Delta)$ (right) VERs at higher altitudes.

7.2 Derivation of $O_2(^1\Sigma)$ line strength

The line strenghts of the $O_2(b^1\Sigma_g^+) \rightarrow O_2(X^3\Sigma_g{}^-)$ transition are calculated as follows (Herzberg, 1950):

$$S_j = \frac{d_j N_{uj} I_0}{U_{ul}.E_{vibr.}}.v_{ul}^3 \tag{7.1}$$

in which S_j is the line strength, j is the angular momentum, d_j is the degeneracy, and $E_{vibr.}$ is the energy of vibrational transitions.

$$I_0 = \frac{A_{evib}}{8\pi c Q_r(T)} \tag{7.2}$$

in which, Q_r(T) is the partitioning function.

$$Q_r(T) \approx \frac{3kT}{2B_v} \tag{7.3}$$

$$N_{uj} = \exp\{-E_{rotj}/kT\} \tag{7.4}$$

in which N_j denotes population densities, and k is the "Boltzmann" constant.

$$E_{rot.j} = B_v J(J+D) - D_v J^2(J+1)^2 + H_v J^3(J+1)^3 \tag{7.5}$$

in which the molecular constants are

$$\begin{aligned} B_v &= B_e - \alpha_e(v+1/2) \\ D_v &= D_e + \beta_e(v+1/2) \end{aligned} \tag{7.6}$$

$$\begin{aligned} P_{Pbranch} &: \Delta J = -1, \quad \Delta K = -1 \\ R_{Rbranch} &: \Delta J = +1, \quad \Delta K = +1 \\ P_{Qbranch} &: \Delta J = 0, \quad \Delta K = -1 \\ R_{Qbranch} &: \Delta J = 0, \quad \Delta K = +1 \end{aligned} \tag{7.7}$$

considering that the transition in which:

$$J = 0 \iff J = 0 \tag{7.8}$$

is forbidden. In each transition from upper level to the lower level:

$$j_u \to j_l \quad , j_u = 0, 2, 4, 6, \ldots, 60 \tag{7.9}$$

The total energy is the sum of energies:

$$E_{uj} = E_{el} + E_{vib} + E_{rot}(j_u) \tag{7.10}$$

in which for $O_2(^1\Sigma)$ band, E_{el} is the electronic energy level of the 760 nm emission/absorption of oxygen. E_{vib} is the vibrational energy state, which is calculated as:

$$E_{vib} = \omega_e(v+1/2) - \omega_e x_e(v+1/2)^2 + \omega_e y_e(v+1/2)^3 \tag{7.11}$$

in which ω_e is the diatomic molecular constant. For the calculations, v_{ul} and v_{ll} have the same units as E_{uj} and $E_{lj'}$.

$$\begin{aligned} P_P: &\quad E_{lj} = E_{elvib,l} + E_{rot}(j_u+1), d_j = 1/2(j_u+2) \\ R_R: &\quad E_{lj} = E_{elvib,l} + E_{rot}(j_u-1), d_j = 1/2(j_u-1) \\ R_Q: &\quad E_{lj} = E_{elvib,l} + E_{rot}(j_u) + E_{trip}(j-1), \quad d_j = \frac{s_j^2(2j+1)}{2} \\ P_Q: &\quad E_{lj} = E_{elvib,l} + E_{rot}(j_u) + E_{trip}(j+1), \quad d_j = \frac{c_j^2(2j+1)}{2} \end{aligned} \tag{7.12}$$

in which s_j and c_j are as follows:

$$\begin{aligned} s_j^2 &= \frac{-F_1}{F_3 - F_1} \\ c_j^2 &= \frac{F_3}{F_3 - F_1} \end{aligned} \tag{7.13}$$

in which F_1 and F_3 are as follows:

$$\begin{aligned} F_1 &= E_{rot}(j-1) + E_{trip,1}(j-1) - E_{rot}(j) \\ F_3 &= E_{rot}(j+1) + E_{trip,3}(j+1) - E_{rot}(j) \end{aligned} \tag{7.14}$$

And the resulting S_j should be corrected for the available states at each level in thermal equilibrium (Gamache and Rothman, 1992):

$$S_j^{pb} = S_j \cdot [1 - e^{-v_{ul}/kT}] \tag{7.15}$$

and to account for Doppler broadening, I apply the following:

$$\tilde{S}_j(\lambda) = \frac{S_j^{pb} g_j}{\sqrt{\pi}} \cdot \exp\{-(\lambda_j - \lambda)^2 g_j^2\} \quad , \tag{7.16}$$

in which

$$\begin{aligned} g_j &= \frac{c}{\lambda_j}\sqrt{\frac{M}{2kT}} \\ \lambda_j &= \frac{10^7}{v_{ul}} \quad [nm] \end{aligned} \tag{7.17}$$

Notation	Value	Comment
B_e	$1.40041_6\ cm^{-1}$ [a]	Herzberg (1950)
α_e	0.01817_0	Herzberg (1950)
B_e	$1.44566_6 cm^{-1}$	Babcock and Herzberg (1948)
D_e	$4.95_7 \times 10^{-6}\ cm^{-1}$	Babcock and Herzberg (1948)
ω_e	$1432.6874\ cm^{-1}$	Babcock and Herzberg (1948)
$\omega_e x_e$	$13.95008\ cm^{-1}$	Babcock and Herzberg (1948)
$\omega_e y_e$	$-0.01075\ cm^{-1}$	Babcock and Herzberg (1948)
A_{evib}	$(2.1 \pm 0.1) \times 10^{-2}\ s^{-1}$	Einstein coefficient of the vibrational transition, Long et al. (2010)
H_ν	$4.2819 \times 10^{-12}\ cm^{-1}$	Long et al. (2010)

[a] Subscript denotes the first decimal which is less than the accuracy within one unit of the previous decimal.

Table 7.1: Constants used in the derivation of $O_2(^1\Sigma)$ line strengths.

7.3 Additional Figures of Chapter 4

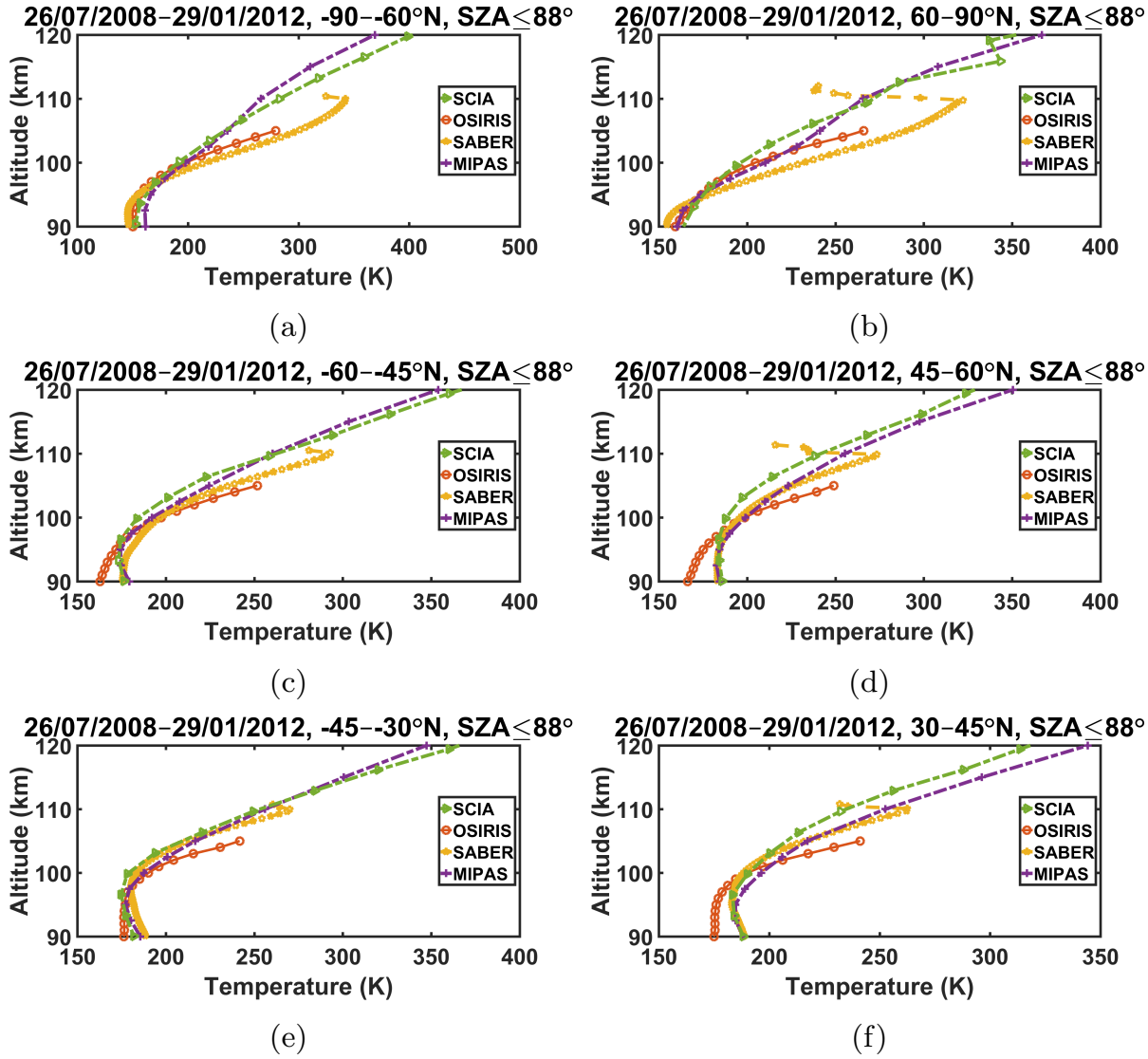

Figure 7.6: Retrieved temperatures profiles from instruments including SCIA, MIPAS instrument (blue), SABER instrument (yellow), and OSIRIS instrument (red) at different latitude boxes. Note the SCIA-MIPAS differences ranging from -8.77 K at 86 km to 9.52 K at 103 km, SCIA-SABER differences ranging from -8.42 K at 86 km to 17.52 K at 106 km, and SCIA-OSIRIS differences ranging from -18.84 K at 86 km to 28.67 K at 104 km. Also note that the SCIA-MIPAS retrieved temperatures are in agreement in the 80–120 km altitude range.

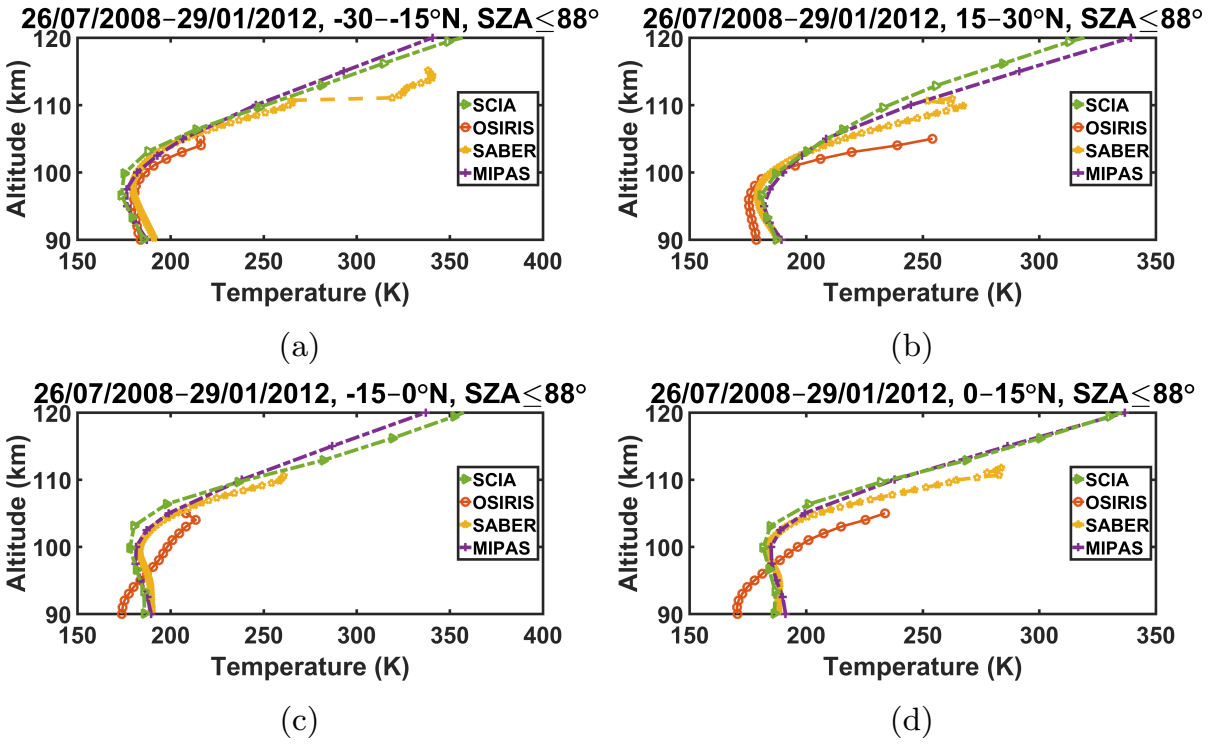

Figure 7.7: Figure 7.6 continued.

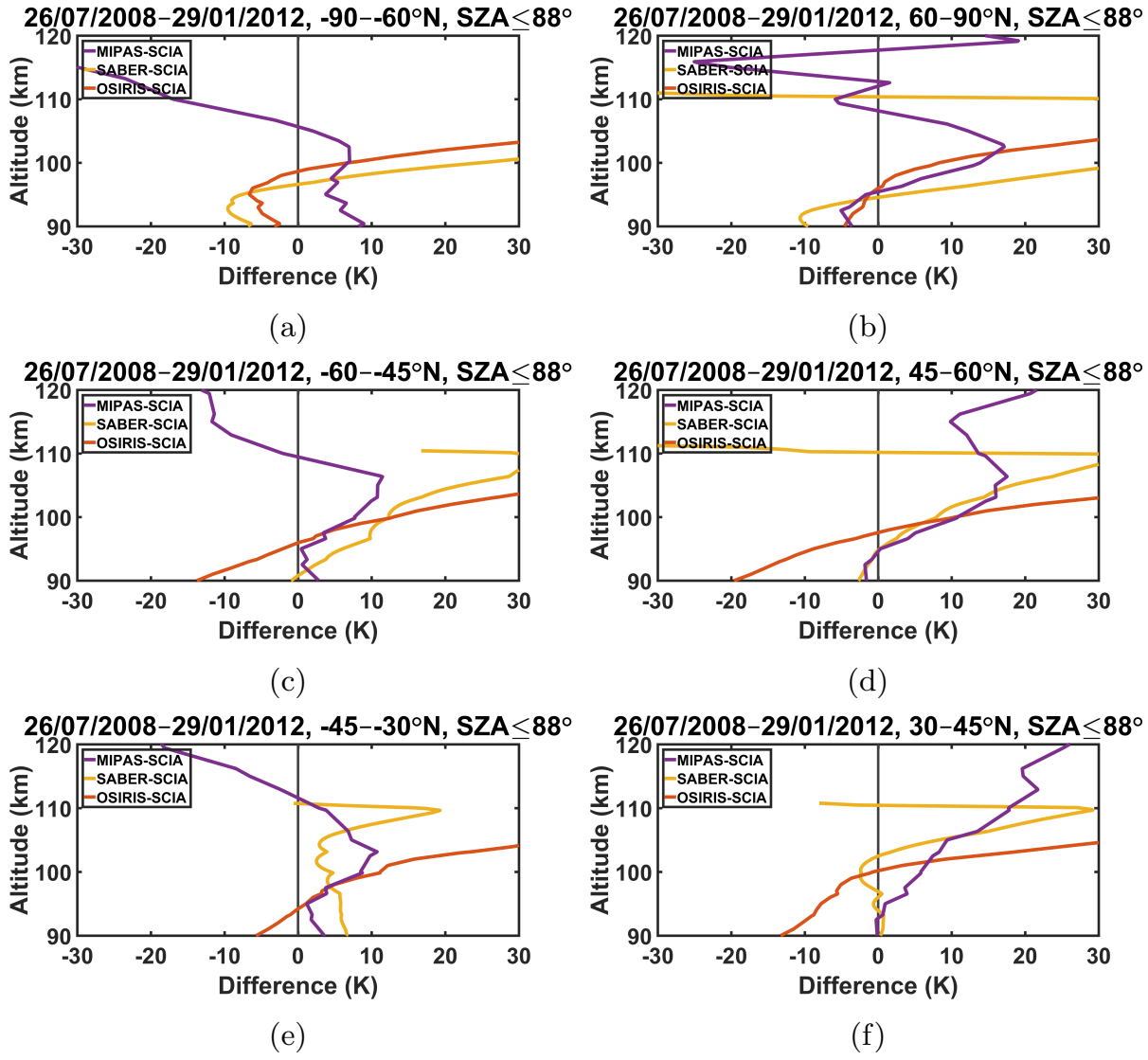

Figure 7.8: Differences between the SCIAMACHY retrieved temperatures profiles with instruments including MIPAS (blue), SABER (yellow), and OSIRIS (red) at 15° latitude bins, corresponding to the profiles shown in Figure 4.10.

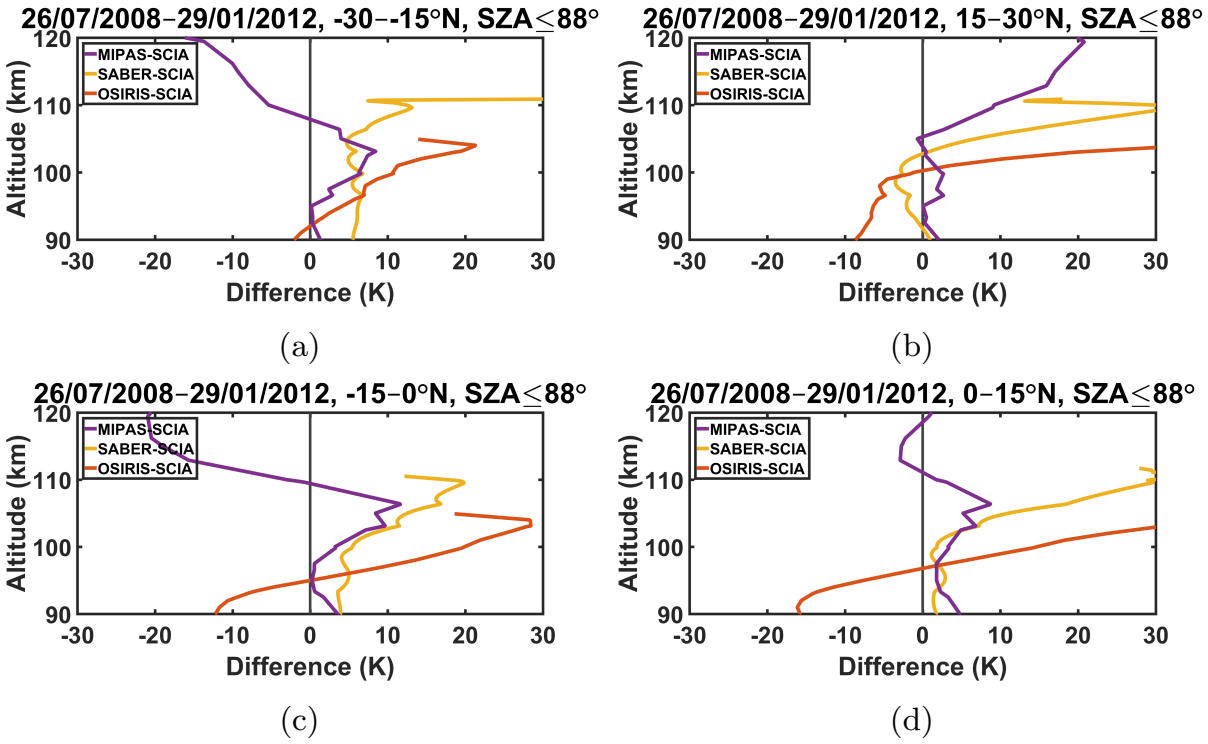

Figure 7.9: Figure 4.11 continued.

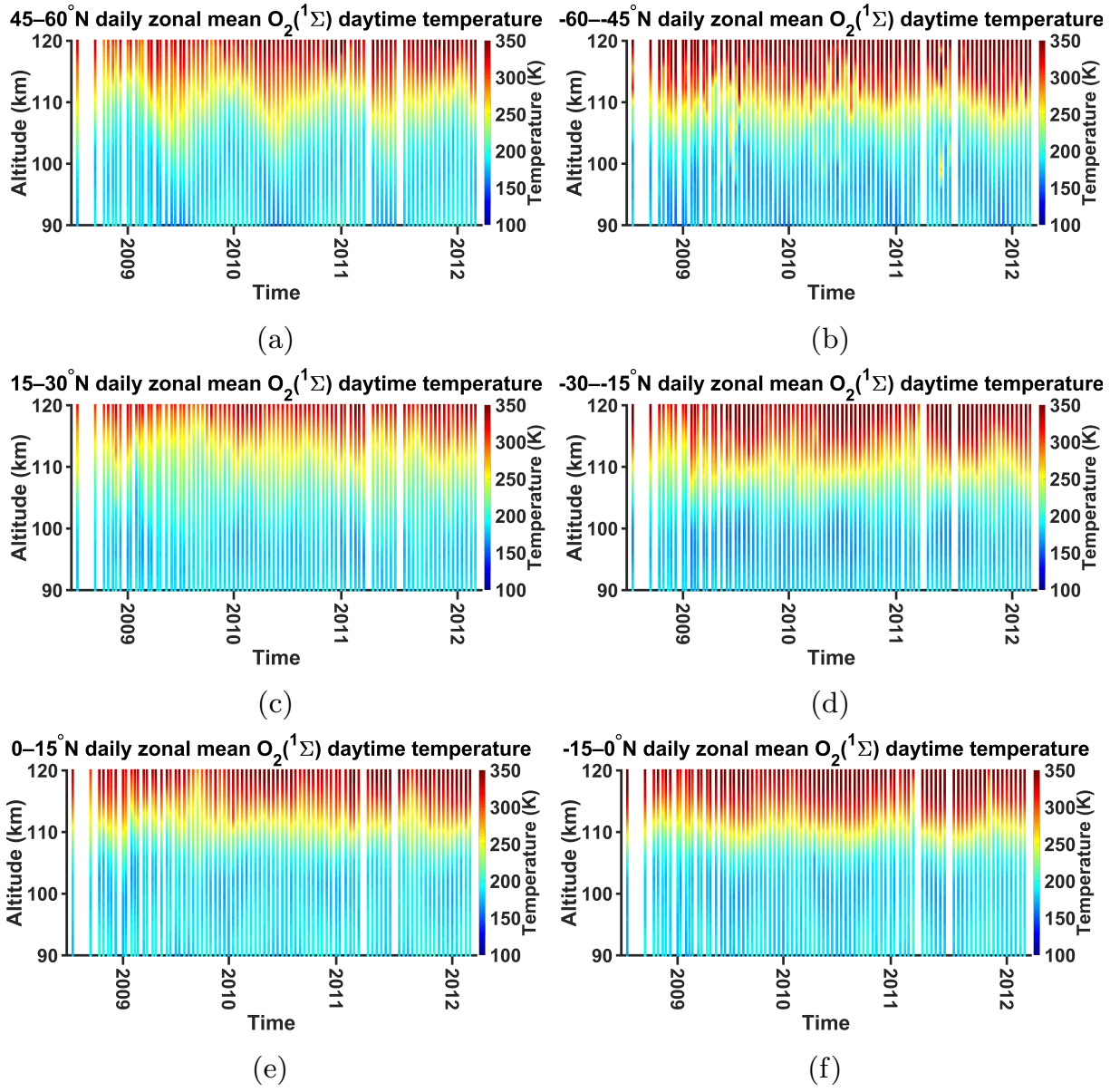

Figure 7.10: Figure 4.12 continued.

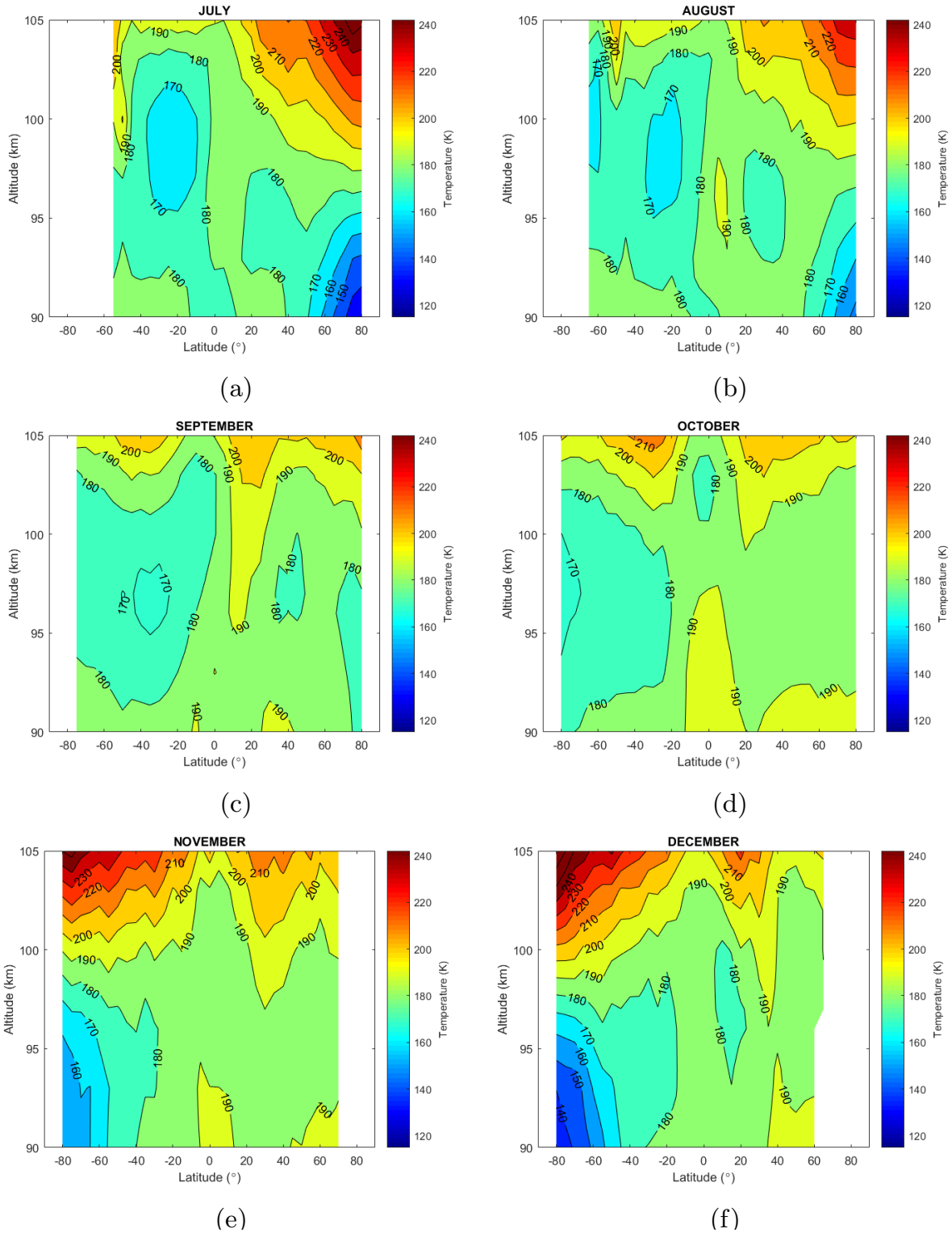

Figure 7.11: Monthly mean climatology of MLT retrieved temperatures

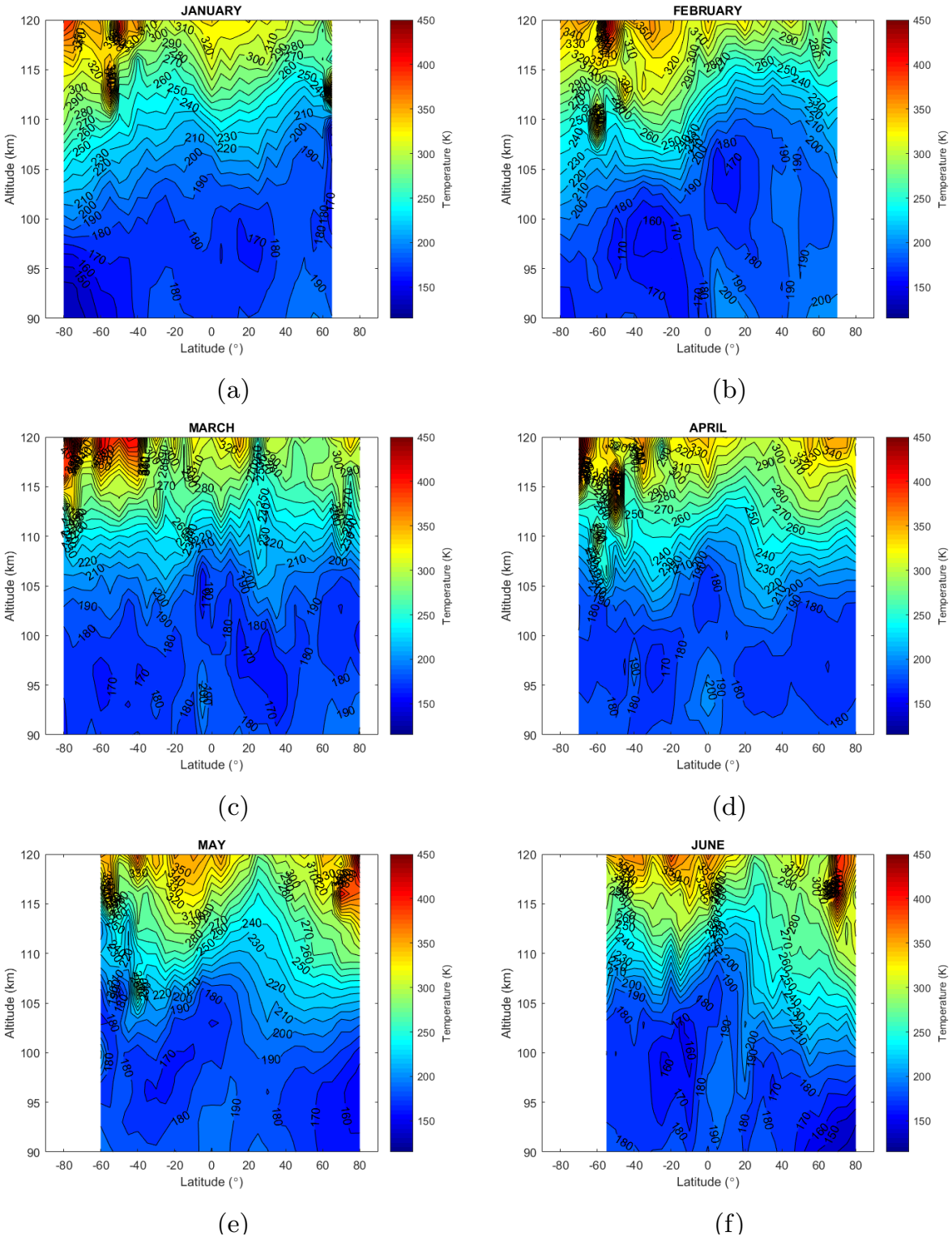

Figure 7.12: Same as Figure 4.13, but for the whole 90–120 km altitude range.

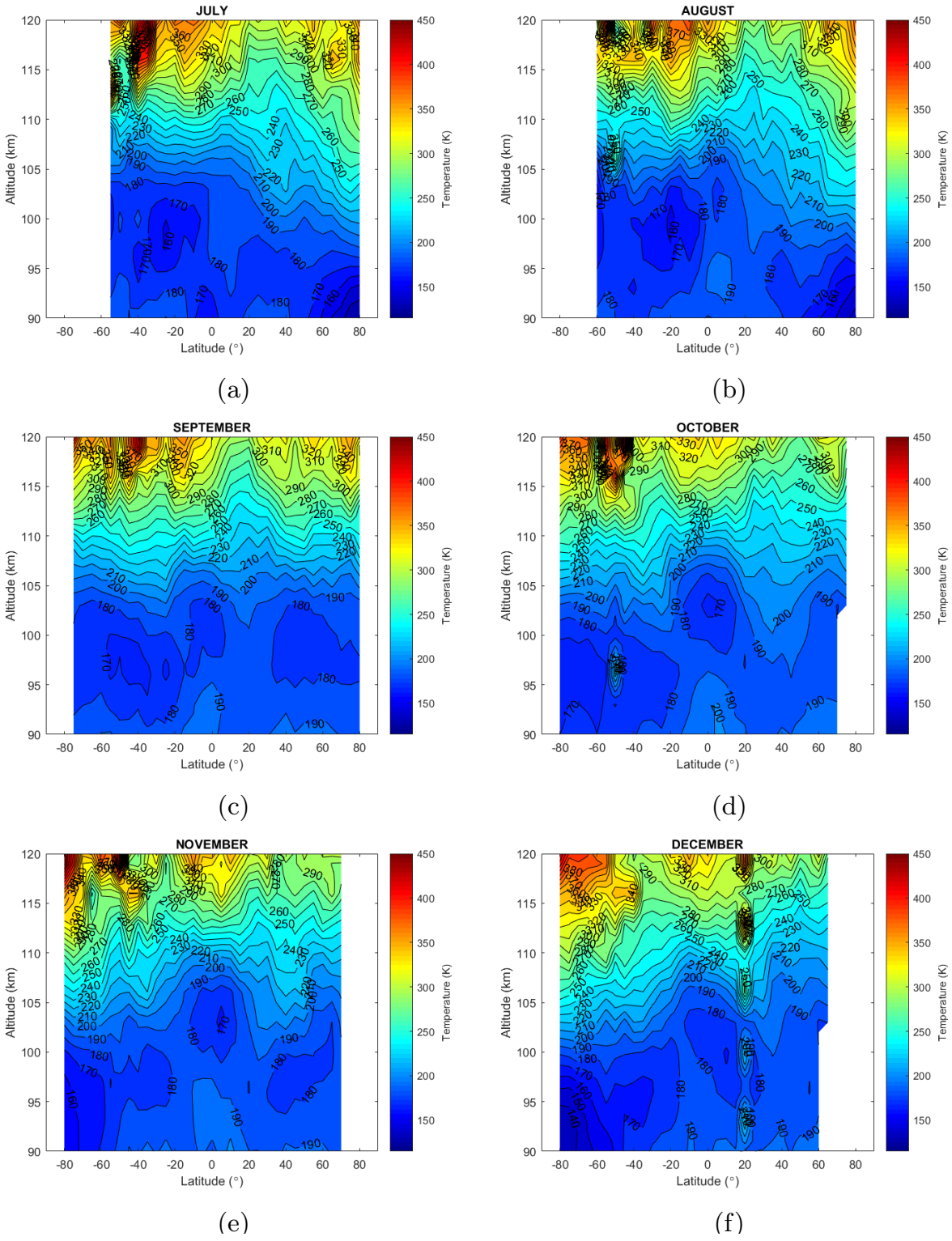

Figure 7.13: Same as Figure 7.11, but for the whole 90–120 km altitude range.

7.4 Additional figures of Chapter 5

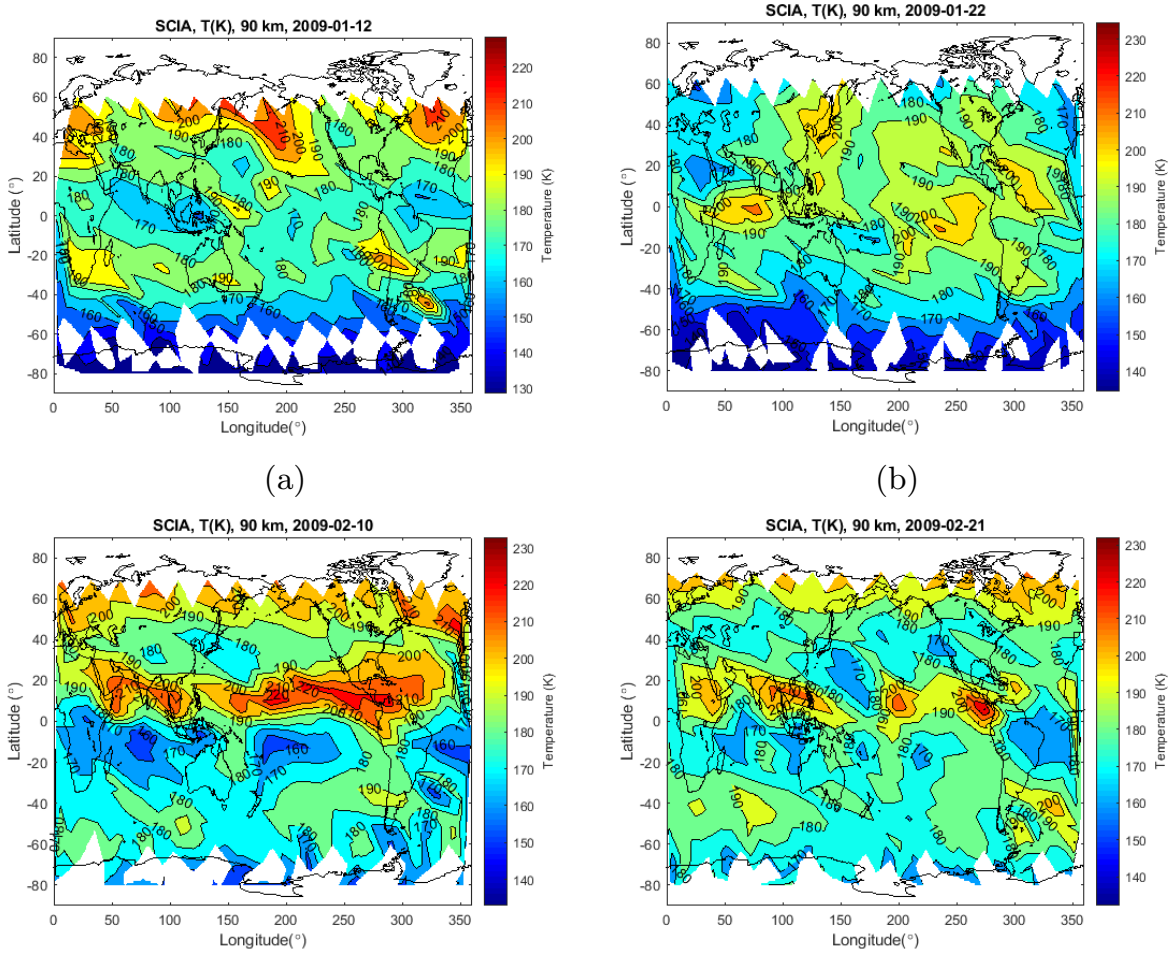

Figure 7.14: Longitude-latitude map of temperature at 90 km altitude, as retrieved by SCIAMACHY on the MLT scan days during and after the SSW of January 2009 event.

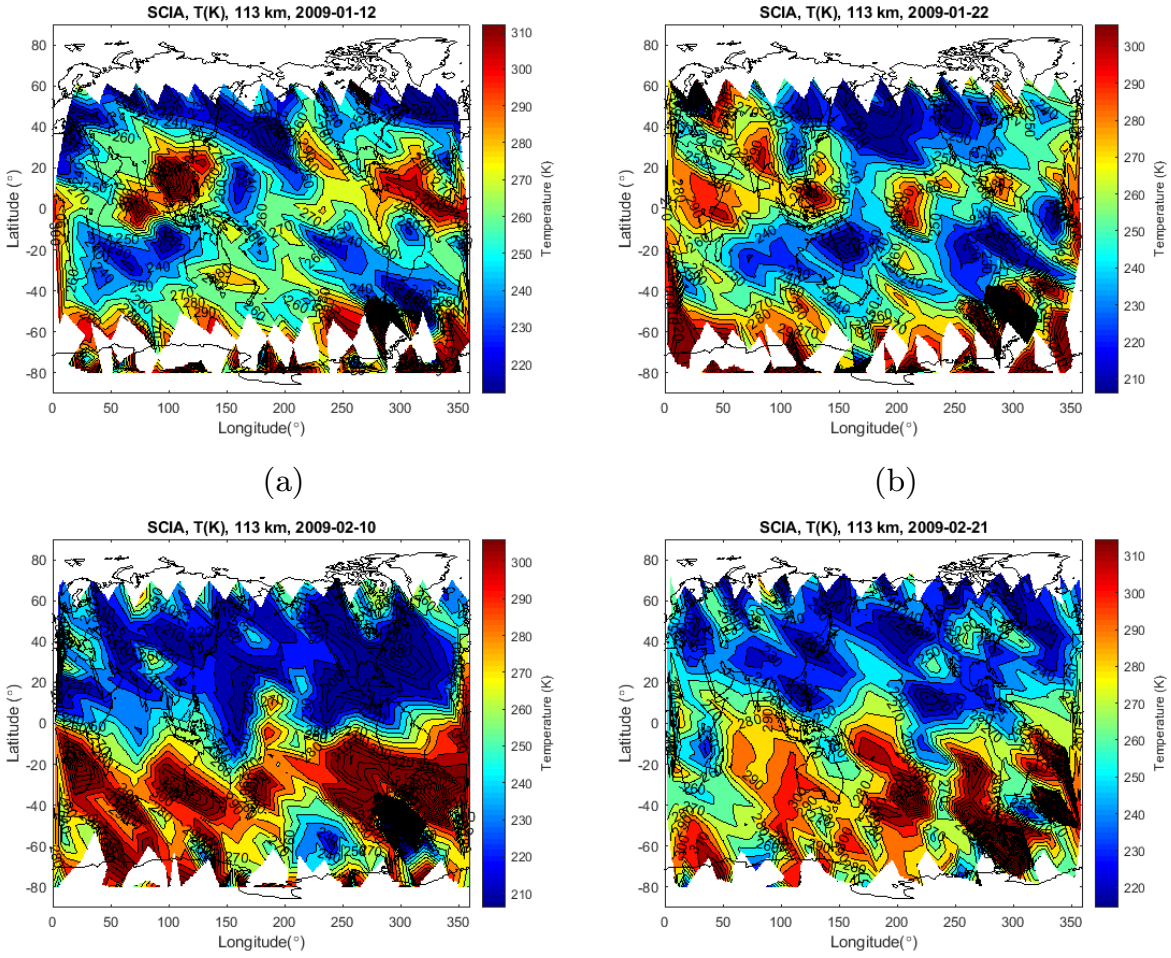

Figure 7.15: Longitude-latitude map of temperature at 113 km altitude, as retrieved by SCIAMACHY on the MLT scan days during and after the SSW of January 2009 event.

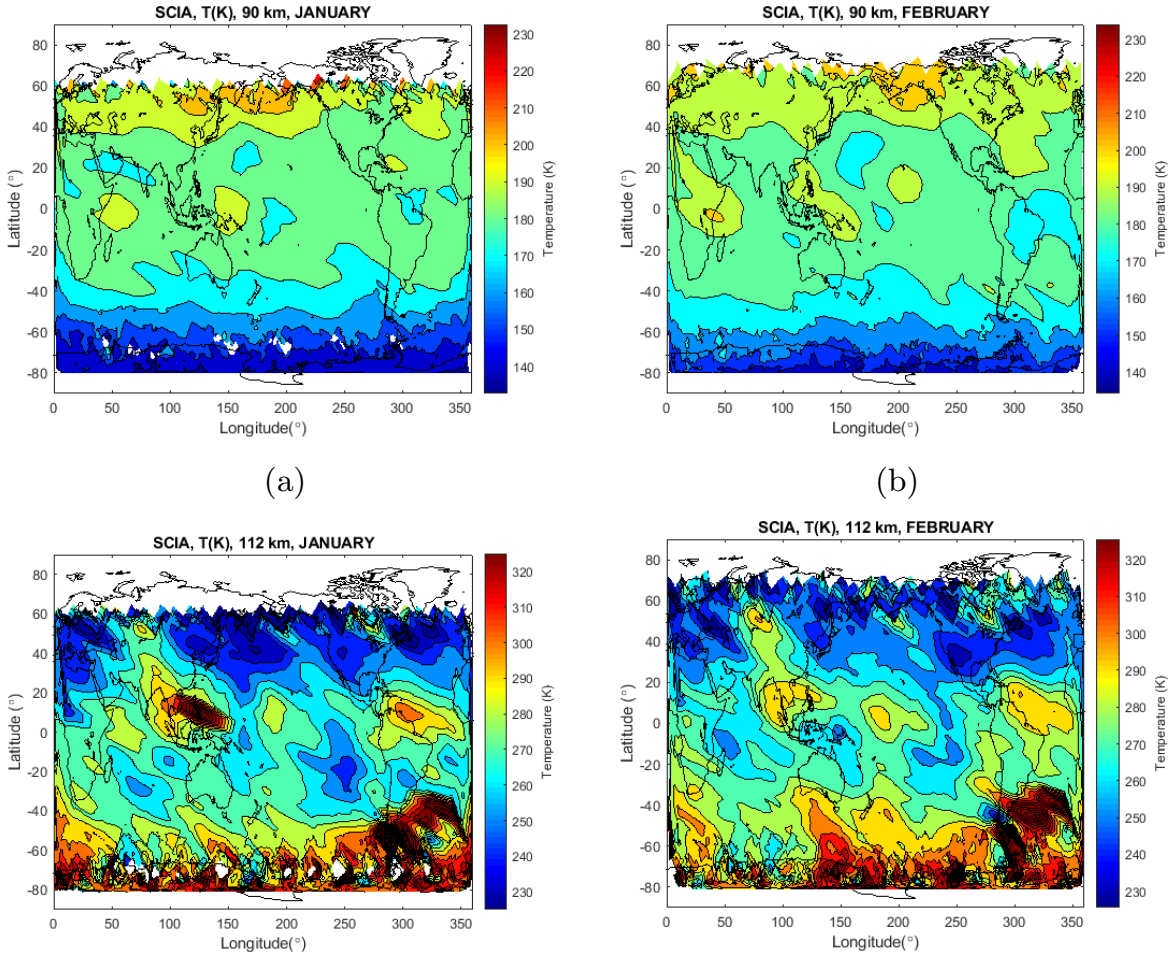

Figure 7.16: Climatologies of temperature at 90 (upper panel) and 112 km altitudes (lower panel) as retrieved by SCIAMACHY on the corresponding MLT scan days during January (left panel) and February (right panel).

8 Bibliography

Akmaev, R.: Modeling the cooling due to CO2 increases in the mesosphere and lower thermosphere, Physics and Chemistry of the Earth, Parts A/B/C, 27, 521–528, 2002.

Akmaev, R.: Thermospheric resistance to "greenhouse cooling": Effect of the collisional excitation rate by atomic oxygen on the thermal response to CO2 forcing, Journal of Geophysical Research: Space Physics, 108, 2003.

Akmaev, R. and Fomichev, V.: A model estimate of cooling in the mesosphere and lower thermosphere due to the CO2 increase over the last 3–4 decades, Geophysical Research Letters, 27, 2113–2116, 2000.

Akmaev, R., Fomichev, V., and Zhu, X.: Impact of middle-atmospheric composition changes on greenhouse cooling in the upper atmosphere, Journal of Atmospheric and Solar-Terrestrial Physics, 68, 1879–1889, 2006.

Babcock, H. D. and Herzberg, L.: Fine Structure of the Red System of Atmospheric Oxygen Bands., Astrophysical Journal, 108, 167, doi:10.1086/145062, 1948.

Bageston, J. V., Batista, P. P., Gobbi, D., Takahashi, H., Paes-Leme, N. M., and Wrasse, C. M.: AIRGLOW AND ITS IMPORTANCE ON MONITORING THE UPPER ATMOSPHERE: OBSERVATIONS AT COMMANDANT FERRAZ ANTARCTIC STATION, Annual activity report, 2012.

Barth, C. A.: Three-body reactions, in: Annales de Geophysique, Vol. 20, p. 182, 1964.

Barth, C. A. and Hildebrandt, A. F.: The 5577 A airglow emission mechanism, Journal of Geophysical Research, 66, 985–986, 1961.

Bates, D.: The green light of the night sky, Planetary and Space Science, 29, 1061–1067, doi:10.1016/0032-0633(81)90003-9, 1981.

Bates, D.: Excitation and quenching of the oxygen bands in the nightglow, Planetary and space science, 36, 875–881, 1988.

Beig, G., Keckhut, P., Lowe, R. P., Roble, R., Mlynczak, M., Scheer, J., Fomichev, V., Offermann, D., French, W., Shepherd, M., et al.: Review of mesospheric temperature trends, Reviews of Geophysics, 41, 2003.

Bender, S., Sinnhuber, M., Burrows, J., Langowski, M., Funke, B., and López-Puertas, M.: Retrieval of nitric oxide in the mesosphere and lower thermosphere with SCIAMACHY., Atmospheric Measurement Techniques Discussions, 6, 2013.

Bovensmann, H., Burrows, J. P., Buchwitz, M., Frerick, J., Noël, S., Rozanov, V. V., Chance, K. V., and Goede, a. P. H.: SCIAMACHY: Mission Objectives and Measurement Modes, Journal of the Atmospheric Sciences, 56, 127–150, 1999.

Brasseur, G. P. and Solomon, S.: Aeronomy of the middle atmosphere: chemistry and physics of the stratosphere and mesosphere, Vol. 32, Springer Science & Business Media, 2006.

Bremer, J. and Berger, U.: Mesospheric temperature trends derived from ground-based LF phase-height observations at mid-latitudes: comparison with model simulations, Journal of Atmospheric and Solar-Terrestrial Physics, 64, 805–816, 2002.

Butchart, N.: The Brewer-Dobson circulation, Reviews of geophysics, 52, 157–184, 2014.

Chau, J. L., Goncharenko, L. P., Fejer, B. G., and Liu, H.-L.: Equatorial and low latitude ionospheric effects during sudden stratospheric warming events, Space Science Reviews, 168, 385–417, 2012.

Christensen, A. B., Yee, J.-H., Bishop, R. L., Budzien, S. A., Hecht, J. H., Sivjee, G., and Stephan, A. W.: Observations of molecular oxygen Atmospheric band emission in the thermosphere using the near infrared spectrometer on the ISS/RAIDS experiment, Journal of Geophysical Research: Space Physics, 117, 2012.

Council, N. R.: SOLAR VARIATIONS, OZONE, AND THE MIDDLE ATMOSPHERE, in: Solar Influences on Global Change, Chap. 3, The National Academies Press, Washington, DC, doi:10, 1994.

Cumberland, L.: On the Physical and Chemical Interactions between Polar Mesospheric Clouds and Upper Mesospheric Temperature and Ozone Chemistry, Ph.D. thesis, copyright - Database copyright ProQuest LLC; ProQuest does not claim copyright in the individual underlying works; Last updated - 2016-03-11, 2012.

Dameris, M., Godin-Beekmann, S., Alexander, S., Braesicke, P., Chipperfield, M., de Laat, A., Orsolini, Y., Rex, M., and Santee, M.: Update on polar ozone: Past, present, and future, Chapter 3 in Scientific Assessment of Ozone Depletion: 2014, Global Ozone Research and Monitoring Project–Report No. 55, World Meteorological Organization, Geneva, Switzerland, 2014.

DeMore, W. B.: Primary Processes in Ozone Photolysis, The Journal of Chemical Physics, 44, 1780, doi:10.1063/1.1726939, 1966.

Dzubenko, N., Ivchenko, V., and Kozak, L.: Temperature variations in the thermosphere over the earthquake focuses as inferred from satellite data, GEOMAGNETISM AND AERONOMY C/C OF GEOMAGNETIZM I AERONOMIIA, 43, 118–123, 2003.

Evans, W. F. J., Hunten, D. M., Llewellyn, E. J., and Jones, A. V.: Altitude profile of the infrared atmospheric system of oxygen in the dayglow, Journal of Geophysical Research, 73, 2885–2896, doi:10.1029/JA073i009p02885, 1968.

Fischer, H., Birk, M., Blom, C., Carli, B., Carlotti, M., Clarmann, T. v., Delbouille, L., Dudhia, A., Ehhalt, D., Endemann, M., et al.: MIPAS: an instrument for atmospheric and climate research, Atmospheric Chemistry and Physics, 8, 2151–2188, 2008.

Funke, B., Lopez-Puertas, M., Bermejo-Pantalen, D., Garca-Comas, M., Stiller, G. P., Von Clarmann, T., Kiefer, M., and Linden, A.: Evidence for dynamical coupling from the lower atmosphere to the thermosphere during a major stratospheric warming, Geophysical Research Letters, 37, 1–5, doi:10.1029/2010GL043619, 2010.

Gamache, R. R. and Rothman, L. S.: Extension of the HITRAN database to non-LTE applications, Journal of Quantitative Spectroscopy and Radiative Transfer, 48, 519 – 525, doi:https://doi.org/10.1016/0022-4073(92)90117-M, special Issue Conference on Molecular Spectroscopic Databases, 1992.

Gao, H., Xu, J., Chen, G., Yuan, W., and Beletsky, A. B.: Global distributions of OH and O2 (1.27 μm) nightglow emissions observed by TIMED satellite, Science China Technological Sciences, 54, 447–456, doi:10.1007/s11431-010-4236-5, 2011a.

Gao, H., Xu, J., Ward, W., and Smith, A. K.: Temporal evolution of nightglow emission responses to SSW events observed by TIMED/SABER, Journal of Geophysical Research: Atmospheres, 116, 2011b.

García-Comas, M., Funke, B., Gardini, A., López-Puertas, M., Jurado-Navarro, A., von Clarmann, T., Stiller, G., Kiefer, M., Boone, C. D., Leblanc, T., Marshall, B. T., Schwartz, M. J., and Sheese, P. E.: MIPAS temperature from the stratosphere to the lower thermosphere: Comparison of vM21 with ACE-FTS, MLS, OSIRIS, SABER, SOFIE and lidar measurements, Atmospheric Measurement Techniques, 7, 3633–3651, doi:10.5194/amt-7-3633-2014, 2014.

Gold, E.: The isothermal layer of the atmosphere and atmospheric radiation, Proceedings of the Royal Society of London A: Mathematical, Physical and Engineering Sciences, 82, 43–70, doi:10.1098/rspa.1909.0006, 1909.

Gottwald, M. and Bovensmann, H.: SCIAMACHY-Exploring the changing Earth's Atmosphere, Springer Science & Business Media, 2010.

Greer, R., Llewellyn, E., Solheim, B., and Witt, G.: The excitation of O2 (b1Σg+) in the nightglow, Planetary and Space Science, 29, 383–389, 1981.

Grygalashvyly, M., Sonnemann, G., Lübken, F.-J., Hartogh, P., and Berger, U.: Hydroxyl layer: Mean state and trends at midlatitudes, Journal of Geophysical Research: Atmospheres, 119, 12–391, 2014.

Harada, Y., Goto, A., Hasegawa, H., Fujikawa, N., Naoe, H., and Hirooka, T.: A Major Stratospheric Sudden Warming Event in January 2009, Journal of the Atmospheric Sciences, 67, 2052–2069, doi:10.1175/2009JAS3320.1, 2010.

Hays, P. B., Abreu, V. J., Dobbs, M. E., Gell, D. A., Grassl, H. J., and Skinner, W. R.: The high-resolution doppler imager on the Upper Atmosphere Research Satellite, Journal of Geophysical Research, 98, 10 713, doi:10.1029/93JD00409, 1993.

Herzberg, G.: Molecular spectra and molecular structure: spectra of diatomic molecules, Vol. 1, van Nostrand, 1950.

Holton, J. R. and Hakim, G. J.: An introduction to dynamic meteorology, Vol. 88, Academic press, 2012.

Huestis, D. L.: Current Laboratory Experiments for Planetary Aeronomy, 245–258, American Geophysical Union, doi:10.1029/130GM16, 2013.

IPCC: Climate Change 2013: The Physical Science Basis. Contribution of Working Group I to the Fifth Assessment Report of the Intergovern- mental Panel on Climate Change, Tech. rep., IPCC, United Kingdom and New York, NY, USA, 2013.

James M. Russell, Martin G. Mlynczak, L. L. G. J. J. T. R. W. E.: Overview of the SABER experiment and preliminary calibration results, doi:10.1117/12.366382, 1999.

Khomich, V. Y., Semenov, A. I., and Shefov, N. N.: Airglow as an indicator of upper atmospheric structure and dynamics, doi:10.1007/978-3-540-75833-4, 2008.

Killeen, T. L., Wu, Q., Solomon, S. C., Ortland, D. A., Skinner, W. R., Niciejewski, R. J., and Gell, D. A.: TIMED Doppler Interferometer: Overview and recent results, Journal of Geophysical Research, 111, A10S01, doi:10.1029/2005JA011484, 2006.

Kirillov, A.: The calculation of quenching rate coefficients of O2 Herzberg states in collisions with CO2, CO, N2, O2 molecules, Chemical Physics Letters, 592, 103 – 108, doi:10.1016/j.cplett.2013.12.009, 2014.

Kirillov, A. S.: Model of vibrational level populations of Herzberg states of oxygen molecules at heights of the lower thermosphere and mesosphere, Geomagnetism and Aeronomy, 52, 242–247, doi:10.1134/S0016793212020077, 2012.

Kurnosova, L., Kolobyanina, T., Logachev, V., Razorenov, L., Sirotkin, I., and Fradkin, M.: Discovery of radiation anomalies above the South Atlantic at heights of 310–340 km, Planetary and Space Science, 9, 513–516, doi:10.1016/0032-0633(62)90057-0, 1962.

Lednyts'kyy, O., Von Savigny, C., Eichmann, K. U., and Mlynczak, M. G.: Atomic oxygen retrievals in the MLT region from SCIAMACHY nightglow limb measurements, Atmospheric Measurement Techniques, 8, 1021–1041, doi:10.5194/amt-8-1021-2015, 2015.

Liou, K.-N.: An introduction to atmospheric radiation, Vol. 84, Elsevier, 2002.

Liu, H.-L., Wang, W., Richmond, A. D., and Roble, R. G.: Ionospheric variability due to planetary waves and tides for solar minimum conditions, Journal of Geophysical Research: Space Physics, 115, doi:10.1029/2009JA015188, 2010.

Llewellyn, E. J., Lloyd, N. D., Degenstein, D. A., Gattinger, R. L., Petelina, S. V., Bourassa, A. E., Wiensz, J. T., Ivanov, E. V., McDade, I. C., Solheim, B. H., McConnell, J. C., Haley, C. S., von Savigny, C., Sioris, C. E., McLinden, C. A., Griffioen, E., Kaminski, J., Evans, W. F., Puckrin, E., Strong, K., Wehrle, V., Hum, R. H., Kendall, D. J., Matsushita, J., Murtagh, D. P., Brohede, S., Stegman, J., Witt, G., Barnes, G., Payne, W. F., Piché, L., Smith, K., Warshaw, G., Deslauniers, D. L., Marchand, P., Richardson, E. H., King, R. A., Wevers, I., McCreath, W., Kyrölä, E., Oikarinen, L., Leppelmeier, G. W., Auvinen, H., Mégie, G., Hauchecorne, A., Lefèvre, F., de La Nöe, J., Ricaud, P., Frisk, U., Sjoberg, F., von Schéele, F., and Nordh, L.: The OSIRIS instrument on the Odin spacecraft, Canadian Journal of Physics, 82, 411–422, doi:10.1139/p04-005, 2004.

Long, D., Havey, D., Okumura, M., Miller, C., and Hodges, J.: O2A-band line parameters to support atmospheric remote sensing, Journal of Quantitative Spectroscopy and Radiative Transfer, 111, 2021 – 2036, doi:https://doi.org/10.1016/j.jqsrt.2010.05.011, 2010.

Matsuno, T.: A dynamical model of the stratospheric sudden warming, 1971.

Mlynczak, M., Morgan, F., Yee, J.-H., Espy, P., Murtagh, D., Marshall, B., and Schmidlin, F.: Simultaneous measurements of the O2 ($^1\Delta$) and O2 ($^1\Sigma$) Airglows and ozone in the daytime mesosphere, Geophysical research letters, 28, 999–1002, 2001.

Mlynczak, M. G. and Nesbitt, D. J.: The Einstein Coefficient for spontaneous emission of the O2 ($a^1\Delta g$) state, Geophysical research letters, 22, 1381–1384, 1995.

Mlynczak, M. G. and Olander, D. S.: On the utility of the molecular oxygen dayglow emissions as proxies for middle atmospheric ozone, Geophysical Research Letters, 22, 1377–1380, doi:10.1029/95GL01321, 1995.

Mlynczak, M. G., Solomon, S., and Zaras, D. S.: An updated model for O 2 (a 1 Δg) concentrations in the mesosphere and lower thermosphere and implications for remote sensing of ozone at 1.27 μm, Journal of Geophysical Research: Atmospheres, 98, 18 639–18 648, doi:10.1029/93JD01478, 1993.

Nicolet, M.: Aeronomic reactions of hydrogen and ozone, in: Mesospheric models and related experiments, 1–51, Springer, 1971.

Oelhaf, H.: MIPAS mission plan, Tech. Note ENVI-SPPA-EOPG-TN-07, 73, 2008.

Pachauri, R. K., Allen, M. R., Barros, V. R., Broome, J., Cramer, W., Christ, R., Church, J. A., Clarke, L., Dahe, Q., Dasgupta, P., et al.: Climate change 2014: synthesis report. Contribution of Working Groups I, II and III to the fifth assessment report of the Intergovernmental Panel on Climate Change, IPCC, 2014.

Pedatella, N., Chau, J., Schmidt, H., Goncharenko, L., Stolle, C., Hocke, K., Harvey, V., Funke, B., and Siddiqui, T.: How sudden stratospheric warming affects the whole atmosphere, Eos, 99, 35–38, 2018.

Picone, J., Hedin, A., Drob, D. P., and Aikin, A.: NRLMSISE-00 empirical model of the atmosphere: Statistical comparisons and scientific issues, Journal of Geophysical Research: Space Physics, 107, 2002.

Ralchenko, Y., Kramida, A., Reader, J., et al.: NIST atomic spectra database, National Institute of Standards and Technology, Gaithersburg, MD, 2008.

Randel, W. J., Shine, K. P., Austin, J., Barnett, J., Claud, C., Gillett, N. P., Keckhut, P., Langematz, U., Lin, R., Long, C., Mears, C., Miller, A., Nash, J., Seidel, D. J., Thompson, D. W. J., Wu, F., and Yoden, S.: An update of observed stratospheric temperature trends, Journal of Geophysical Research: Atmospheres, 114, doi:10.1029/2008JD010421, 2009.

Raspollini, P., Carli, B., Carlotti, M., Ceccherini, S., Dehn, A., Dinelli, B. M., Dudhia, A., Flaud, J.-M., López-Puertas, M., Niro, F., Remedios, J. J., Ridolfi, M., Sembhi, H., Sgheri, L., and von Clarmann, T.: Ten years of MIPAS measurements with ESA Level 2 processor V6 - Part 1: Retrieval algorithm and diagnostics of the products, Atmospheric Measurement Techniques, 6, 2419–2439, doi:10.5194/amt-6-2419-2013, 2013.

Rothman, L. S., Jacquemart, D., Barbe, A., Benner, D. C., Birk, M., Brown, L., Carleer, M., Chackerian Jr, C., Chance, K., Coudert, L. e. a., et al.: The HITRAN 2004 molecular spectroscopic database, Journal of quantitative spectroscopy and radiative transfer, 96, 139–204, 2005.

Salby, M. L.: Fundamentals of atmospheric physics, Vol. 61, Elsevier, 1996.

Sheese, P. E., Llewellyn, E. J., Gattinger, R. L., Bourassa, A. E., Degenstein, D. A., Lloyd, N. D., and McDade, I. C.: Temperatures in the upper mesosphere and lower thermosphere from OSIRIS observations of O2 A-band emission spectra, Canadian Journal of Physics, 88, 919–925, doi:10.1139/P10-093, 2010.

Shepherd, G. G., Thuillier, G., Gault, W. A., Solheim, B. H., Hersom, C., Alunni, J. M., Brun, J.-F., Brune, S., Charlot, P., Cogger, L. L., Desaulniers, D.-L., Evans, W. F. J., Gattinger, R. L., Girod, F., Harvie, D., Hum, R. H., Kendall, D. J. W., Llewellyn, E. J., Lowe, R. P., Ohrt, J., Pasternak, F., Peillet, O., Powell, I., Rochon, Y., Ward, W. E., Wiens, R. H., and Wimperis, J.: WINDII, the wind imaging interferometer on the Upper Atmosphere Research Satellite, Journal of Geophysical Research, 98, 10 725, doi:10.1029/93JD00227, 1993.

Sinnhuber, M., Berger, U., Funke, B., Nieder, H., Reddmann, T., Stiller, G., Versick, S., von Clarmann, T., and Wissing, J. M.: NO_y production, ozone loss and changes in net radiative heating due to energetic particle precipitation in 2002–2010, Atmospheric Chemistry and Physics, 18, 1115–1147, doi:10.5194/acp-18-1115-2018, 2018.

Siskind, D. E., Eckermann, S. D., McCormack, J. P., Coy, L., Hoppel, K. W., and Baker, N. L.: Case studies of the mesospheric response to recent minor, major, and extended stratospheric warmings, Journal of Geophysical Research Atmospheres, 115, 1–16, doi:10.1029/2010JD014114, 2010.

Skinner, W. and Hays, P.: Brightness of the O2 atmospheric bands in the daytime thermosphere, Planetary and Space Science, 33, 17–22, doi:10.1016/0032-0633(85)90138-2, 1985.

Slanger, T., Cosby, P., Sharpee, B., Minschwaner, K., and Siskind, D.: O (1S $\rightarrow$ 1D, 3P) branching ratio as measured in the terrestrial nightglow, Journal of Geophysical Research: Space Physics, 111, 2006.

Slanger, T. G. and Copeland, R. A.: Energetic Oxygen in the Upper Atmosphere and the Laboratory, Chemical Reviews, 103, 4731–4765, doi:10.1021/cr0205311, 2003.

Smith, I. W. M.: The role of electronically excited states in recombination reactions, International Journal of Chemical Kinetics, 16, 423–443, doi:10.1002/kin.550160411, 1984.

Smith-Johnsen, C., Orsolini, Y., Stordal, F., Limpasuvan, V., and Pérot, K.: Nighttime mesospheric ozone enhancements during the 2002 southern hemispheric major stratospheric warming, Journal of Atmospheric and Solar-Terrestrial Physics, 168, 100–108, 2018.

Stegman, J. and Murtagh, D.: The molecular oxygen band systems in the UV nightglow: measured and modelled, Planetary and Space Science, 39, 595–609, 1991.

Strahan, S.: MIDDLE ATMOSPHERE | Transport Circulation, in: Encyclopedia of Atmospheric Sciences (Second Edition), edited by North, G. R., Pyle, J., and Zhang, F., 41 – 49, Academic Press, Oxford, second edition edn., doi:https://doi.org/10.1016/B978-0-12-382225-3.00231-0, 2015.

Thomas, G.: Is the polar mesosphere the miner's canary of global change?, Advances in Space Research, 18, 149 – 158, doi:https://doi.org/10.1016/0273-1177(95)00855-9, thermosphere-Ionosphere-Middle Atmosphere Coupling and Dynamics, 1996a.

Thomas, G.: Global change in the mesosphere-lower thermosphere region: has it already arrived?, Journal of Atmospheric and Terrestrial Physics, 58, 1629–1656, 1996b.

Thomas, R. J., Barth, C. A., Rottman, G. J., Rusch, D. W., Mount, G. H., Lawrence, G. M., Sanders, R. W., Thomas, G. E., and Clemens, L. E.: Ozone density distribution in the mesosphere (50-90 km) measured by the SME limb scanning near infrared spectrometer, Geophysical Research Letters, 10, 245–248, doi:10.1029/GL010i004p00245, 1983.

Thomas, R. J., Barth, C. A., Rusch, D. W., and Sanders, R. W.: Solar Mesosphere Explorer Near-Infrared Spectrometer: Measurements of 1.27-μm radiances and the inference of mesospheric ozone, Journal of Geophysical Research: Atmospheres, 89, 9569–9580, 1984.

Von Zahn, U.: Are noctilucent clouds a "Miner's Canary" for global change?, EOS, Transactions American Geophysical Union, 84, 261–264, 2003.

Von Zahn, U., Höffner, J., Eska, V., and Alpers, M.: The mesopause altitude: Only two distinctive levels worldwide?, Geophysical Research Letters, 23, 3231–3234, 1996.

Wayne, R. P.: Chemistry of atmospheres., 1991.

Wayne, R. P.: Singlet oxygen in the environmental sciences, Research on Chemical Intermediates, 20, 395–422, doi:10.1163/156856794X00397, 1994.

Winick, J., Wintersteiner, P., Picard, R., Esplin, D., Mlynczak, M., Russell, J., and Gordley, L.: OH layer characteristics during unusual boreal winters of 2004 and 2006, Journal of Geophysical Research: Space Physics, 114, 2009.

WMO: Scientific Assessment of Ozone Depletion: 2018, Tech. Rep. Global Ozone Research and Monitoring Project—Report No. 58, WMO (World Meteorological Organization), Geneva, Switzerland, 2018.

Wraight, P.: Association of atomic oxygen and airglow excitation mechanisms, Planetary and Space Science, 30, 251 – 259, doi:10.1016/0032-0633(82)90003-4, 1982.

Yamamoto, H., Makino, T., Sekiguchi, H., and Naito, I.: Infrared atmospheric band airglow radiometer on board the satellite OHZORA., Journal of geomagnetism and geoelectricity, 40, 321–333, 1988.

Zarboo, A., Bender, S., Burrows, J. P., Orphal, J., and Sinnhuber, M.: Retrieval of $O_2(^1\Sigma)$ and $O_2(^1\Delta)$ volume emission rates in the mesosphere and lower thermosphere using SCIAMACHY MLT limb scans, Atmospheric Measurement Techniques, 11, 473–487, doi:10.5194/amt-11-473-2018, 2018.

List of Figures

List of Tables

List of Acronyms

SCIAMACHY	SCanning Imaging Absorption spectroMeter for Atmospheric CHartographY
Envisat	ENVIronmental SATellite
MIPAS	Michelson Interferometer for Passive Atmospheric Sounding
TIMED	Thermosphere-Ionosphere-Mesosphere Energetics and Dynamics (TIMED)
SABER	Sounding of the Atmosphere using Broadband Emission Radiometry
OSIRIS	Optical Spectrograph and InfraRed Imager System
SAA	South Atlantic Anomaly
EI	Emission Intensity
VER	Volume Emission Rate
SSW	Stratospheric Sudden Warming
MLT	Mesosphere Lower Thermosphere
SPE	Solar Proton Event
IPCC	Intergovenmental Panel on Climate Change
WMO	World Meteorological Organisation
AVHRR	Advanced Very High Resolution Radiometer
NOAA	National Oceanic and Atmospheric Administration
NASA	National Aeronautics and Space Administration
MLS	Microwave Limb Sounder
MERRA	Modern-Era Retrospective Analysis for research and Applications
EOS	Earth Observing System
CA	Centroid Altitude
SZA	Solar Zenith Angle

Acknowledgements

First, I would like to thank my supervisor, Dr. Miriam Sinnhuber for giving me the opportunity to do this PhD work. I would like to thank her for all the helps, supports, and advices that she offered me throughout my PhD. She always managed to find whatever time was needed to discuss about my PhD work. The freedom in research and her patience were important sources of inspiration and fostering this PhD work, especially during the hard moments.
I also like to thank my committee members (Prof. Dr. Johannes Orphal and Dr. Michael Höpfner) for reading this thesis and counseling me throughout this work. My special thanks to Dr. Stefan Bender for his perceptive scientific advice and many constructive comments and suggestions. He always gave me support and help, and inspired me with creative ideas and perspective. Also I would like to thank Dr. Sabine Barthlott for her kind advice and guidance, and Dr. Jennifer Schroter for providing me with the template and suggestions during writing my thesis.
Finally, I would like to thank my family for all their love and encouragement. I can not express how I am grateful to my wife "Naghmeh" for sacrificing her job, and devoting all of her love and care to me, supporting in every stage of my PhD work, and life. After that, I am thankful of my parents for their love and motivation.